Interactions of Plasmonic and Dielectric Structures with 2D Materials

A PhD Thesis

by:

Julia Lawless

Supervisor:

Prof. Louise Bradley

School of Physics
Trinity College Dublin
2023

Declaration

I declare that this thesis has not been submitted as an exercise for a degree at this or any other university and it is entirely my own work. Any assistance or collaboration is recognised in the acknowledgements and throughout the thesis where applicable.

I agree to deposit this thesis in the University's open access institutional repository or allow the Library to do so on my behalf, subject to Irish Copyright Legislation and Trinity College Library conditions of use and acknowledgement.

I consent to the examiner retaining a copy of the thesis beyond the examining period, should they so wish (EU GDPR May 2018).

Julia Lawless

Acknowledgements

I would like to thank my supervisor, Prof. Louise Bradley for giving me this opportunity to do a PhD in her group and for all of the helpful advice and guidance throughout. It was an amazing experience to be part of her research group.

I would also like to acknowledge all of the other members in the Bradley group, Dr. Calin Hrelescu, Dr. Xia Zhang, Dr. Jorge Garcia, Dr. Stephen Cunningham, Dr. Oisín McCormack, Carolyn Elliott, Fionnuala McGrath, Jing Qian, Sara Pelivani and Jack Dobie. It has been a pleasure working with all of them over the last few years. In particular I would like to thank Calin for teaching me about Lumerical, Carolyn for teaching me how to synthesise bipyramids, Xia for our collaborations and for co-authoring a paper with me and Oisín for all the hours of dark field measurements we carried out together.

I would also like to acknowledge Dr. Niall McEvoy, Dr. Lisanne Peters and Joshua Pepper for growing the MoS_2 and graphene samples, and for teaching me how to grow my own samples too. I would like to thank Dr. Jing Li for fabricating the Si disk arrays used in this thesis.

I would like to give special thanks to my mother, Ellen, my brothers and sisters, Anna, Caoimhín, Caroline and Charlie and my niece, Aisling. Their support and encouragement have been invaluable throughout the past four years. I would also like to acknowledge my cat, Mia, for her eternal comfort and support during the long months of working from home in the pandemic, and for her unparalleled enthusiasm with lasers!

Finally, I would like to thank my boyfriend, Stephen, for all his love, support and guidance while we both completed our PhDs. I could not have done it without him!

Abstract

Three separate systems of nanoparticles coupled to two-dimensional materials are studied. Each system is investigated both experimentally and numerically with FDTD simulations.

The first system involves a nanoparticle-on-mirror approach, with a 150 nm Au sphere on a 100 nm Au film with an intermediate monolayer of graphene in between. The gap size between the Au nanosphere and film, as well as the doping level of the graphene is altered by immersing the system in nitric acid. The scattering spectra for individual nanospheres revealed three multipolar modes, which red-shifted with a reduced gap size and blue-shifted with increased chemical potential of the graphene. Smaller gap sizes increased the electric field strength between the Au sphere and film, increasing the interaction with the graphene. Additionally, it was found that the dipolar mode splits into two new modes due to the coupling of the gap plasmon and the charge transfer plasmon. This work demonstrates the merging of two other theories previously shown to strongly influence the multipolar plasmonic modes in the nanoparticle on mirror system.

The second system consists of single Au nano-bipyramids drop-cast on a monolayer of MoS_2. Rabi splitting is achieved between the longitudinal plasmons of the Au bipyramids and the excitons of the MoS_2 layer. This strong coupling effect is enhanced by increasing the size of the bipyramids. This is due to the higher electric field strength concentrated at the tips of the larger bipyramids, and also due to the lower aspect ratio of the bipyramid required to keep the plasmon energy overlapped with the energy of the exciton. A lower aspect ratio increases the natural tilt a bipyramid has towards the substrate, tilting the plasmon to overlap more closely with the exciton, and hence increases the strong coupling effect. A bipyramid's sharp tips are also important to increase the Rabi splitting strength, by both increasing the electric field strength and confinement and by tilting the plasmon resonance more directly towards the MoS_2 layer. This work is the first demonstration of the Rabi splitting strength increasing with an increased metal volume of nanoparticle, without increasing the number of excitons coupled into the system.

The final system is a monolayer of MoS_2 placed on top of a Si disk array on a SiO_2/Si substrate. The Si disks are shown to cause a photoluminescence enhancement in the MoS_2 for two different pump wavelengths, caused primarily due to the increased absorption at both wavelengths. The system was further optimised with simulations, by replacing the Si in the substrate with Au to act as a back-reflector. This increases the absorption in a monolayer of MoS_2 to up to 53%.

List of Publications and Conference Contributions

Publications

1. Julia Lawless, Calin Hrelescu, Carolyn Elliott, Lisanne Peters, Niall McEvoy, & A. Louise Bradley (2020) ‘Influence of gold nano-bipyramid dimensions on strong coupling with excitons of monolayer MoS_2.’ ACS Applied Materials & Interfaces, 12(41), 46406-46415.
   Basis for chapter 5.

2. Xia Zhang, Julia Lawless, Jing Li, John F. Donegan, Lisanne Peters, Niall McEvoy & A. Louise Bradley. (2022). ‘Absorbance enhancement of monolayer MoS_2 in a perfect absorbing system.’ Physical Review Materials, 6(4), 045202.
   Basis for chapter 6.

3. Julia Lawless, Oisín McCormack, Joshua Pepper, Niall McEvoy & A. Louise Bradley ‘Spectral Tuning of a Nanoparticle-on-Mirror System by Graphene Doping and Gap Control with Nitric Acid.’ (Manuscript in preparation, 2022)
   Basis for chapter 4.

Conference Contributions

1. Julia Lawless, Calin Hrelescu, Carolyn Elliott, Lisanne Peters, Niall McEvoy, & A. Louise Bradley ‘Rabi Splitting between Plasmons of Gold Nano-bi pyramids and Excitons of Monolayer MoS_2 revealed by Single-particle Dark Field Spectroscopy.’ Microscopy Society of Ireland Symposium 2020, 8th - 10th January 2020, Dublin, Ireland. (Oral Presentation)

2. Julia Lawless, Calin Hrelescu, Carolyn Elliott, Lisanne Peters, Niall McEvoy, & A. Louise Bradley ‘Rabi Splitting of Gold Nano-bipyramids coupled to Monolayer MoS_2.’ Physics of Light-Matter Coupling in Nanostructures (PLMCN) 2020, 27th - 30th October 2020, Clermont-Ferrand, France (Virtual conference). (Poster)

3. Julia Lawless, Calin Hrelescu, Carolyn Elliott, Lisanne Peters, Niall McEvoy, & A. Louise Bradley ‘Influence of nanoparticle dimensions on Rabi splitting strength.’ Conference on Lasers and Electro-Optics (CLEO) 2021, 9th - 14th May 2021, San Jose, USA. (Poster)

4. Julia Lawless, Calin Hrelescu, Carolyn Elliott, Lisanne Peters, Niall McEvoy, & A. Louise Bradley 'Rabi Splitting of Gold Nano-bipyramids coupled to Monolayer MoS_2.' European Materials Research Society (EMRS) 2021, 31st May - 4th June 2021, France (Virtual conference). (Oral Presentation)

5. Julia Lawless, Calin Hrelescu, Carolyn Elliott, Lisanne Peters, Niall McEvoy, & A. Louise Bradley 'Use of Gold Nano-Bipyramids with monolayer MoS_2 for the Manipulation of Rabi Splitting Strength.' Photonics Ireland 2021, 14th - 16th June 2021, Dublin (Virtual conference). (Oral Presentation)

6. Julia Lawless, Calin Hrelescu, Carolyn Elliott, Lisanne Peters, Niall McEvoy, & A. Louise Bradley 'Rabi Splitting using Gold Nano-Bipyramids and Monolayer MoS_2.' Conference on Lasers and Electro-Optics (CLEO) Europe 2021, 21st - 25th June 2021, Germany (Virtual conference). (Oral Presentation)

7. Julia Lawless, Calin Hrelescu, Carolyn Elliott, Lisanne Peters, Niall McEvoy, & A. Louise Bradley 'Influence of Nanoparticle Dimensions on Rabi Splitting Strength.' Applied Photonics Physics School 2021, 5th - 10th September 2021, Bad Honnef, Germany. (Poster)

8. Julia Lawless, Calin Hrelescu, Carolyn Elliott, Lisanne Peters, Niall McEvoy, & A. Louise Bradley 'The Effect of Nano-Bipyramid Size on Rabi Splitting Strength when Coupled to MoS_2.' European Congress and Exhibition on Advanced Materials and Processes (EUROMAT) 2021, 13th - 17th September 2021, Austria (Virtual conference). (Oral Presentation)

9. Julia Lawless, Calin Hrelescu, Carolyn Elliott, Lisanne Peters, Niall McEvoy, & A. Louise Bradley 'Size Dependence of Rabi Splitting Using Gold Nano-Bipyramids on Monolayer MoS_2.' Smart NanoMaterials: Advances, Innovation, and Applications (SNAIA) 2021, 7th - 10th December 2021, Paris, France (Hybrid conference). (Oral Presentation)

Contents

Dixitque Deus: Fiat lux. Et facta est lux.

Genesis 1:3

1 Introduction

The study and manipulation of light has been crucial to both science and day to day life for centuries. One of the earliest examples of this is the invention of the wearable eyeglasses in 13th century Italy by Salvino D'Armati[1]. The invention of the earliest compound microscope is credited to Zacharias Janssen[2], around the same time as the earliest recorded telescope, which was invented by Hans Lippershay in the early 17th century, before Galileo Galilei published his first astronomical discoveries in 1610[3]. All of these inventions relied on lenses to focus light to improve vision for improving the natural focus of the eye, examining small objects in finer detail and observing far-away objects in space. They proved that light could be manipulated to improve vision and to further the knowledge of science. The uses for light, however, were limited without a deeper knowledge of the fundamental physics by which light behaves.

Many theories were proposed to describe the nature of light, notably the two competing theories of Christiaan Huygens and Isaac Newton. Huygens proposed in 1678 that light was due to propogating waves[4]. In 1704, Newton proposed his corpuscular theory, suggesting that light was made of particles[5]. In 1801, Thomas Young's double slit experiment demonstrated the constructive and destructive interference of two monochromatic sources of light, suggesting that Huygens' theory was correct[6]. In 1864, James Clerk Maxwell derived equations that describing electromagnetic waves. The speed his equations predicted for the speed of the electromagnetic waves was so close to the speed of light, he hypothesised that the electromagnetic disturbances were light itself[4]. In 1890, Heinrich Hertz experimentally proved Maxwell's theory, demonstrating that electromagnetic waves, that moved at the speed of light, could be produced by oscillating electric charges[7]. After this discovery, Hertz said he did not believe that the electromagnetic waves he discovered would have any practical application. It was unknown at the time the revolution in photonics and other areas of science that Hertz's discovery would make possible.

In 1922, Albert Einstein won the Nobel Prize in Physics for his discovery of the photoelectric effect, demonstrating how light interacts with matter and how it is quantised in energy packets called photons[8]. Since this discovery, scientists have strived to study and manipulate the interactions between light and matter. The trend in recent years has been to push devices to smaller and smaller scales for photonic devices, analogous to the trends in electronics. With the rise of interest in nanoscience, the study of nanophotonics has also become more important.

In 1959, nanoscience and nanotechnology were first introduced by Richard Feynman, to the American Physical Society in Caltech in his famous talk, entitled 'There's Plenty of Room at the Bottom'[9]. Since then, there has been an explosion in growth in all areas of nanoscience. Nanoscience is the study of materials larger than the atomic scale, but smaller than the macroscale, generally encompassing all materials with at least one dimension between 1 and 100 nm. These nanomaterials have drastically different properties than their bulk and molecular counterparts[10], which adds to the scientific intrigue of their discovery. Nanomaterials form an exotic intermediate between materials on the bulk and molecular scale, presenting an entirely new set of physical properties to wield into novel devices and applications.

With an increasing amount of scientific interest over the last few decades, a vast range of fabrication methods have been developed for nanomaterials. These techniques can be in the form of a 'top down' or a 'bottom up' approach[11]. 'Top down' approaches involve processing bulk materials to construct a nanomaterial. These techniques include lithographic and milling techniques such as electron beam lithography, photolithography and focused ion beam milling. Very simple methods can also be employed for some materials. For example, mechanical exfoliation of two-dimensional materials is carried out by cleaving away layers of the material with scotch tape until a single monolayer remains. 'Bottom up' approaches involve assembling nanomaterials from the atomic level. These techniques include chemical vapour deposition and physical vapour deposition. Synthesis of nanoparticles in a growth solution is also a 'bottom up' technique.

Metallic nanoparticles are of particular interest in the study of nanophotonics due to localised surface plasmon resonances (LSPRs). This is when light hits a metallic nanoparticle, smaller than the wavelength of the incident light, causing an oscillation of the electrons within. LSPRs can be manipulated by the size, shape and metal of the nanoparticle and can be used to control the scattering and absorption cross sections. LSPRs are also particularly useful due to their tendency to enhance the electric field strength at the surface of the metallic nanoparticle, as well as confine it in very small, sub-wavelength regions. Early examples of plasmons being used to manipulate light can be traced back as far as the 4th century with the Lycurgus cup, an Ancient Roman artifact[12]. Dielectric nanoparticles can be used for similar control over light by manipulating the electric and magnetic multipolar modes described by Mie theory[13]. Dielectric nanostructures have different advantages and disadvantages from the metallic nanoparticles previously mentioned. The electric field hotspot for dielectric nanoparticles is on the inside instead of the surface, as it is for metallic particles. This makes it more difficult to access and couple with other materials. Dielectric nanoparticles, however, are less lossy than their metallic counterparts, with sharper peaks and longer lifetimes. This is advantageous for sensing applications.

Two-dimensional materials are a particularly interesting class of materials, as their properties differ significantly from their bulk counterparts. Graphene exhibits unparallelled carrier mobilities[14], and many transition metal dichalcogenides exhibit a direct band-gap only in their monolayer state[15]. 2D materials also offer the advantage of sub-nanometer thicknesses, increasing the ease of their integration with other components in a device. Additionally, their thin nature allows the increase in their overlap with the electric field hotspot of plasmonic nanoparticles.

The study of nanophotonics has opened the world up to numerous new scientific advances and discoveries. Shrinking photonic devices down to the nanoscale has enabled the development of flat optical metalenses[16, 17]. It has enabled the advancement of sensing, even on the molecular level[18, 19, 20], which provides obvious benefits to many other areas of science and medicine. The advancement of nanophotonics has helped to pave the way to more sustainable energy sources by improving solar cells[21, 22]. It has also given potential to the development of a quantum computer by developing methods for quantum entanglement[23]. Several methods have been developed to allow for the precise placement of quantum emitters in the hot-spots of the electric field strength, for example by 2-photon polymerisation[24] and by optical tweezing[25].

The aim of this thesis is to investigate the coupling of nanoparticles with 2D materials in three different systems. Each system explores how to improve the interaction between Au or Si nanoparticles and an atomically thin layer of graphene or MoS_2. The excitation modes of the nanoparticles are modulated by coupling with the 2D materials. Experimental and numerical results are displayed for each system considered in this thesis. Potential applications for the work displayed include the development of solar cells, quantum sensing and optical switching.

In **chapter 2**, the background theory behind the work presented is introduced. This chapter includes details about the 2D materials used (graphene and MoS_2) with background on the atomic configurations and electric band structures. The physics of localised surface plasmon resonances in metallic nanoparticles is discussed, as well as the magnetic and electric multipolar modes in dielectric nanoparticles. Finally, the weak and strong coupling interactions are discussed, giving background to the coupling of nanoparticles to MoS_2 in chapters 5 and 6.

Chapter 3 gives an overview of all of the methods employed throughout the work of this thesis. Details of the finite-difference-time-domain (FDTD) simulations are given, as FDTD is used as the method of numerical simulations throughout the entire work. Fabrication techniques of all of the materials used in this thesis are given, including the synthesis of Au nanoparticles (spheres and bipyramids) in aqueous solution and the growth of 2D materials (graphene and MoS_2) by chemical vapour deposition. Finally, the characterisation and measurement techniques are described, including Raman, photoluminescence, dark field, reflectance and UV-vis spectroscopy and scanning electron microscopy. Photolithography is also described, as a method of creating a grid on a substrate to correlate the spectra measured of individual nanoparticles and their corresponding SEM images.

The first experimental system studied in this thesis is shown in **chapter 4**. A system with single Au nanospheres drop-cast on top of an Au film with an intermediate layer of monolayer graphene in between is investigated. The effect of the gap size between the Au film and sphere and the doping of the graphene layer is explored. The change in gap size and the doping of the graphene layer was achieved by immersing the system in nitric acid. It is shown that both the gap size and the doping of the graphene have very large effects on the spectral features of the system because the electric field hot-spot is concentrated in the gap.

In **chapter 5**, a system with single Au nano-bipyramids drop-cast onto a monolayer of MoS_2 on a SiO_2/Si substrate is investigated. This chapter elucidates the strong coupling effect between the longitudinal plasmons of the Au bipyramids and the A exciton of the MoS_2, showing how the system's energy splits into two new energy states. It is shown how a bipyramid is an ideal shape of nanoparticle to achieve strong coupling because of its natural sharp tips, which greatly confine and enhance the electric field strength of the plasmon resonance. Additionally, the bipyramid shape shows a further advantage by its natural tilt towards the substrate on which it is drop-cast, tilting the plasmon resonance towards the MoS_2, increasing the coupling strength.

Chapter 6 investigates the weak coupling regime between an array of Si disks on a SiO_2/Si substrate and a monolayer of MoS_2. A photoluminescence enhancement for the MoS_2 on the disk arrays for two different pump frequencies is presented. It is shown that this enhancement was due to the absorption enhancement within the MoS_2 layer when the Si disks were present. This system is further optimised to show that a layer of Au underneath the SiO_2 layer can act as a back-reflector to enhance the absorption of the MoS_2 and Si disk hybrid system.

Chapter 7 gives a conclusion drawn from the results found in this thesis. A discussion on the future work regarding the three systems investigated is also laid out.

> Remember to look up at the stars and not down at your feet.
>
> Stephen Hawking

2 Background

2.1 2D Materials

2.1.1 Graphene

Two-dimensional materials are an interesting class of nanomaterials. At the monolayer limit, they are shown to have highly different properties compared to their bulk counterparts[26]. Additionally, due to their atomic thicknesses, they can easily be integrated with other devices[27]. 2D materials were originally thought of in a theoretical context only. This is because studies showed that they would be unstable at the monolayer limit[28, 29]. The first study on monolayer graphene was conducted in 1947 by Wallace[30] to investigate the electronic energy bands. It wasn't until over 50 years later, in 2004, when the first reproducible fabrication method was developed by Novoselov and Geim[14]. This was achieved with the very simple approach of mechanical exfoliation. Layers were repeatedly pealed away from highly-oriented bulk pyrolytic graphite with scotch tape until a single graphene layer remained. This was an important discovery because of graphene's many unique properties, including its high electrical conductivity, and its high chemical stability[31, 32, 33, 34]. After the first fabrication of 2D graphene sheets, many doorways were opened to new science, exploiting its interesting new properties.

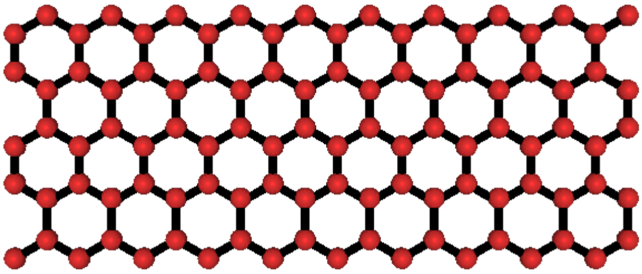

Figure 2.1: Honeycomb structure of sp^2 hybridised carbon atoms.

This discovery was the inspiration for many other studies to investigate the fabrication and properties of the atomically thin graphene sheets. Since the development of the scotch tape method, many other fabrication techniques were established[35]. It was important to develop other fabrication methods, because while the mechanical exfoliation method showed promising results of monolayer graphene flakes with high crystallinity, there was minimal control over the flake size and how much bi- and multi-layered graphene sheets surrounded the desired monolayer product. Other methods of graphene growth include liquid phase exfoliation[36], flame synthesis[37], pulsed laser deposition[38] and chemical vapour deposition (CVD)[33]. CVD was chosen as the technique of fabrication for this work due to its high monolayer coverage[33, 34].

Graphene consists of a monolayer of carbon atoms in a honeycomb formation, as shown in figure 2.1. It is the thinnest of the 2D materials, with a thickness of 0.34 nm[39, 40, 41]. Each carbon atom is covalently bonded to its three nearest neighbours, with nearest-neighbour distance being 1.42 Å[26]. A lone carbon atom has an electric configuration of $1s^2 2s^2 2p_x^1 2p_y^1 2p_z^0$ in its ground state, with the $2p_x$, $2p_y$ and $2p_z$ states all being degenerate. Figure 2.2 shows the 2s (sphere-shaped) and two 2p (dumbbell-shaped) orbitals. In a monolayer of graphene, these electron orbitals combine to form three new, degenerate energy electron orbitals, sp^2 hybridised. The energy of these new orbitals are between the energy of the original s and original p orbitals. The shapes of the sp^2 orbitals are also shown in figure 2.2, as well as their positions in relation to each other and the carbon atom nucleus. In all orbitals shown in figure 2.2, the carbon nucleus is at the origin of the x and y axes shown.

Each carbon atom in the graphene sheet bonds with its three nearest neighbours, as shown in figure 2.1. A schematic of these bonds is shown in figure 2.3, with example sp^2 orbitals shown in red and example p orbitals shown in blue. As previously discussed, the 2s, $2p_x$ and $2p_z$ orbitals form three new hybridised orbitals, while the $2p_z$ orbital remains unchanged. A σ covalent bond is formed between the sp^2 orbitals of adjacent carbon atoms. A weaker π bond is also formed between the $2p_z$ orbitals of adjacent atoms. This results in small spacings between atoms in the graphene sheet, and incredibly strong bonds. Carbon nanotubes (sheets of rolled-up graphene) are the strongest known material because of this[42, 43]. It is even stronger than diamond, which consists of sp^3 hybridised orbitals around carbon atoms. The out of plane π bonds cause van der Waals attraction between separate sheets of graphene.

The band structure of graphene is particularly interesting because of its zero band-gap between the conduction and valence bands[26]. This allows graphene to conduct electrons as a metal does. This band structure can be modified by several different methods. For monolayer graphene, the conduction band and valence band touch only at Dirac points, giving rise to the zero band gap nature. In bilayer graphene, the out of plane $2p_z$ orbitals interact with the

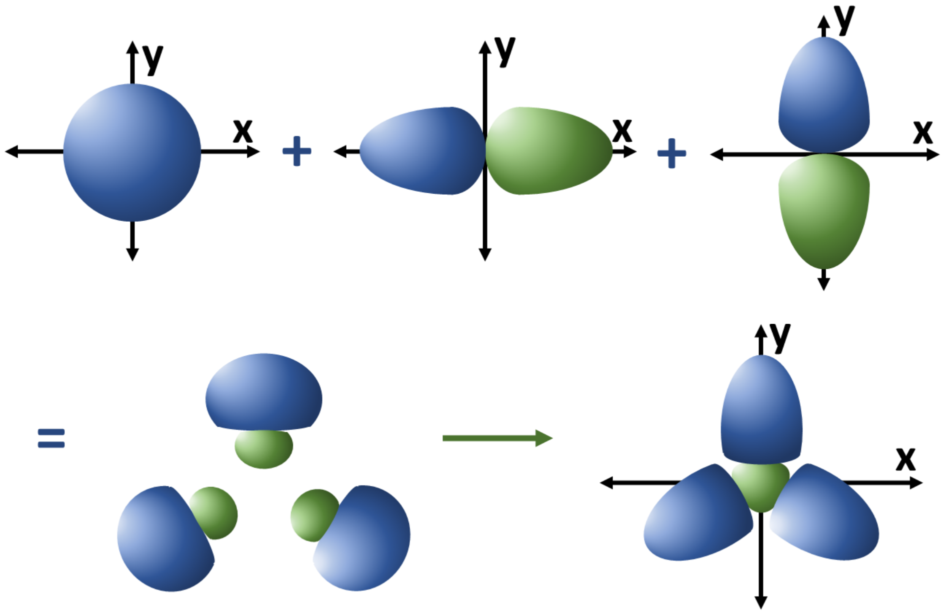

Figure 2.2: Hybridisation of the 2s, $2p_x$ and $2p_z$ orbitals to make three separate sp^2 orbitals in the graphene honeycomb structure. The combination of the three sp^2 orbitals positioned around a carbon nucleus is also shown. These three hybridised orbitals bond with the three nearest neighbour carbon atoms in graphene. The carbon atom nucleus is positioned at the origin of the x and y axes shown.

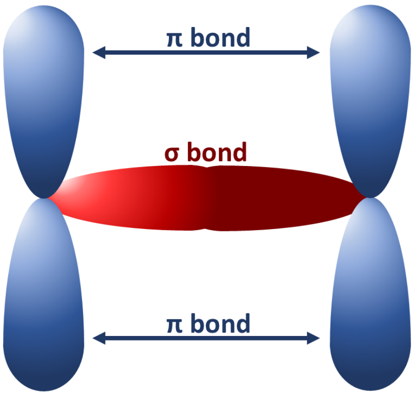

Figure 2.3: Schematic of two nearest neighbour carbon atoms bonding each other in a sheet of graphene. The two red orbitals describe the hybridised sp^2 orbitals in a covalent σ bond. The two blue orbitals describe the $2p_z$ orbitals in a covalent π bond. Similar bonds occur for each carbon atom in the graphene sheet and their three nearest neighbours.

other $2p_z$ orbitals in the other graphene layer. This gives rise to a zero-energy band, no longer being confined to a single Dirac point. For trilayer graphene, there is a finite overlap between the valence and conduction bands, making it a semi-metal[44]. As more layers of graphene are added, the band structure quickly changes, becoming almost identical to graphite with 10 layers[45].

The band structure of graphene can also be modified by doping the graphene, both electrically and chemically[46, 47, 48]. This is illustrated in figure 2.4. The linear dispersion around the point of zero band-gap is approximated as a cone. For pristine, undoped graphene, the Fermi level is at the Dirac point, with the occupied density of states below the Dirac point, and the unoccupied density of states above (see figure 2.4a). When the graphene is p-doped, the Fermi energy is displaced to a lower point with respect to the Dirac point as shown in figure 2.4b. Similarly, when the graphene is n-doped, the Fermi energy is displaced to a higher point with respect to the Dirac point as shown in figure 2.4c.

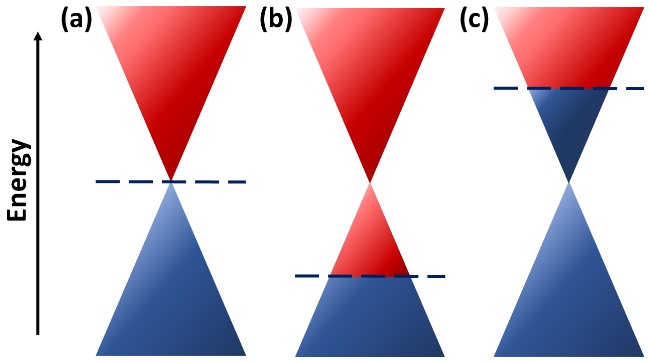

Figure 2.4: Dirac cones of (a) undoped, (b) p-doped and (c) n-doped graphene. The blue parts of the cones depict the occupied density of states, while the red parts of the cones depict the unoccupied density of states. The Fermi level is indicated by the dark blue dashed lines.

The graphene used in this thesis is doped chemically with nitric acid (HNO_3). This method causes the graphene to be p-doped, due to adsorbed atoms and molecules on the graphene surface[49]. According to D'Arsié *et al.*, the HNO_3 molecules dissociate into two radical types and water molecules after physisorbing onto the graphene lattice according to the following equation:

$$2HNO_3 \rightarrow NO_2^0 + NO_3^0 + H_2O \tag{2.1}$$

The two radicals formed have an energy state below the Fermi energy of the graphene only occupied by a single electron. Therefore, they each attract an electron from the graphene into their lower-energy states, forming NO_2^- and NO_3^- anions. Two holes are created in the graphene by this, causing the p-doping. The NO_2^- and NO_3^- are kept adsorbed by the graphene, bound by the Coulomb force between the anion and the positive hole formed in the graphene. The bond length between the carbon atoms in the graphene is too long for the anions to bond to more than one carbon atom, which minimises changes in the relative positions of the carbon atoms in the lattice. This keeps the quality of the graphene high, which can be observed in the absence of the D peak in the Raman spectrum after the graphene has been doped with Nitric acid. The D peak will be discussed further in section 3.4.1.

2.1.2 MoS_2

The discovery of graphene inspired many scientists to investigate other 2D materials, such as transition metal dichalcogenides (TMDCs). Today, there are over 40 known TMDCs[50]. These are a class of 2D material, with the formula MX_2, where M is a transition metal atom (group 4-12 in the periodic table) and X is a chalcogen atom (group 16 in the periodic table). In the bulk, layers of TMDCs are held together by van der Waals forces[50], as is the case for graphene. In this work, MoS_2 (a TMDC) is used as a 2D material in chapters 5 and 6. MoS_2 is one of the most stable layered dichalchogenides[51], with an A exciton with energy in the visible region. It is a preferable two-dimensional material to WSe_2 (a TMDC with a similar A exciton energy[52]) due to its relative ease of synthesis. This is because sulfide precursors are more reactive than selenium precursors and because WO_3 is more difficult to sublimate than MO_3 (boiling points being at $1700°C$ and $1155°C$, respectively).

Atoms are arranged differently in TMDCs than they are in graphene, because there are two different types of atoms within each layer. Within one layer of crystalline 2H-MoS_2, for example, the Mo atoms are arranged in a hexagonal lattice, with 6 equidistant Mo atoms surrounding each individual Mo atom. This is sandwiched between two layers of S atoms, both also arranged in a hexagonal lattice. Each Mo atom is bonded covalently to six S atoms, three in the S hexagonal lattice above the Mo layer, and three in the S hexagonal lattice below the Mo layer. Each S atom is bonded covalently to three Mo atoms. The covalent bonds are between the 4d orbitals in the Mo atoms and the 3p orbitals on the S atoms[53]. This structure is represented in figures 2.5a and b, with a view from above, and a view from the side, respectively. The thickness of MoS_2 is 0.65 nm[54].

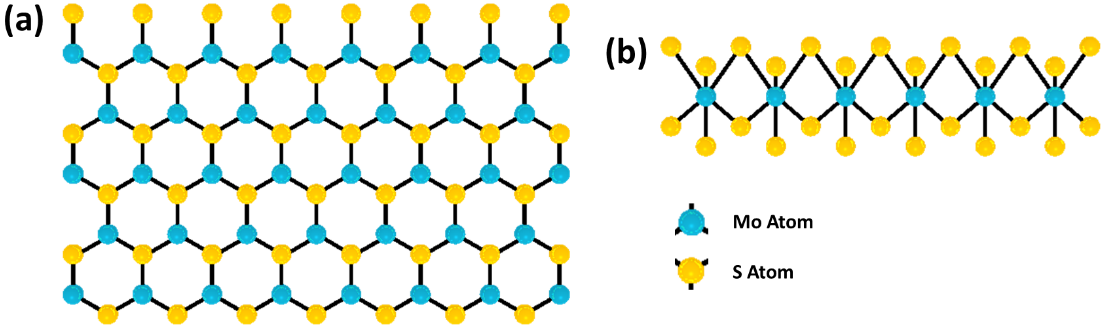

Figure 2.5: (a) Top view and (b) side view of a single layer of MoS_2.

MoS_2 can be fabricated by mechanical exfoliation, CVD[54] and liquid phase exfoliation[55]. Small monolayer coverage is also possible with pulsed laser deposition[56]. MoS_2 is interesting as a 2D material because the band-structure changes for the single layered and few layered case. At the monolayer limit, the indirect band-gap becomes a direct band-gap[57] (see figure 2.6). This property can be exploited for many applications, for example, a low threshold laser[58].

The band-structure of MoS_2 is highly dependent on the number of layers because of the quantum confinement in the atomic thickness of a MoS_2 monolayer[59]. For bulk MoS_2, the highest energy in the valence band is at the Γ point in the band structure. There is also a local maximum of high energy in the valence band at the K point. The conduction band minimum is between the Γ and K points, making an indirect band-gap transition between the minimum (between the Γ and K points) of the conduction band and the maximum (Γ point) of the valence band. The overall energy between the highest valence band and the lowest conduction band is increased as the number of layers in few-layer MoS_2 is reduced. This is because the lowest conduction band increases in energy as the number of layers is reduced. Only a small increase in energy occurs at the K point because these states are primarily due to the 4d orbitals of the Mo atoms. As previously discussed, the Mo atoms form an intermediate layer between two layers of S atoms, and therefore are not affected as heavily by the external environment, or numbers of layers of MoS_2. The energy of the conduction band increases much more quickly at the Γ point because these states are primarily due to the hybridised 4d and 3p orbitals of the Mo and S atoms, respectively. Therefore, as the number of layers decreases, the Γ point in the conduction band increases in energy at a quicker rate than the K point. Similarly, the energy of the valence band also decreases at the Γ point, further increasing the band-gap, but less at the K point. When the monolayer limit is reached, the minimum between the Γ and K points in the conduction band is at a higher energy than the minimum at the K point. This means that the direct band-gap (K to K) is smaller than the indirect (Γ to the point between Γ and K) gap[60]. This effect is illustrated in figure 2.6. This transition from an indirect to a direct band-gap when it is a monolayer makes MoS_2 a particularly interesting material with a myriad of potential applications such as sensing, flexible electronics and optoelectronics[61, 62].

A MoS_2 monolayer has two main excitons, the A and B excitons[63]. Excitons are electron-hole pairs that can exist in insulators and semiconductors, which can be excited by incoming photons. The first study theorising excitonic excitations was carried out in 1931 by Frenkel[64]. He hypothesised that absorbed light is not confined within one atom, but

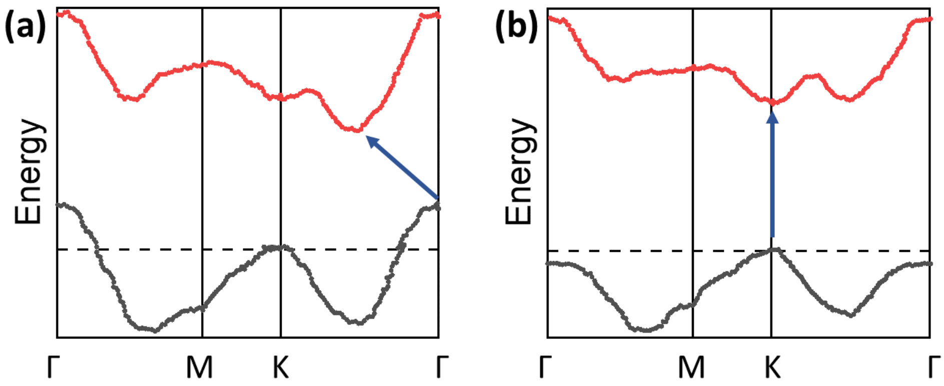

Figure 2.6: Band structure of highest energy valence band and lowest energy conduction band for (a) bulk and (b) monolayer MoS_2. Blue arrows indicate the (a) indirect and (b) direct band gap. These plots were adapted from Splendiani *et al.*[59].

---

the excitation can be passed through the material in the form of an 'excitation wave'. There would be no transfer of charge with this wave, because an exciton is a bound electron hole pair, with a net zero charge.

The A exciton of MoS_2 has energy of $\approx$ 1.92 eV, and the B exciton has energy of $\approx$ 2.08 eV[15]. These excitons are caused by the spin-orbit coupling of electrons in the valence band of MoS_2. The highest band splitting occurs at the K point of the highest energy valence band of MoS_2. This gives two possible transitions of electrons to the conduction band, giving rise to the A and B excitons.

As with graphene, the band structure of MoS_2 can be modified by applying a voltage. This is due to the formation of trions[65]. These can take the form of two electrons coupled to one hole, or two holes coupled to one electron, depending on the gate bias. The application of a gate voltage and the introduction of trions into the MoS_2 modifies the band gap energy. The trions are observed to have a lower binding energy than the excitons[60, 66].

The excitonic energies can be probed by both the absorbance and the photoluminescence (PL) spectra of MoS_2. The PL has a quantum yield of 10^4 times higher than the bulk[15]. This is because the excitonic energy is highly absorbed by bulk MoS_2. The absorption is significantly less in the monolayer case due to the presence of the direct band-gap. The complex refractive index and permittivity is shown in figure 2.7a and b, respectively. The two peaks shown for the imaginary permittivity between 600 and 700 nm correspond to the A and B excitons[67].

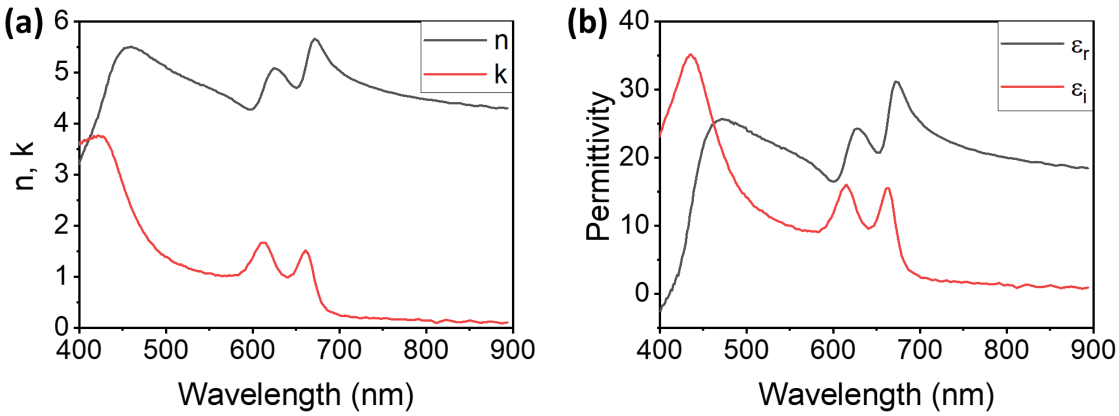

Figure 2.7: (a) Refractive index and (b) Permittivity for monolayer MoS_2 used for FDTD simulations and taken from Jung *et al.*[67].

2.2 Plasmons

Plasmons are oscillations of electrons at a metal interface which are excited with incident light. The two types of plasmons are surface plasmon polaritons (SPPs) and localised surface plasmon resonances (LSPRs). A SPP is when a plasmon propogates over the surface of a bulk metal. LSPRs are the non-propogating oscillation of an electron cloud within a metal nanoparticle. This work will focus on LSPRs.

For a LSPR, the nanoparticles need to be smaller than the wavelength of the incident light. The incident light acts as a driving force, causing an oscillation of the electron cloud within the nanoparticle. As the electrons are displaced from their ground states, the Coulomb force acts as a restoring force between the displaced electrons and the nuclei of the metal atoms of the nanoparticle. This effect is demonstrated in figure 2.8.

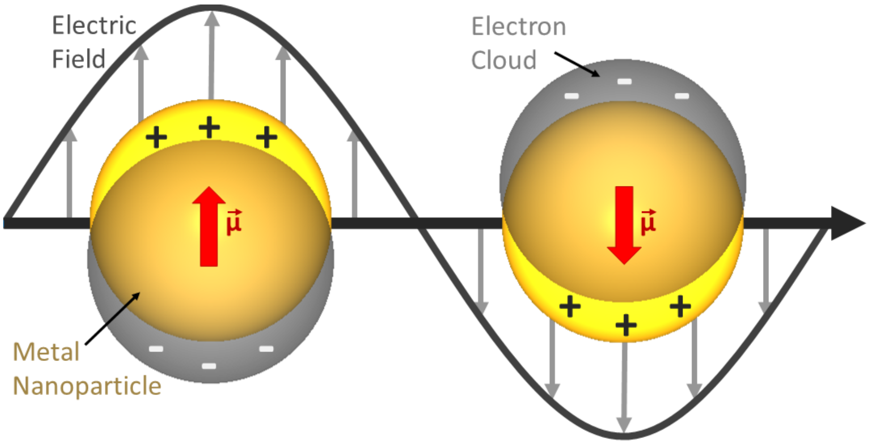

Figure 2.8: Schematic of a LSPR in a metallic nanoparticle, with the dipole moment marked as $\vec{\mu}$.

As shown, the oscillating electrons are confined by the surface of the metal nanoparticle.

This causes a significant near field enhancement around the edges of the nanoparticle[68]. By modifying the nanoparticle shape by adding sharper points on the surface, the electric field at the surface can be even further enhanced. Manipulating the size and shape of metal nanoparticles can allow for great control over the resonant frequency of the nanoparticles, as well as allow for stronger electromagnetic field strength and field confinement. The confinement can be localised at particular sides of the nanoparticle by exciting the nanoparticle with polarised light[24]. It is also possible to design a nanoparticle with an elongated axis so the plasmonic oscillation is polarised in a single direction, regardless of the polarisation of the incoming light. This will be discussed further in chapter 5.

The resonant frequency of the plasmon is the energy of the specific wavelength of light the plasmonic nanoparticle absorbs, resulting in an electron oscillation within the nanoparticle. It can be controlled by the metal, size and shape of the nanoparticle. The light-matter interactions at the nanoparticle are strongest at the resonant frequency. These two interactions are the absorption (σ_{abs}) and the scattering (σ_{scat}). The extinction cross section is found by

$$\sigma_{ext} = \sigma_{abs} + \sigma_{scat} \tag{2.2}$$

The extinction cross section of a nanoparticle can be up to ten times larger than the nanoparticle's geometric cross section[69]. This is due to the large electromagnetic field around the nanoparticle after it has been excited with electromagnetic light[70]. The high cross section of nanoparticles interacting with light give a myriad of potential applications in photonic devices. These include applications in biosensing[20] and in solar cells[21, 22].

The polarisability of a nanoparticle, α_P, is defined as the ratio between the dipole moment induced in a nanoparticle by an incident electromagnetic wave (μ) and the amplitude of the displacement field of the incident electromagnetic wave (D). Therefore

$$\alpha_P = \frac{\mu}{D} = \frac{\mu}{\varepsilon_0 \varepsilon_d E_0} \tag{2.3}$$

where ε_0 is the permittivity of free space, ε_d is the permittivity of the surrounding dielectric and E_0 is the amplitude electric field strength of the incident light. By considering the simplest case of a metallic nanosphere with a diameter lower than the wavelength of the incident light, the polarisability can be described by[71]

$$\alpha_P = 4\pi R^3 \frac{\varepsilon(\omega) - \varepsilon_d}{\varepsilon(\omega) + 2\varepsilon_d} \tag{2.4}$$

where R is the nanosphere radius and $\varepsilon(\omega)$ is the metal permittivity. Therefore, the LSPR peaks where α_P is strongest.

The polarisability, α_P, and therefore the dipole moment, μ, is strongest when $\varepsilon(\omega) = -2\varepsilon_d$, to minimise the denominator in equation 2.4. This is known as the Fröhlich condition[72]. The Fröhlich condition shows that the polarisability strongly depends on permittivity of both the nanoparticle and the surrounding medium. Therefore, the substrate a nanoparticle is drop-cast onto must be considered when utilising the LSPRs of nanoparticles. The absorption, (σ_{abs}) and scattering, (σ_{scat}) are both greatly enhanced when the Fröhlich condition is met[71], due to the increase in the polarisability (α_P). It is therefore important to meet the Fröhlich condition to maximise the light-matter interaction with the nanoparticle.

Au and Ag are commonly used as metals for plasmonic nanoparticles because of their negative permittivity in the visible wavelength region. This enables them to satisfy the Fröhlich condition. Ag has a sharper plasmonic resonance than Au due to the real part of the permittivity being more negative for Ag in the visible region[73]. It is not favoured for fabricating nanodevices, however, as it is easily tarnished over time[74]. Au is used for the nanoparticles in this work because of this.

Equation 2.4 describes the polarisability of the simplest-case, spherical particle. It can give trends for other shapes of nanoparticles too, but as the shape is altered, other factors also come into effect. The scattering and absorption are strongly influenced by changes in the size and shape of the nanoparticle. This is discussed in greater detail in the results presented in chapter 5.

This work aims to modify the plasmon resonances of nanoparticles by coupling them to 2D materials (graphene and MoS_2), as well as to increase the light-matter interaction with the active excitonic material of MoS_2. To achieve this, strong field enhancements and high field confinements are essential to fully integrate the atomically thin 2D materials with the plasmonic devices. Many recent studies have investigated the coupling of plasmonic nanoparticles with 2D materials. They have demonstrated the electric control of plasmonic modes by electric gating of the 2D material[66, 75], and increased light-matter interaction[76, 77, 78]. It remains a challenge, however, to maximise the overlap between the nanoparticle's electric field hot-spot and the 2D material it is coupled to. Chapters 4 and 5 aim to show two different methods to improve these limitations. In chapter 4, a localised electromagnetic hot-spot within a layer of graphene is achieved by creating a nanometer-wide gap between a spherical nanoparticle and a metal film, with the graphene as an intermediate layer in the nanoparticle-on-mirror system. In chapter 5, the electric field strength is increased and confined within a MoS_2 layer underneath by designing metal nanoparticles to have a sharp tip, pointed down towards the MoS_2.

2.3 Dielectric Nanoparticles

So far, we have seen how metallic nanoparticles can be designed to enhance electric field strength and confinement, increasing the light-matter interaction. Metallic nanostructures have numerous advantages for this purpose, offering unparalleled concentration of light into the subwavelength scale. The highest electric field strength of an excited metallic nanoparticle is positioned outside of the particle, giving the advantage of allowing easier coupling to other materials. However, metallic nanostructures also suffer from some draw-backs such as high absorption losses and heating. These lead to broad plasmonic resonances and short lifetimes[79]. A broad resonance is a major draw-back, because it reduces sensitivity in measurements. Additionally, as will be seen in section 2.4, the condition of strong coupling is for the exchange of energy between a plasmon and a cavity or quantum emitter to be faster than their intrinsic dissipation rates. This effect is more likely to be realised if the resonance has a longer lifetime, thus signifying another draw-back for metallic nanoparticles. Further, metal nanoparticles are generally fabricated with metals such as Au or Ag. This can be very expensive to fabricate, reducing their utility[80]. Additionally, colloidal metallic nanoparticles synthesised in a solution are not precisely placed and oriented. This issue can be overcome by methods such as electron beam lithography, but this fabrication technique comes at the cost of higher defects[11], resulting in a lower sharpness and a lower electric field strength.

Dielectric nanoparticles can offer several advantages over the metallic nanoparticles previously discussed. Similar to metallic nanoparticles, dielectric nanoparticles have resonances with energies that can be tuned by optimising their size and shapes. In contrast to metal nanoparticles, dielectric nanoparticles hold several advantages, including their very low absorption losses, especially in the visible-to-near-infrared region[81]. This has the effect of sharpening the resonances and increasing the lifetime. Additionally, they are generally much more cost-effective materials, making them preferable as a potential material for day-to-day applications.

The excitation of a dielectric particle with an incident electromagnetic wave is in the form of both magnetic and electric multipolar modes. These can be described by Mie resonances, which were formulated in 1908 by Gustov Mie[13]. Mie theory describes the light scattered by a single nanosphere placed in homogeneous surroundings, with diameter similar to the wavelength of the incident light. The Mie resonances occur because the incident light excites circular displacement currents inside the dielectric material of high permittivity. This creates a strong magnetic response[80]. Mie theory describes the scattered light as a series of infinite harmonics, with the two lowest-order modes (with the lowest frequencies) being the magnetic and electric dipole modes[82]. Mie theory only describes the resonances for a perfect sphere in a homogeneous medium, but Mie-like resonances also occur for other dielectric nanostructures[83]. This has been demonstrated in Si nanodisks[84, 85], with the multipolar resonances being manipulated in the visible range. This effect will be utilised in chapter 6.

Many materials can be used to give similar Mie resonances. In particular, III-V semiconductors have a strong light-matter interaction and a non-linear response. This is due to their direct band-gap[86]. Silicon also has many advantages, primarily due to the already existing fabrication technologies and the possibility of integrating it with on-chip photonics and established silicon optics.

As for plasmonic resonances, the shape, size, material and periodicity of the elements in a metasurface are designed and fabricated to give control over the desired direction, phase and polarisation of the wavefront. The multipolar resonances in a dielectric nanostructure can be tuned to overlap and interfere with each other[87]. This gives an extra degree of freedom with which to control the photonic response[84]. The manipulation of the multipolar modes to supress back-scattered light is know as the Kerker effect[88]. This effect is useful as it enhances and concentrates the electric field within the dielectric structure and controls the directionality of the scattered light. A high level of control can be achieved with structures such as this, with a model of the multipolar modes successfully replicating observed experimental reflectance data[84].

Metasurfaces can be fabricated with arrays of dielectric nanoresonators. These can have a wide variety of functionalities and applications. A metasurface of a periodic array of tuned Si disks can be used as a near-perfect reflector due to its magnetic and electric dipole resonances. A high reflectivity of average 98% was achieved over a range of wavelengths as broad as 200 nm[89]. Other research has been carried out to demonstrate focusing lenses in the infrared region, fabricated from a dielectric metasurface[16]. It is also possible to create a lens with multi-wavelength operations to increase the utility. This can allow for fluorescence to be excited and collected at two different wavelengths[17].

2.4 Coupling between Excitons and the Modes in a Plasmonic or Dielectric Structure

2.4.1 Weak Coupling Regime

When the energy of a plasmon is close to the energy of an exciton, they can couple together and demonstrate many different effects. When the coupling has no perturbation effect on the exciton and plasmon wave functions, it is called weak coupling.

Weak coupling can enhance or quench a system's emission, modifying the decay rate. This was first observed in 1995 by Purcell[90], demonstrating that the spontaneous emission rates of atoms were different when they were in a microcavity to when they were in free space. The Purcell factor is written as

$$F_P = \frac{\gamma_c}{\gamma_0} \tag{2.5}$$

where γ_c is the spontaneous radiative emission rate of the emitter within the cavity, and γ_0 is the spontaneous radiative emission rate of the emitter in free space.

The absorption of the emitter can also be modified by the presence of the LSPR[91]. The change in both the absorption and the emission of the quantum emitter in the presence of the LSPR leads to the enhancement or quenching of the overall fluorescence. This modification of the fluorescence of a quantum emitter is characteristic to the weak coupling regime. This effect is discussed more thoroughly in chapter 6. A high degree of control of the weak coupling effect in a system can be achieved by modifying the LSPR in the vicinity of the emitter[85]. This is because the weak coupling is a result of the emitter interacting with the local electromagnetic field.

The weak coupling regime has many important applications. One important application is surface enhanced Raman scattering (SERS). The first observation of SERS was in 1974 by Fleischmann *et al.*[92] where the Raman spectrum of pyradine was obtained on a rough Ag surface. The enhancement factor, M_{EM} is given as[93]

$$M_{EM} = \frac{|E_L(\omega_1)|^2}{|E_I(\omega_1)|^2} \times \frac{|E_L(\omega_2)|^2}{|E_I(\omega_2)|^2} \tag{2.6}$$

where E_L and E_I are the amplitudes of the local and incident fields, respectively and ω_1 and ω_2 are the frequencies of the pump laser and the Raman scattered light, respectively. SERS is a very powerful characterisation tool, opening avenues to explore the properties of materials that would otherwise be difficult to identify. SERS can make it possible to detect materials on the single molecule level[94]. The maximum single molecule SERS enhancement factors are typically on the order of 10^{10}[95].

Another important application of the weak coupling effect is the fabrication of solar cells. The weak coupling regime can modify the absorption of a system. By designing a system to achieve maximum absorption, it is possible to harvest more energy from a small amount of material. This gives potential for a method of harvesting solar energy with a compact solar cell device[21].

2.4.2 Strong Coupling Regime

Strong coupling can occur between an optical cavity and a quantum emitter, or in the case of this thesis, a plasmon and an exciton. The strong coupling regime is reached when the rate of exchange of energy between the plasmon and exciton is quicker than their intrinsic dissipation rates[21]. In this regime, in contrast to the weak coupling effect, the wave functions of the plasmon and exciton are perturbed by their interaction. This means that the energy of the strongly coupled system is not only enhanced or quenched, but splits into two entirely new energy states. This is called Rabi splitting[96]. These new states are a light-matter hybrid and are known as polaritons. The energy of these new states can be measured from the scattered light. Rabi splitting gives rise to a characteristic anti-crossing pattern, meaning that the two new eigenstates have energy above and below that of the original plasmon and exciton[52, 66, 97, 98, 99, 100]. Examples of this effect are demonstrated in chapter 5. An illustration of this effect, contrasted with the weak coupling effect, is demonstrated in figure 2.9.

In the past, Rabi splitting was realised with closed optical cavities coupled to quantum emitters[99, 101]. These structures were on the micrometer scale and required cryogenic temperatures for the strong coupling to occur. With recent developments in nanoscience, many studies have now shown that Rabi splitting is possible even at room temperature[52, 66, 97, 98, 102]. For example, many studies have shown a large quantity of randomly oriented J-aggregates could strongly couple with the modes of plasmonic nanostructures[103, 104, 105]. Plasmonic nanoparticles have also been used to couple with TMDCs[52, 66, 106, 107], with the nanoparticles placed on top of the monolayer TMDC on a substrate. The studies have shown the potential to realise Rabi splitting with a variety of different nanoparticle shapes and TMDCs, investigating the effects of changing the number of layers in the TMDC[52], the effect of back-gating the TMDC[66] and the effect of changing the plasmon resonance energy[106, 107]. Many different shapes of nanoparticle have been investigated, including rods, cubes, prisms and bipyramids. This will be explored in chapter 5.

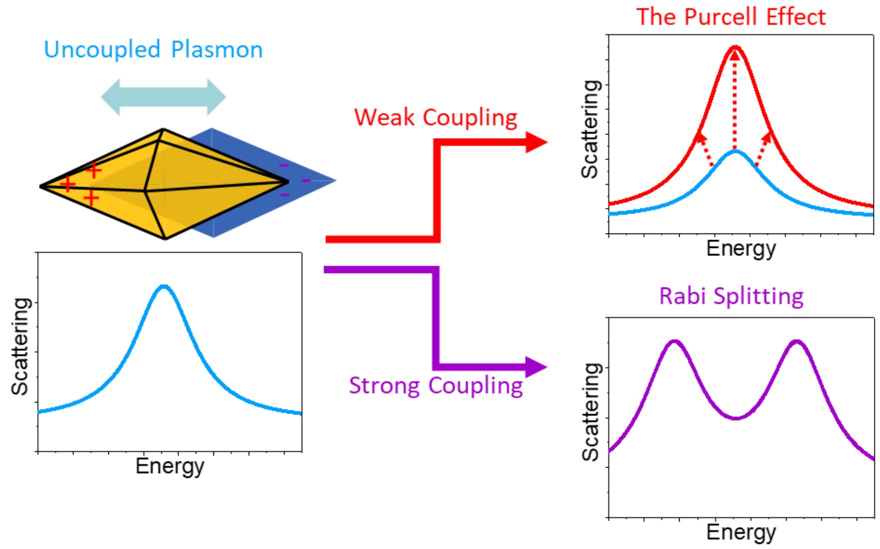

Figure 2.9: Typical scattering spectra of plasmons coupled to exctions are shown. The longitudinal quantised oscillation of the electron cloud in a bipyramid (as in chapter 5) gives the single-peak scattering spectrum (blue). The plasmon weakly coupled to an exciton gives another single peak, enhanced or quenched (red). The plasmon strongly coupled to an exciton splits into two separate eigenstates (purple).

The strong coupling behaviour in Rabi splitting can be approximated by using a coupled oscillator model of a spring pendulum[98]. Numerical simulations can be used to give reasonably accurate predictions, taking into account the size and shape of the nanoparticles under study[102]. The approximation given by Stete *et al.*[98], however, shows a better conceptual understanding of the effect. The plasmon and exciton are modelled as two pendula, X and Y, attached to separate springs and one spring in between them, with the plasmon (pendulum X) being excited by an external force (incident light). A sketch of this model is shown in figure 2.10.

The spring in between the two pendula couples their oscillation, giving the coupling constant, g. The resonance frequencies of the two pendula are given as ω_x and ω_y, their masses as m_x and m_y and their damping as γ_x and γ_y. For a simplified study, we will assume that both oscillators have the same resonance frequency ($\omega_x = \omega_y = \omega_0$), and the same mass ($m_x = m_y = m$). The plasmon damping is much higher than that of the exciton in the system studied, so γ_x and γ_y are kept as separate values. The external force, F, on the coupled system, with frequency ω, is the incident light. It is assumed that only the plasmon (oscillator X) is excited by the incident light (force F). The equations of motion can therefore be written as:

$$\ddot{x} + \gamma_x \dot{x} + \omega_0^2 x + gy = \frac{F}{m} e^{-i\omega t} \tag{2.7}$$

$$\ddot{y}+\gamma_y\dot{y}+\omega_0^2 y+gx=0 \tag{2.8}$$

where x and y are the distances the oscillators X and Y have been displaced, respectively.

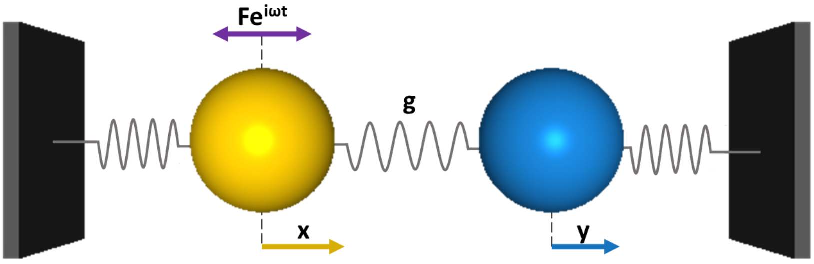

Figure 2.10: Sketch of the two coupled oscillator model, the plasmon, X (gold) and exciton, Y (blue)

The complex amplitudes are then given as:

$$A_x=\frac{\omega_0^2-\omega^2-i\gamma_y\omega}{(\omega_0^2-\omega^2-i\gamma_x\omega)(\omega_0^2-\omega^2-i\gamma_y\omega)-g^2}\frac{F}{m} \tag{2.9}$$

$$A_y=\frac{g}{(\omega_0^2-\omega^2-i\gamma_x\omega)(\omega_0^2-\omega^2-i\gamma_y\omega)-g^2}\frac{F}{m} \tag{2.10}$$

The absorption of the plasmon, oscillator X (Abs_x), and the exciton, oscillator Y (Abs_y), are given by the loss due to friction. Therefore,

$$Abs_x=-m\gamma_x\dot{x}^2=-\frac{m\gamma_x}{2}(\omega|A_x|)^2 \tag{2.11}$$

and

$$Abs_y=-m\gamma_y\dot{y}^2=-\frac{m\gamma_y}{2}(\omega|A_y|)^2 \tag{2.12}$$

The scattering for the plasmon ($scat_x$) and exciton ($scat_y$) are given by:

$$scat_x \propto \omega^4|A_x|^2 \tag{2.13}$$

and

$$scat_y \propto \omega^4|A_y|^2 \tag{2.14}$$

It was found that, according to these equations, the resonance frequency of oscillator X (plasmon) splits in two as soon as the coupling is turned on, while for the other oscillator, Y (exciton), the splitting happens only when the coupling, g is at least $(\gamma_x+\gamma_y)/2$. This is the condition for the realisation of strong coupling, and it has been reported in several articles[52, 98, 96, 108]. The difference between the two oscillators is due to the numerator in the amplitude equations 2.7 and 2.8. The minimum for A_x is at $\omega=\omega_0$ when $g>0$. This is a Fano-like interference, causing an anti-resonance. The splitting of the Y oscillator in this system indicates the presence of Rabi splitting.

In the weak coupling case, the only driving force acting on oscillator Y is from oscillator X. The oscillators have the same resonance frequencies, resulting in a phase shift of $\pi/2$ between the two oscillators. For the weak coupling case, the intrinsic decay of the oscillator Y, γ_y, is weaker than the coupling force. Oscillator Y therefore gives a feedback force on oscillator X, opposing the original driving force, and phase-shifted by exactly π from the original force acting on oscillator X. This is the main part of the energy because the coupling is stronger than the decay channel for oscillator Y. This reduces the oscillation amplitude of the X oscillator at ω_0 due to this feedback force counteracting the original driving force. This causes the dip in the coupled resonance spectrum, known as Fano interference.

In the strong coupling case, feedback from oscillator X to oscillator Y must be possible. This means that the feedback from X to Y must be faster than any other decay channel, the rate of exchange of energy between the oscillators being faster than their intrinsic dissipation rates. The feedback from X to Y is then phase-shifted by π from the original driving force. This cancels with the original driving force from X to Y, meaning no energy is transferred to Y. At least one oscillation period relative to both oscillators must be completed for the strong coupling condition to be met. In practise, the feedback force will be slightly less than the original driving force, but the gap narrows as the coupling becomes stronger.

This is a simplified model and is not as accurate in predictions of experimental data as numerical simulations would be. However, similar trends have been found in numerical simulations by Antosiewicz *et al.*[102], showing that it is a good qualitative analysis to understand the origins of Rabi splitting.

The coupling constant is given by[52, 97]:

$$g = \sqrt{N}\mu_e|E_{vac}| \propto \mu_e\sqrt{\frac{N}{V}} \tag{2.15}$$

where N is the number of emitters or excitons coupled into the system, μ_e is the transition dipole moment of the quantum emitter, E_{vac} is the vacuum field and V is the resonance mode volume. Typical scattering specta for both the Purcell effect and Rabi splitting for a longitudinal plasmon resonance of a bipyramid are shown in figure 2.9.

In chapter 5, Rabi splitting is achieved between the longitudinal plasmon of a Au bipyramid and the A exciton of monolayer MoS_2. It is demonstrated that a bipyramid is an ideal geometry to achieve the strong coupling effect due to its sharp tips, resulting in a large electric field enhancement and confinement. The tips of a bipyramid can remain equally sharp for a large bipyramid as for a small one, resulting in a greater electric field strength concentrated in an equally small volume when the bipyramid size is increased. Additionally, bipyramids are an interesting structure for Rabi splitting due to their natural alignment, with one tip pointed towards the substrate, directing the plasmon resonance towards the exciton that it is coupling to.

Rabi splitting gives rise to a large range of important applications[21, 109]. These include the control and modification of the rate of a chemical reaction[110, 111, 112], a low threshold laser[113], quantum sensing[20], a photon blockade[114, 115] and quantum entanglement for quantum information processing[23].

The rate of a chemical reaction can be modified by coupling the vibrational modes of a molecule to an optical cavity. Thomas *et al.*[112] found that the rate of chemical reaction was increased with a higher Rabi splitting strength, using the desilylation of 1-phenyl-2-trimethylsilylacetylene (PTA) as the chemical reaction under study. Interestingly, the Rabi splitting was shown to have a significant impact on the reaction rate, despite the splitting energy being much weaker than the transition state energy of the reaction. Pang *et al.*[111] showed that the strong coupling worked to promote or impede chemical reactions by selecting the vibrational modes to couple with to match the symmetry of the desired products. This study was carried out by investigating the charge transfer complexation of trimethylated benzene as a donor and iodine as an acceptor.

Noda *et al.*[113] demonstrated how the strong coupling between a cavity in a photonic crystal and an emitter can be used to design a low threshold laser. This is achieved by gaining control over the spontaneous emission of an emitter via the strong coupling regime. A thin, freestanding semiconductor slab structure with an array of holes was utilised. When the emission energy overlapped with the photonic band gap of the photonic crystal, the spontaneous emission was suppressed parallel to the substrate, but enhanced in the vertical direction. This lead to an overall increase in PL lifetime. With the introduction of a nanocavity to the photonic crystal, the PL lifetime was reduced, while the emission was still confined to the direction perpendicular to the substrate. This demonstrated directional control and enhancement of the PL emission.

Kongsuwan *et al.*[20] demonstrated how Rabi splitting could be utilised for quantum sensing. In this system, two antibodies were used to bind an antigen to a quantum emitter. This was placed in the electric field hot-spot in the centre of a dimer, resulting in Rabi splitting. Several simulations were carried out with the antigens bonded to the quantum dots randomly scattered about the dimers. It was shown that the quantum case (with at least one antigen bonded to an emitter in the middle of the dimer) gave a much more powerful shift than the classical case (without any antigen bonded to an emitter in the middle of the dimer) even with a higher density. This study shows how Rabi splitting can be used as a reliable method of detecting an analyte in an immunoassay.

A photon blockade can be achieved with Rabi splitting with a single quantum dot or atom coupled to a cavity[114]. This can be shown with the Jaynes-Cummings ladder, with the Rabi splitting energy shift changing the energy levels of the system. When a photon is absorbed by this system, the absorbance of another photon is blocked until the original photon is emitted, resulting in anti-bunching. An unconventional photon blockade is also possible by engineering the quantum interference between different excitation pathways resulting in bunched pairs of photons interfering destructively, but single photons and photons in bunches of three or more being emitted. You *et al.*[115] demonstrated how a system could be switched between a conventional and unconventional photon blockade by placing emitters at the corners of a metal nanoprism. If the excitation light was polarised, the coupling strengths of the emitters at each of the corners could be tuned. This allowed for the system to be easily switched between the photon blockade and unconventional photon blockade with just changing the polarisation of the incident light.

Rabi splitting is also important for quantum entanglement, which is an essential part of quantum information processing. Xiong *et al.*[23] demonstrated how quantum entanglement between two quantum dots at the opposite upper corners of a Au nanocube coupled to a Au film. This study showed that the entanglement was stronger when the emission of the quantum dots were slightly detuned from the antenna mode of the nanocube-on-mirror system, and when the coupling strength was higher. It was demonstrated that the coupling strength could be increased by coating an entire nanocube with more layers of quantum emitters before depositing on the Au film. The system was brought into the ultrastrong coupling regime, where the coupling strength is comparable in energy to the energy of the plasmonic resonances. This study demonstrated quantum entanglement on a single nanocube, but has the potential to be scaled up to a larger quantum network. The development of such a structure would be a major stepping stone towards the development of a quantum computer. This would have the potential to revolutionise many branches of science by performing calculations much faster that today's supercomputers, allowing for much more accurate simulations.

2.5 Conclusion

In this chapter, the background to the experimental chapters of this thesis is presented. In chapter 4, graphene is used as a 2D material, and in chapters 5 and 6 MoS_2 is used. For both materials, the two-dimensional nature is demonstrated with diagrams showing the relative positions of the atoms. Further, the nature of the electric band structures is also shown, which will aid in the elucidation of how they can be used and manipulated when being coupled to the plasmonic and dielectric structures discussed in later chapters.

The theory behind plasmon oscillations was introduced, giving some background to the work demonstrated in chapters 4 and 5. An introduction to dielectric nanoparticles was also introduced as a background for the work in chapter 6. Background theory and applications were given for both the strong and weak coupling effects, which will be demonstrated in chapters 5 and 6, respectively.

> We have all a better guide in ourselves, if we would attend to it, than any other person can be.
>
> ---
>
> Jane Austen

3 Methods

3.1 Computational Techniques

3.1.1 Finite-Difference Time-Domain Simulations

The Finite-Difference Time-Domain (FDTD) technique was used to carry out numerical simulations with the commercial software, Lumerical solutions. This is a state-of-the-art method for solving Maxwell's equations for complex nanophotonic structures for non-magnetic materials. A Computer Aided Design (CAD) tool is used to visualise the structures being simulated, with a three-dimensional, Cartesian-style mesh defined over the simulation volume. At each mesh point, the material properties are defined, with each point containing the frequency-dependent complex refractive index information of the material defined to be in the specific location. The electric and magnetic fields are also measured for each mesh point in the simulation. Several different types of sources are supported with the Lumerical FDTD solver including a dipole source, a plane wave and a total-field-scattered-field (TFSF) source. The boundary conditions of a simulation can be defined in several ways, including periodic boundary conditions which are useful for simulating an array of nanoparticles, and perfectly matched layer (PML) boundary conditions which are designed to absorb light and reduce back-reflections. The simulation is programmed to end when the electric field reaches a steady state, falling below a set threshold value, or when the simulation reaches a set time.

The E and H fields at each mesh point are calculated using Maxwell's curl equations:

$$\frac{\partial \overrightarrow{D}}{\partial t} = \nabla \times \overrightarrow{H} \tag{3.1}$$

$$\overrightarrow{D}(\omega) = \varepsilon_0 \varepsilon_r(\omega) \overrightarrow{E}(\omega) \tag{3.2}$$

$$\frac{\partial \overrightarrow{H}}{\partial t} = -\frac{1}{\mu_0} \nabla \times \overrightarrow{E} \tag{3.3}$$

where D, H and E are the displacement, magnetic and electric fields, respectively, $\varepsilon_r(\omega)$ is the complex relative dielectric constant and ε_0 and μ_0 are the permittivity and permeability of free space, respectively.

Each point in the mesh corresponds to a Yee cell, as shown in figure 3.1. The electric field and magnetic field components, E_x, E_y, E_z, H_x, H_y and H_z are measured in different parts of the Yee cell.

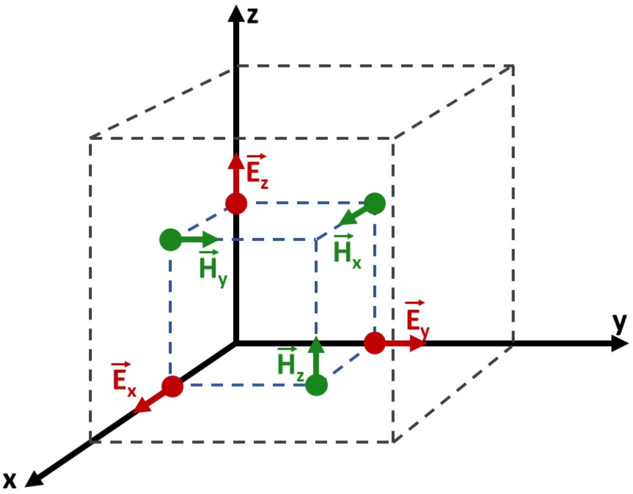

Figure 3.1: A Yee cell, showing where each component of the electric and magnetic fields are solved relative to each other within the grid cell of the mesh.

The curl of $\overrightarrow{E}$ and $\overrightarrow{H}$ are calculated in a leapfrog algorithm[116], with $\overrightarrow{E}$ being measured at times $t, t+\Delta t, t+2\Delta t, ...$ and $\overrightarrow{H}$ being measured at times $t+\frac{1}{2}\Delta t, t+\frac{3}{2}\Delta t, t+\frac{5}{2}\Delta t, ...$, with Δt being the time interval between iterations. Therefore,

$$\overrightarrow{E}^{t+\Delta t} = \overrightarrow{E}^{t} + \alpha(\nabla \times \overrightarrow{H}^{t+\frac{1}{2}\Delta t}) \tag{3.4}$$

$$\overrightarrow{H}^{t+\frac{3}{2}\Delta t} = \overrightarrow{H}^{t+\frac{1}{2}\Delta t} + \beta(\nabla \times \overrightarrow{E}^{t+\Delta t}) \tag{3.5}$$

where α and β are proportionality terms, dependent on the simulation parameters.

The derivative of the electric field as shown in equations 3.1 and 3.2 is found by the curl of the $\overrightarrow{H}$ field and can be written as:

$$\frac{\partial H_z}{\partial y} - \frac{\partial H_y}{\partial z} = \varepsilon_0 \varepsilon_r \frac{\partial E_x}{\partial t} \tag{3.6}$$

$$\frac{\partial H_x}{\partial z} - \frac{\partial H_z}{\partial x} = \varepsilon_0 \varepsilon_r \frac{\partial E_y}{\partial t} \tag{3.7}$$

$$\frac{\partial H_y}{\partial x} - \frac{\partial H_x}{\partial y} = \varepsilon_0 \varepsilon_r \frac{\partial E_z}{\partial t} \tag{3.8}$$

Similarly, the derivative of the magnetic field as shown in equation 3.3 can be written with the partial differentials of $\overrightarrow{E}$ as:

$$\frac{\partial E_z}{\partial y} - \frac{\partial E_y}{\partial z} = -\mu_0 \frac{\partial H_x}{\partial t} \tag{3.9}$$

$$\frac{\partial E_x}{\partial z} - \frac{\partial E_z}{\partial x} = -\mu_0 \frac{\partial H_y}{\partial t} \tag{3.10}$$

$$\frac{\partial E_y}{\partial x} - \frac{\partial E_x}{\partial y} = -\mu_0 \frac{\partial H_z}{\partial t} \tag{3.11}$$

Where the initial filed conditions and the material properties are known, FDTD can solve the above equations with the discrete Yee cells and time intervals of Δt.

The derivative of any arbitrary function $f(x)$ is described as:

$$f'(x) = \lim_{\Delta x \to 0} \frac{f(x+\Delta x) - f(x)}{\Delta x} \tag{3.12}$$

Δx cannot be zero for numerical calculations, so an approximation using very small values must be used for FDTD simulations. A higher accuracy simulation would have smaller Yee cells and shorter Δt time intervals, but at a cost of a much higher simulation time. The derivative of the function is approximated as:

$$f'(x) \approx \frac{f(x+\Delta x) - f(x)}{\Delta x} \tag{3.13}$$

For a small Δx, a more accurate estimation for a tangent to $f(x)$ than the one-sided approximation is given by the central difference method:

$$f'(x) \approx \frac{f(x+\Delta x) - f(x-\Delta x)}{\Delta x} \tag{3.14}$$

This technique is employed by FDTD, with the electric and magnetic field being measured at alternating times and positions in the Yee cell, as discussed above.

From equation 3.3, The H field can be calculated with the curl of $\overrightarrow{E}$. For numerical simulations, this is written as:

$$\frac{E_z^{i,(j+1),k}|_t - E_z^{i,j,k}|_t}{\Delta y} - \frac{E_y^{i,j,(k+1)}|_t - E_y^{i,j,k}|_t}{\Delta z} = -\mu_0 \frac{H_x^{i,j,k}|_{t+\frac{1}{2}\Delta t} - H_x^{i,j,k}|_{t-\frac{1}{2}\Delta t}}{\Delta t} \tag{3.15}$$

This is illustrated in a Yee cell in figure 3.2a, showing how $E_z^{i,j,k}$, $E_z^{i,(j+1),k}$, $E_y^{i,j,k}$ and $E_y^{i,j,(k+1)}$ are needed to calculate the curl of $H_x^{i,j,k}$.

Similarly, the E field can be calculated with the curl of $\overrightarrow{H}$ from equation 3.1. For numerical simulations, this is written as:

$$\frac{H_z^{i,j,k}|_{t+\frac{1}{2}\Delta t} - H_z^{i,(j-1),k}|_{t+\frac{1}{2}\Delta t}}{\Delta y} - \frac{H_y^{i,j,k}|_{t+\frac{1}{2}\Delta t} - H_y^{i,j,(k-1)}|_{t+\frac{1}{2}\Delta t}}{\Delta z} = \varepsilon_0 \varepsilon_r \frac{E_x^{i,j,k}|_{t+\Delta t} - E_x^{i,j,k}|_t}{\Delta t} \tag{3.16}$$

This is illustrated in a Yee cell in figure 3.2b, showing how $H_z^{i,j,k}$, $H_z^{i,(j-1),k}$, $H_y^{i,j,k}$ and $H_y^{i,j,(k-1)}$ are needed to calculate the curl of $E_x^{i,j,k}$. $E_y^{i,j,k}$, $E_y^{i,j,k}$, $H_y^{i,j,k}$ and $H_z^{i,j,k}$ can be calculated analogously.

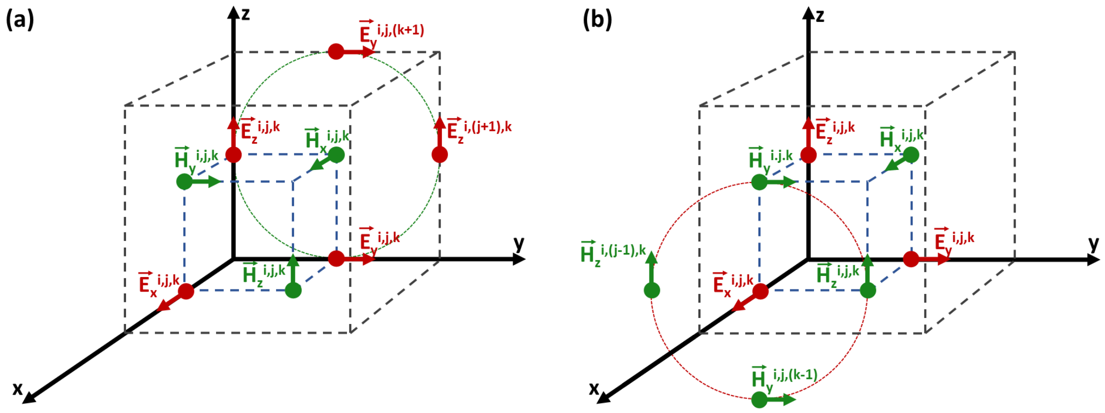

Figure 3.2: (a) A Yee cell, illustrating that $E_z^{i,j,k}$, $E_z^{i,(j+1),k}$, $E_y^{i,j,k}$ and $E_y^{i,j,(k+1)}$ are used to calculate $\nabla H_x^{i,j,k}$. (b) A Yee cell, illustrating that $H_z^{i,j,k}$, $H_z^{i,(j-1),k}$, $H_y^{i,j,k}$ and $H_y^{i,j,(k-1)}$ are used to calculate $\nabla E_x^{i,j,k}$.

FDTD is solved in the time domain. The source signal ($s(t)$) would ideally be a dirac delta function, allowing all solutions in the frequency domain, $s(\omega)$, be equal to one. $s(\omega)$ is the Fourier transform of $s(t)$, and is found by:

$$s(\omega) = \int e^{i\omega t} s(t)dt \tag{3.17}$$

With FDTD simulations, it is more accurate and efficient to model the signal as a short pulse with a reasonably large value of $s(\omega)$ over the frequency range of interest.

The simulated electric field can be found by:

$$\overrightarrow{E}_{sim}(\omega) = \int e^{i\omega t} \overrightarrow{E}(t)dt \tag{3.18}$$

The result of $\overrightarrow{E}_{sim}(\omega)$ depends on the system being studied, as well as the source pulse. Therefore, continuous wave normalisation is used, so that the impulse response of the system only is returned:

$$\overrightarrow{E}(\omega) = \frac{\overrightarrow{E}_{sim}(\omega)}{s(\omega)} \tag{3.19}$$

$\overrightarrow{H}(\omega)$ is also normalised in the same way:

$$\overrightarrow{H}(\omega) = \frac{1}{s(\omega)} \int e^{i\omega t} \overrightarrow{H}(t)dt = \frac{\overrightarrow{H}_{sim}(\omega)}{s(\omega)} \tag{3.20}$$

The Poynting vector is found by the cross product of the E and H fields, and indicates the energy flux of the electromagnetic wave. It is also normalised by the continuous wave normalisation:

$$\overrightarrow{P}(\omega) = \frac{\overrightarrow{E}_{sim}(\omega) \times \overrightarrow{H}^*_{sim}(\omega)}{|s(\omega)|^2} = \overrightarrow{E}(\omega) \times \overrightarrow{H}^*(\omega) \tag{3.21}$$

For FDTD simulations, the accuracy is improved with smaller mesh sizes, at the cost of longer simulation times. A particular challenge is met when simulating 2D materials due to their sub-nanometer dimensionality. In this work, to keep simulation times down, the mesh size was reduced only in the region around the 2D materials, along the axis of their smallest dimension. Convergence tests were employed with several different mesh sizes to ensure the numerically simulated results converged to accurate values.

3.2 Synthesis and Characterisation of Au Nanoparticles

3.2.1 Spheres

Many studies reporting the growth of Au nanospheres give non-uniform, poly-crystalline and quasi-spherical shapes. Zheng *et al.*[117] reported a method for the growth of Au spheres which resulted in single-crystalline spheres with precisely controlled diameters in the range of 5-150 nm. This method involves several steps, beginning with the growth of CTAB-capped Au clusters which were used as seeds for the growth of 5-16 nm spheres. The 10 nm spheres were then used as seeds for the growth of 15-80 nm spheres, and the 46 nm spheres were used as seeds for the growth of 70-150 nm spheres. The single-crystalline structure and the spherical shape are kept by the slow addition of $HAuCl_4$ into the growth solutions. Spheres of a variety of sizes grown by this method are shown in figure 3.3.

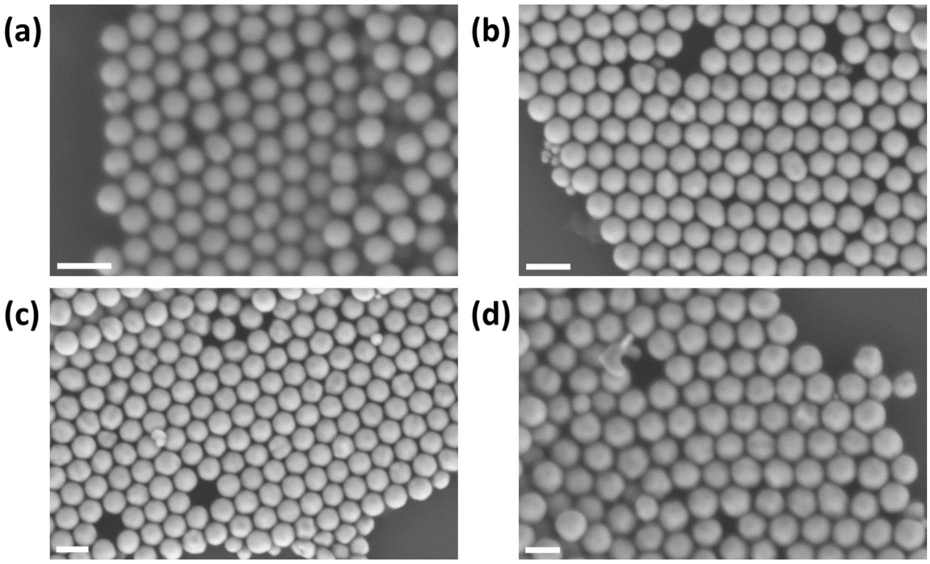

Figure 3.3: SEM images of a variety of nanospheres synthesised for this work. The diameters of the spheres shown are 105, 120, 145 and 180 nm for figures (a), (b), (c) and (d), respectively. All white scale bars show 200 nm.

To make the Au clusters, 0.6 mL of 10 mM $NaBH_4$ was added to a 10 mL aqueous solution 2.5 mM $HAuCl_4$ and 0.1 M CTAB, immediately forming a brown solution. This was stirred rigorously for two minutes before being kept undisturbed for three hours at 27°C.

To make the 10 nm spheres, 2 mL of 0.2 M cetyltrimethylammonium chloride (CTAC), 1.5 mL of 0.1 M ascorbic acid and 50 μL of the Au cluster solution were mixed together, followed by 2 mL of 0.5 mM $HAuCl_4$. This reaction was left to continue for 15 minutes at 27°C. The product was then collected by centrifugation, and washed with water once before being diluted again in 1 mL of 20 mM CTAC solution.

To make the 46 nm spheres, 2 mL of 0.1 M CTAC, 130 μL of 10 mM ascorbic acid and 10 μL of the 10 nm Au sphere solution were mixed together. This was followed by the addition of 2 mL of 0.5 mM $HAuCl_4$, slowly added with 80 μL being added every 2.5 minutes over an hour. This reaction was left to continue for 10 minutes at 27°C after the addition of the last dose of $HAuCl_4$. The product was then collected by centrifugation, and washed with water once before being diluted again in 0.86 mL of millipore water.

To make the larger spheres used in this work and shown in figure 3.3, 2 mL of 0.1 M CTAC, 130 μL of 10 mM ascorbic acid and the 46 nm Au sphere solution were mixed together. Four samples were grown, with 50, 100, 200 or 300 μL of the 46 nm Au sphere solution being added to each separate one. This was followed by the addition of 2 mL of 0.5 mM $HAuCl_4$, slowly added with 80 μL being added every 2.5 minutes over an hour. This reaction was left to continue for 10 minutes at 27°C after the addition of the last dose of $HAuCl_4$. The product was then collected by centrifugation, and washed with water once. The spheres grown at the end of this step were 180, 145, 120 and 105 nm in diameter for the samples with 50, 100, 200 and 300 μL of the 46 nm Au sphere solution added, respectively.

As can be seen from these results, the size of the nanospheres can be precisely controlled by the amount of seeds added to the growth solution. If many seeds are added, the Au precursor has to divide itself between all of the seeds present, resulting in smaller spheres. If fewer seeds are added, there is a larger amount of Au precursor added per seed, resulting in larger spheres.

The rate of the addition of the Au precursor to the growth solution was crucial for obtaining spherical nanoparticles. If the precursor was added too quickly, in one shot, the surface diffusion effect would be neglected. This means that the facets of the sphere would be less likely to be the most energetically favourable because a Au atom is more likely to deposit along a (111) direction. This effect would result in the surface mainly being covered in (100) facets, leading to cube-like nanoparticles. Conversely, if the precursor was added too slowly, for example 1 mL per hour, surface diffusion would cause the facets to be in the more energetically favourable state. The Au atoms would have sufficient time to move to the (100) facets, reducing the proportion of (100) facets in the final product. This would cause the spheres to become more like truncated octahedrons in shape. Therefore, a specific rate for adding the Au precursor is needed to ensure the correct balance of (111) and (100) facets to make a Au nanosphere.

The ascorbic acid was added into the growth solution to reduce the Au(III) to Au(II). If the concentration of the ascorbic acid was too low, less Au would be reduced and be able to adsorb onto the nannosphere surfaces. A very high concentration, however, would increase the reduction rate, thus making the growth too fast. This would cause the nanospheres to become less spherical in shape.

CTAC was used instead of CTAB for the growth of the nanospheres from the Au clusters and from the Au seeds because the presence of Br^- ions in the growth solution resulted in nanoparticles with a cuboctahedral shape. This is due to the Br^- ions selectivley adsorbing onto the (110) facets. Smaller and more electronegative hallides have a weaker binding affinity with Au[118], making the Cl^- ions in CTAC a better option for the growth of Au nanospheres. The CTAC in the growth solution prevented aggregates of nanoparticles forming, and also prevented the growth only along selected facets which would have occurred with the use of CTAB.

3.2.2 Bipyramids

Au nano-bipyramids have sharp and easily tunable plasmonic resonances. Bipyramids have a very large near-field enhancement at their two tips which compares favourably with other similar nanoparticle shapes such as rods. The Au bipyramids used in this work were synthesised with a wet chemistry approach, grown from Au penta-twinned seeds[119]. The bipyramids synthesised in this work were easily tuneable, made with a variety of shapes and sizes with a high yield as shown in figure 3.4.

The penta-twinned seeds are grown using the procedure of Jana *et al.*[120]. 5 mL of 0.25 mM sodium citrate was added to 2.5 mL of 0.25 mM $HAuCl_4$ and 2.5 mM millipore H_2O, with rigorous stirring. 0.15 mL of 10 mM $NaBH_4$ was added, and this solution was aged for 2 hours. All steps were carried out at room temperature.

To grow the Au bipyramids with the procedure of Liu *et al.*[119], 0.5 mL of 10 mM $HAuCl_4$ and 0.1 mL of 10 mM $AgNO_3$ were added to 10 mL of a 0.1 M CTAB (Cetyltrimethy-

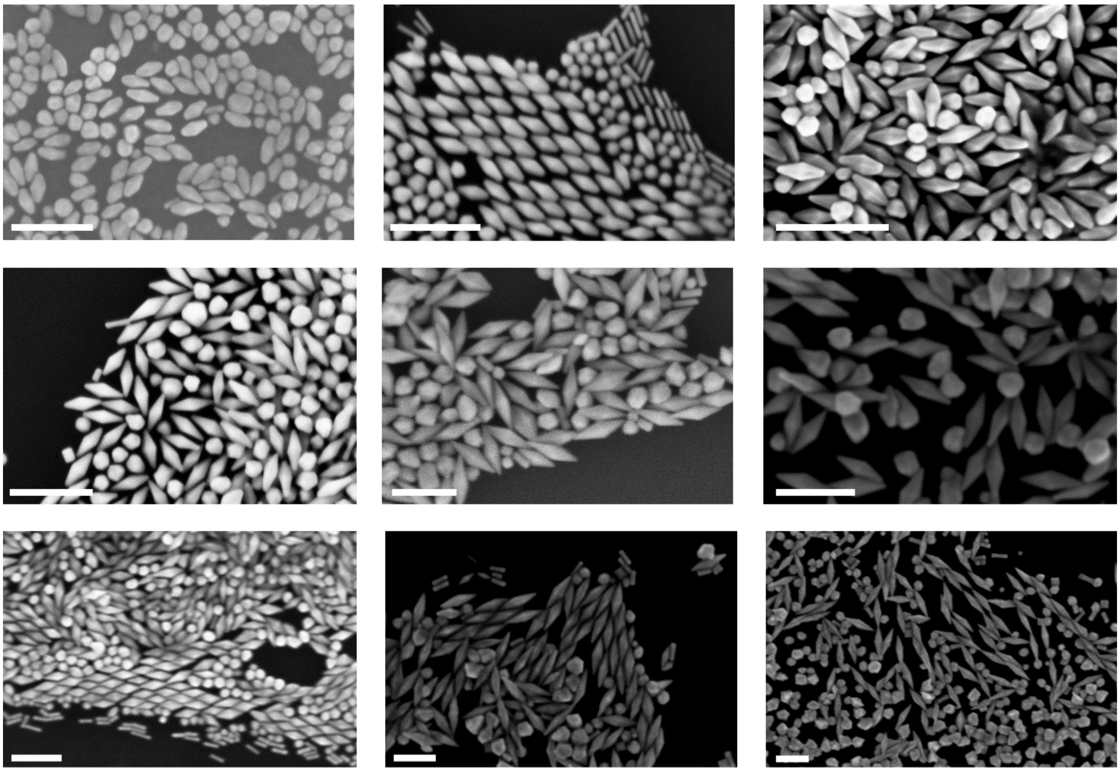

Figure 3.4: SEM images of a variety of bipyramids synthesised for this work. All white scale bars show 200 nm.

---

lammonium bromide) solution. This was acidified with 0.2 mL of 1 M HCl to a pH of approximately 3 or 4. 0.08 mL of 0.1 M l-ascorbic acid was added to reduce the Au(III) to Au(I), followed by 80 μL of the aged Au seed solution. This growth reaction was carried out in a 30° water bath for two hours.

The mechanism for growing the seeds into bipyramids relies heavily on the Ag(I) in the solution. With the Ag(I) present when growing from a single crystalline seed, the fully grown nanoparticle retains the single crystalline structure. Similarly, when penta-twinned seeds are used, as in this case, the fully grown nanoparticle will also have a penta-twinned structure. This is because the Ag(I) significantly increases the growth time of the nanoparticles, and therefore allows the Au atoms to adsorb to the most energetically favourable place. This ensures that the atoms are packed in the face-centred cubic (FCC) geometry, with no new twin defects introduced that were not already present in the seeds.

With the presence of the Ag(I) in the growth solution, the surface structures of the nanoparticles become energetically unfavourable. When rods are grown from single-crystalline seeds, they have facets with the surface structure (110). The (110) facet rarely appears on the surface of Au nanocrystals, as (111) and (100) facets are much more energetically favourable.

Bipyramids have stepped surfaces, making their facets (11n), further increasing the surface energy. This unusual effect is due to the underpotential deposition of Ag atoms onto the surface of the Au nanocrystals.

For bulk Ag(0) deposition, a basic pH is needed. However, when only a monolayer or sub-monolayer of Ag is being deposited on a different metal, the work function is much lower, resulting in underpotential deposition. This allows Ag atoms to be absorbed onto the surface of a Au structure, even in an acidic solution. Underpotential deposition favours more open surface structures for the adatom to adsorb onto. This is because with a more open facet structure, the adatom has more nearest neighbours to bond to. This is illustrated in figure 3.5. The (111) facet is the most energetically favourable, but the Ag adatom only has three nearest neighbours. The (100) facet is less energetically favourable, but the Ag adatom has four nearest neighbours, making it more stabilised with the Ag(0) present. The most open and energetically unfavourable structure shown here is the (110) facet, which gives an adsorbed adatom five nearest neighbours, further increasing the stabilisation from the Ag(0).

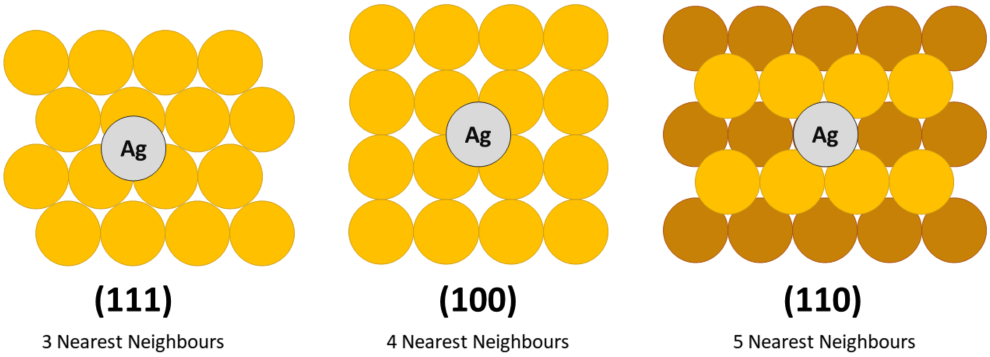

Figure 3.5: Geometry of Ag atom adsorbed onto 3 types of FCC facet during the bipyramid growth process.

During the growth of the Au bipyramids, the Br^- from the CTAB selectively adsorbs onto the (110) facets. Therefore, the growth only occurs perpendicular to these facets, which is along the twinning axis. The side-wall cannot always be flat during this growth, so it will naturally form a stepped facet of (11n). Without any Ag(I) in the solution, these steps are not thermodynamically stable, so they will disappear, resulting in a nanorod structure at the end of the growth. With the Ag(I) present in the solution, the steps are stabilised, resulting in ten-sided bipyramid shapes at the end of the growth process.

The underpotential deposition of Ag(0) onto the Au surface essentially reverses what facets are more thermodynamically favourable for a Au crystalline structure. Therefore, the growth solution can be manipulated to give a high degree of control over the size and aspect ratios (ratio of length to width) of the bipyramids grown in the solution.

Bipyramids of different lengths, aspect ratios and tip radii were synthesised by varying the concentrations of the different chemicals required. These features have an effect on the UV-vis spectrum of the bipyramid sample. (UV-vis measurements will be discussed in section 3.12.) A longer bipyramid or a higher aspect ratio has a red-shifted plasmonic resonance, while a shorter bipyramid or a lower aspect has a blue-shifted plasmonic resonance. The tip radii of the bipyramids were also seen to have an effect, blue-shifting the plasmonic resonance when they were increased.

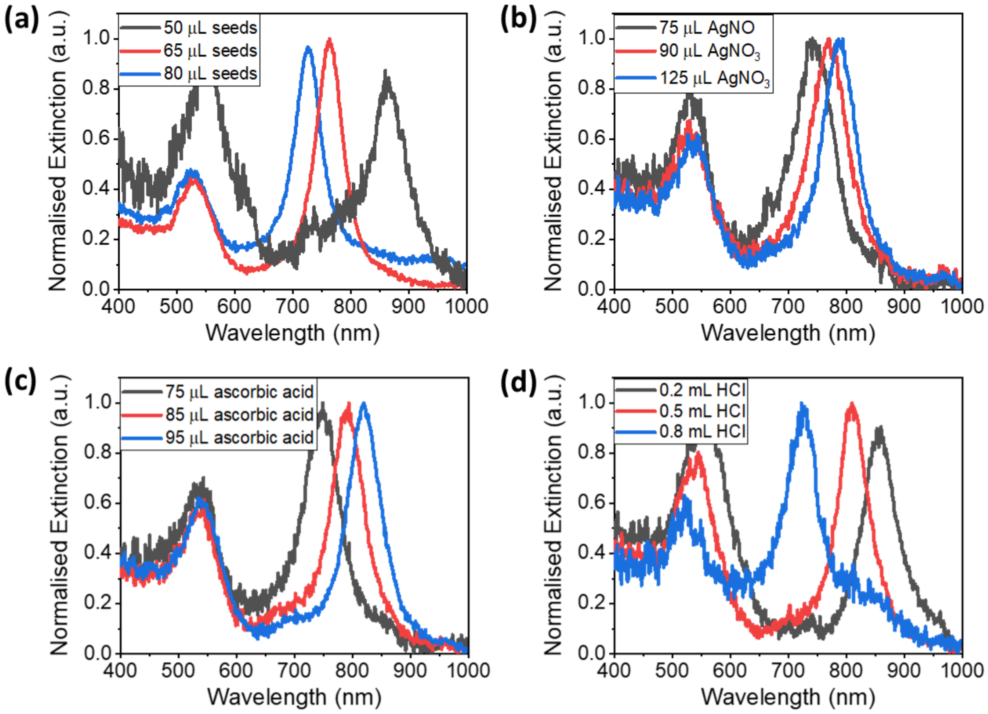

Figure 3.6: UV-vis extinction spectra for various bipyramid samples in solution. Plots a, b, c and d show samples of varying concentrations of Au penta-twinned seeds, silver nitrate solution, ascorbic acid solution and hydrochloric acid, respectively.

The UV-vis spectra of various bipyramid samples in aqueous solutions are shown in figure 3.6. Figure 3.6a shows the effect of changing the seed concentration added to the growth solution. As was expected, it was found that a lower amount of seeds added to the solution resulted in fewer, larger bipyramids. More seeds added resulted in smaller bipyramids. The aspect ratio of each of the bipyramids remained fixed as the other chemicals dictated the slope of the sides. The plasmon shift visible was therefore due to the overall size of the bipyramids in the batch. The smaller bipyramids had a blue-shifted plasmonic peak with respect to the larger bipyramids.

Figure 3.6b shows the effect of varying the Ag concentration. Less Ag added to the growth solution has the effect of less Ag adatoms adsorbing to the surface of the synthesising bipyramids. Therefore, the growth is less stunted in the width-wise direction. This gives wider bipyramids with more steps along the bipyramid facets, resulting in a lower aspect ratio. If too little $AgNO_3$ is added, there is no preferential growth direction, causing nanostars to form. Nanostars were seen to form with the addition of less than 75 μL of 10 mM $AgNO_3$. The change in the plasmonic resonance with varying Ag concentrations is due to the aspect ratio difference.

Figure 3.6c shows the effect of changing the concentration of ascorbic acid in the solution. The ascorbic acid was shown to have an effect on the overall size of the bipyramid, giving larger bipyramids when more of is was added to the growth solution. This is because the ascorbic acid in the solution reduced the Au(III) to Au(I). Therefore, less ascorbic acid in the solution would result in less Au(I) being available to adsorb onto the growth surface.

Figure 3.6d shows the effect of changing the concentration of hydrochloric acid on a batch of bipyramids. The HCl has several effects on the bipyramid growth. It was observed that the presence of extra HCl in the solution slowed the reduction of Au(III) to Au(I) when the ascorbic acid was added. Therefore, a higher concentration of HCl in the solution reduced the overall size of the synthesised bipyramids. This blue-shifted the plasmonic resonance with the addition of more HCl. The other effect of the HCl was the change in underpotential deposition. With a basic pH, bulk Ag can adsorb onto the surface. When the pH was too high (with no addition of HCl into the growth solution), stars were formed, showing no dominant growth direction.

The Au concentration also had to be precisely controlled. Too much Au in the solution resulted in Au piling on at the end of the tips. This severely reduced the sharpness of the tips and thus the electric field enhancement was also reduced. Too much Au also lessened the proportion reduced to Au(I) by the ascorbic acid. Too little Au, however, would result in very small bipyramids. The Au was particularly important to control due to the importance of the sharp tips, providing a large electric field enhancement.

The uniform nature of the sizes and shapes of the bipyramids is apparent from the SEM images in figure 3.4 as well as the sharp UV-vis peaks in figure 3.6. This uniformity is important to give the opportunity of comparing large samples of similar bipyramids more accurately. However, there is always some variation between chemically synthesised particles. The small degree of change from particle to particle within the sample is also important to investigate how smaller changes within a plasmon can affect a plasmonic system.

3.3 Growth of 2D Materials

3.3.1 Graphene

Copper can be used for $> 90\%$ coverage of monolayer graphene grown by CVD[33]. It works well as a catalyst for graphene growth compared to other transition metals due to its filled 3d electron shell. It can therefore only form soft bonds with carbon, with charge transfer from the electrons in the sp^2 hybridised bonds of the carbon to the 4s state of the copper. This effect serves to stabilise the carbon with weak bonds to the copper surface, without the copper and carbon chemically reacting.

The graphene was grown on a 25 μm thick sheet of copper foil. The foil was heated to 1094°C in a Carbolite tube furnace under 50 standard cubic centimeters per minute (sccm) of H_2. This was left to dwell for 60 minutes to anneal the Cu, removing any oxides, reducing defects and increasing the Cu grain size. CH_4 was introduced at 10 sccm, with the H_2 flow being reduced to 6 sccm. This lead to uniform nucleation of graphene islands, with orientations dependent on the below orientations of the Cu grains. Over the growth time period, these islands increased in size and eventually coalesced, forming a single monolayer of graphene over the entire copper surface. This growth step was carried out for 30 minutes. The CH_4 flow was then switched off while the H_2 flow was reduced to 3 sccm while the samples cooled to room temperature.

After the growth, the graphene was transferred onto the desired substrates[121]. A2 950K PMMA was spun onto the graphene and copper samples at 3000 revolutions per minute (rpm) for 60 seconds, then 1000 rpm for 60 seconds after washing them in acetone and IPA. The samples were then baked for 5 minutes at 120°C. The samples were cut to the desired size before backside etching in a 20g per 100 mL solution of ammonium persulfate (APS). The samples were repeatedly submerged in water and placed back on top of the APS solution for the first 7 minutes of this process to remove any graphene on the backside of the copper foil. The samples were then left for about an hour on top of the APS solution, until all the copper was etched away. The PMMA supported graphene was then fished into millipore water, before being fished onto the desired substrate. The samples were then placed in a desiccator overnight, before being heated to 150°C for five minutes, being immersed in acetone for 20 minutes and finally being rinsed with IPA and blow dried with a nitrogen gun.[1]

---

[1] Some of the graphene used in this work was grown by Joshua Pepper and Niall McEvoy.

3.3.2 MoS_2

MoS_2 has been widely investigated and characterised with chemical vapour deposition, making it possible to obtain high-quality monolayer flakes[122]. Chemical vapour deposition (CVD) was chosen as the fabrication technique. This was because it results in a large area coverage of monolayer MoS_2 and high crystallinity in comparison with other methods[123].

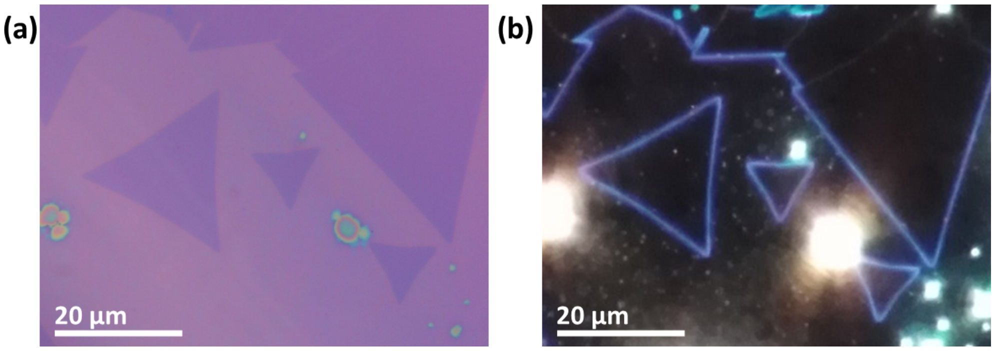

Figure 3.7: (a) Bright field and (b) dark field microscopy image of monolayer MoS_2 flakes grown by chemical vapour deposition.

For the CVD growth of MoS_2, a target substrate was placed face-down on a seed substrate. These were both 300 nm SiO_2 on Si substrates. The seed substrate had liquid-phase exfoliated MoO_3 nanosheets drop-cast onto it. This was then placed in the centre of a quartz tube furnace. It was heated to 750 °C under 150 standard cubic centimeters per minute (sccm) Ar flow at a pressure of about 0.7 Torr. Sulfur vapour was generated in a separate downstream part of the furnace by heating sulfur powder to 120 °C. The seed and target substrates were exposed to the sulfur vapour, with forming gas as a carrier. This reduces the MoO_3 to MoO_2, before the MoO_2 reacts with the S to form MoS_2[124]. Bright field and dark field microscopy images of typical monolayer MoS_2 CVD flakes are shown in figure 3.7.

To transfer the MoS_2 onto a different substrate, a polymer support technique was used[125]. Polymethyl methacrylate (PMMA) was spin-coated onto the MoS_2 sample on the SiO_2/Si substrate it was grown on, then heated to 150°C for 5 minutes. The MoS_2/PMMA films were removed from the growth substrate by floating in 2M NaOH at 80°C. These were transferred to deionised water for cleaning, before being fished onto the desired substrates. These were left to dry in a desiccator overnight. The PMMA layer was then dissolved by immersion in acetone for 20 minutes, rinsed with IPA and again placed in a desiccator to dry.[2]

---

[2] All of the MoS_2 used in this work was grown and transferred by Lisanne Peters and Niall McEvoy.

3.4 Raman and Photoluminescence Spectroscopy

Raman spectroscopy is a technique based on the inelastic scattering of monochromatic light from a material. The scattered light is of a lower energy than the incident light. This is because some of the energy is absorbed to excite the molecules to a higher energy vibration or rotational level. This inelastic scattering process is significantly less likely to occur than elastic scattering, with only 1 in every 10^7 photons being scattered inelastically. Therefore, to obtain a good quality Raman spectrum, a high intensity of incident laser light and high integration times are required. Raman spectra are described by wavenumber ($\tilde{v}$) in cm^{-1} units, and are found by

$$\tilde{v} = \frac{1}{\lambda_0} - \frac{1}{\lambda_1} \tag{3.22}$$

where λ_0 is the wavelength of the incident monochromatic laser and λ_1 is the wavelength of the scattered light. Raman spectroscopy demonstrates individual blueprint spectrum for each material, and is widely used for characterisation.

The Raman spectra for chapter 5 were taken with a Horiba Jobin Yvon Raman spectrometer with a 100x objective lens of numerical aperture 0.9. A 532 nm laser was used. The Raman spectra for chapters 4 and 6 were taken with a WITec Alpha 300R with a 633 nm and a 532 nm excitation laser, respectively. A 100x objective lens of numerical aperture 0.9 was used for taking single spectra, and a 50x objective lens of numerical aperture 0.75 was used for taking maps.

Photoluminescence (PL) spectroscopy is another optical technique that can be used to characterise materials. It is the process by which a material absorbs an incident photon before emitting another photon, usually of lower energy. This technique was used in chapters 5 and 6 to characterise the MoS_2 used and to probe the energy of the A exciton, by measuring the emitted light.

The PL spectra were taken with an Olympus upright microscope with a 100x objective lens of numerical aperture 0.9. Both 405 nm and a 532 nm lasers were used.

3.4.1 Graphene

The graphene was confirmed to be monolayer by Raman spectroscopy (see figure 3.8). The strong peak at 1588 cm^{-1} is the G mode, which is the E_{2g} mode, caused by the carbon atoms vibrating in the graphene plane.

The 2D peak, at 2647 cm^{-1}, is the most prominent, and is due to a double resonance process. The position and FWHM of the 2D peak confirms that the graphene is a monolayer[27,

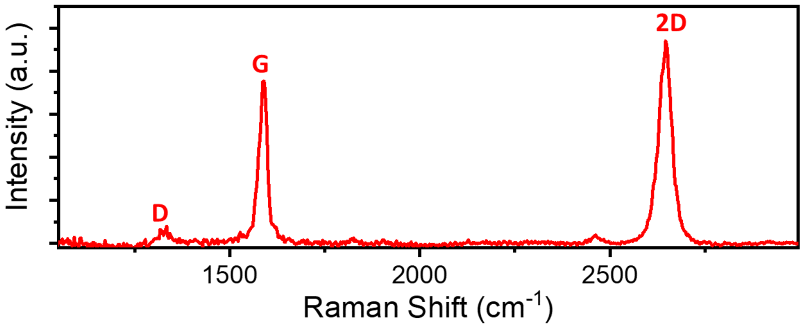

Figure 3.8: Raman spectrum of monolayer graphene on SiO_2/Si surface grown by CVD on Cu film.

126]. For bilayer graphene, the 2D band significantly broadens and red-shifts, the FWHM increasing from 35 cm^{-1} (as shown in figure 3.8) to 50 cm^{-1} and it peak upshifting by 20 cm^{-1}. This is because the single 2D Raman peak of monolayer graphene splits into four components in the bilayer case. This change in bilayer graphene is due to the change in the electronic band structure with the number of graphene layers. The monolayer case is shown in figure 3.9a. The laser with energy ε_L induces the excitation of an electron-hole pair (a $\rightarrow$ b). Electron-phonon scattering close to **K** occurs at exchanged momentum **q** (b $\rightarrow$ c), and then again at **-q** (c $\rightarrow$ b), before the electron-hole recombination (b $\rightarrow$ a). Therefore, the 2D Raman frequency is two times the scattering frequency. It is also clear from figure 3.9 that the Raman shift of the 2D peak is largely dependent on the laser frequency used, a higher frequency resulting in a higher energy 2D peak.

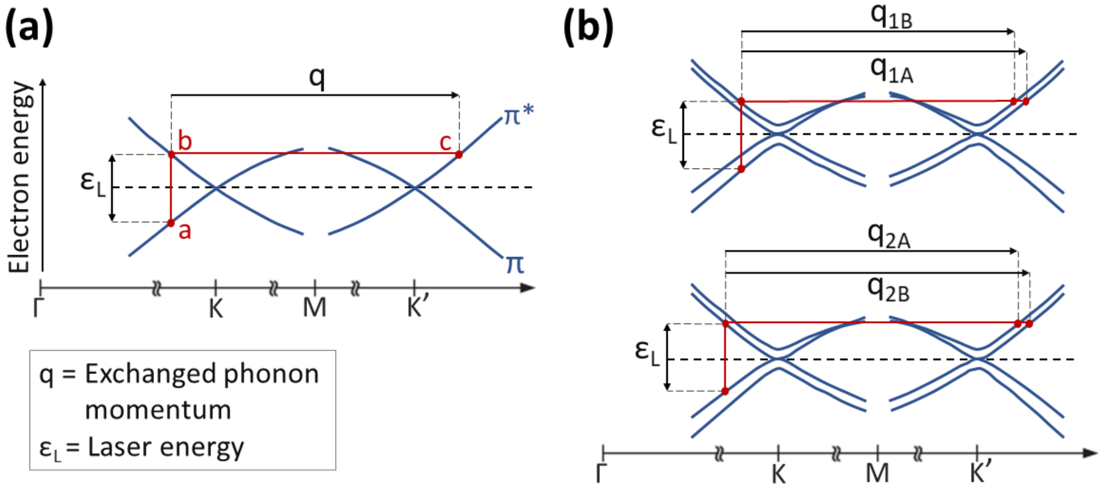

Figure 3.9: The origins of the 2D peak in the Raman spectrum for monolayer and bilayer graphene. This diagram representing the simplified electronic band structure of graphene was modified from Ferrari *et al.*[126]. The black dashed line shows the Fermi energy in each plot.

In the bilayer case, the interactions between the two graphene sheets cause the π and $\pi*$ bands to split into four different bands figure 3.9b. The four resulting Raman shifts are associated with the momenta $\mathbf{q_{1B}}$, $\mathbf{q_{1A}}$, $\mathbf{q_{2A}}$ and $\mathbf{q_{2B}}$. These four peaks are close together and appear as a much broader peak, and at a higher Raman shift than the equivalent 2D peak in the monolayer case.

The D peak, at 1325 cm^{-1} is due to the defects in the graphene sample. The mechanism for this is similar to the mechanism for the 2D peak[127]. For the D peak, the electron is scattered back to band 1 by an impurity. The Raman shift of the D peak is also dependent on the laser energy used. The D peak splits into two separate peaks when more than one layer of graphene is present. Therefore, both the D and 2D peaks broaden with the addition of more layers.

3.4.2 MoS$_2$

The Raman spectrum of MoS$_2$ shows two peaks at about 400 cm^{-1}, and a stronger peak at 520 cm^{-1}. The two peaks at 400 cm^{-1} are the E^1_{2g} and A_{1g} peaks, and the peak at 520 cm^{-1} is the peak associated with the Si substrate. The full Raman spectrum of MoS$_2$ on a 300 nm SiO$_2$ layer on a Si substrate is shown in figure 3.10, and the two peaks associated with MoS$_2$ are shown in more detail in figure 3.11a. They arise due to the in-plane optical vibration of the Mo and S atoms and the out-of-plane optical vibration of S atoms, respectively[128]. The separation of these two peaks is $18.4cm^{-1}$ for a monolayer of MoS$_2$, but increases when more layers are present, converging to the bulk limit of $25.1cm^{-1}$[129]. This can be used as an accurate method of determining the number of layers of MoS$_2$ in a sample[130]. The A_{1g} peak is seen to blue-shift at twice the rate that the E^1_{2g} peak is seen to red-shift with increasing layers of MoS$_2$. The interlayer Van der Waal forces are expected to increase the frequency of the vibrational modes, acting as a restoring force to the intra-layer vibrations. This is observed for the A_{1g} peak. The opposite behaviour of the E^1_{2g} peak could be attributed to structural change in the topmost layer due to the presence of the others. A decrease in distance of about 5% was observed between the topmost S layer and the corresponding Mo in the bulk, measured by low energy electron diffraction[131]. It is also possible that the decrease in vibrational frequency is due to long-range Coulombic interactions[132].

Photoluminescence (PL) is the light emitted from the spontaneous recombination of electrons and holes (excitons)[133]. The PL of monolayer MoS$_2$ is enhanced 10^4-fold in comparison with the bulk crystal. The PL reduces for each layer added in the few-layer case,

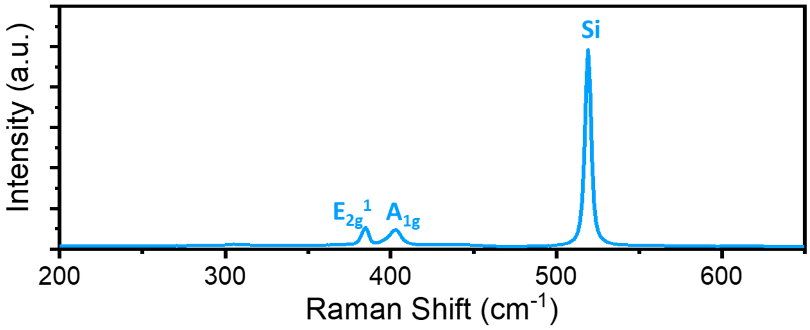

Figure 3.10: Raman spectrum of monolayer MoS_2 on SiO_2/Si surface grown by CVD.

converging to the bulk limit. This is because the PL of bulk MoS_2 is a phonon-assisted process (because of the indirect band-gap), resulting in almost negligible quantum yield. The monolayer PL peak at ≈ 1.88 eV matches the absorption peak in both energy position and width. It can therefore be attributed to a direct-gap luminescence[15]. A typical PL spectrum of a monolayer MoS_2 flake grown by CVD is shown in figure 3.11b.

Shi *et al.* (2012)[134] demonstrated the effects of reducing bulk MoS_2 to few- and single-layer samples. Quantum confinement was shown to have a very important effect, causing the exciton dynamics to deviate significantly from the bulk crystal. Faster electron-hole recombination was observed for the monolayer case due to the indirect to direct bandgap transition and the quantum confinement effect. The direct recombination was found to be ≈ 800 ps for the monolayer case, but the indirect recombination was > 2.3 ns for the bulk case, demonstrating why the PL intensity is strongest for the monolayer limit of MoS_2.

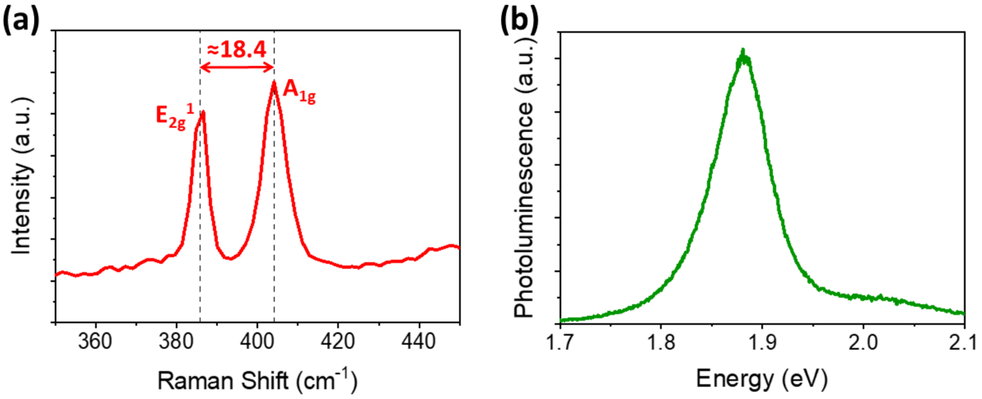

Figure 3.11: (a) Raman and (b) photoluminescence spectra of monolayer MoS_2 flakes grown by chemical vapour deposition.

3.5 Optical Measurements

The reflectance and scattering measurements in this thesis were taken with an Olympus upright microscope under white light excitation. Reflectance measurements were taken of Si disk arrays in chapter 6. These measurements were taken with the bright field mode using a 5x objective lens of numerical aperture 0.12. Measurements of scattering spectra were taken at the single particle level for chapters 4 and 5. These measurements were taken with the dark field mode using a 100x objective lens of numerical aperture 0.9. The spectra were recorded with an Andor CCD camera and an Andor 330i spectrometer.

Simple schematics of the bright and dark field modes are shown in figure 3.12a and b, respectively. In the bright field mode, reflected light is collected from the same direction as the incident light. The total reflectance is calculated using

$$R = \frac{I_{col}}{I_{inc}} \tag{3.23}$$

where R is the reflectance, I_{col} is the total intensity of the collected light and I_{inc} is the total intensity of the incident light. I_{inc} was calculated by focusing the incident beam on a Ag mirror, and collecting the total reflected light, equal to the incident light. From this measurement it is also possible to calculate the absorbance (A) of the system, assuming there is no transmittance (T). This is because $R+A+T=1$, so $A=1-R$ when $T=0$.

In the dark field mode, the incident light hits the sample in a cone formation, and the light scattered upwards is collected. The scattering intensity (I_{scat}) from each particle is found by

$$I_{scat} = \frac{I_P - I_{BG}}{I_{BG}} \tag{3.24}$$

where I_P is the intensity of scattered light measured from the particle and I_{BG} is the intensity of light scattered from the background material surrounding the particle. The measurement of I_{BG} was taken with the same slit width as the measurement of the nanoparticle, directly beside each nanoparticle measured.

A Cary 50 UV-vis spectrophotometer was used to measure the extinction spectra of liquid samples containing nanoparticles. Examples of these are shown in section 3.2.2, showing the extinction spectra of samples of Au bipyramids. No spectra are shown for the Au nanospheres because the yield was too low. A beam of light was passed through the liquid sample in a cuvette, with the total transmitted light collected and measured. The extinction (total absorbed and scattered light) was found by subtracting the intensity of the transmitted light from the incident light.

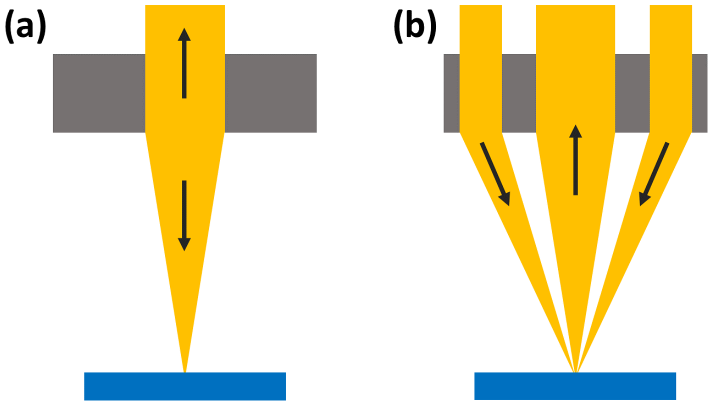

Figure 3.12: Schematic for measurements taken with an optical microscope with the (a) bright field and (b) dark field objectives.

3.6 Scanning Electron Microscopy

All scanning electron microscopy (SEM) images in this thesis were recorded using a Carl Zeiss Ultra SEM. SEM was employed to image all nanostructures used, giving information about their size and shape that would not be possible to measure with an optical microscope. This is because there is a wavelength-dependent limit of the optical resolution, the Abbe limit, approximated as

$$d = \frac{\lambda}{2nsin\theta} \tag{3.25}$$

where d is the maximum resolution length for wavelength λ, n is the refractive index and θ is the angle of the converging light from the normal direction. Therefore, the theoretical maximum resolution for any optical microscope is $\frac{\lambda}{2}$. The visible wavelength range is from 400 nm to 700 nm, making the visualisation of nanoparticles with a traditional optical microscope impossible.

The de Broglie wavelength of an electron is given by

$$\lambda = \frac{h}{mv} = \frac{h}{\sqrt{2meV}} \tag{3.26}$$

where h is Planck's constant, m is the electron mass, v is the electron velocity and V is the accelerating voltage applied to the electron. A higher accelerating voltage increases the velocity of the electron, according to the equation showing the energy of the electron.

$$E = \frac{1}{2}mv^2 = eV \tag{3.27}$$

Therefore, the de Broglie wavelength, and hence, d can significantly reduce with an increased V, allowing for the imaging of nanostructures.

Images are primarily generated from the back-scattered electrons (BSE) and secondary electrons (SE). The back-scattered electrons scatter elastically from the sample, with more electrons back-scattering for materials with high atomic numbers. There are three different types of secondary electrons, SE1, SE2 and SE3. SE1 electrons are generated directly where the impacting electron beam meets the surface of the sample. SE2 electrons emit further from the point of original impact, and are generated after multiple scattering within the sample. SE3 electrons are generated from back-scattered electrons impacting in the sample further away from the spot hit by the original electron beam, and are not useful for the image generation.

The in-lens detector is positioned above the objective lens in the SEM. The primary electrons are decelerated as they pass through the objective lens by 8 kV, so that the secondary electrons can be accelerated after they are scattered back up through the objective lens towards the in-lens detector. The in-lens detector collects SE1 and SE2 electrons, with almost no back-scattered or SE3 electrons. This makes it ideal for detecting surface information. Images taken with the in-lens detector, however, appear flat, with very little topological information. This is because the in-lens detector is placed directly above the sample.

The SE2 detector is positioned to the side, below the objective lens, mounted on the specimen chamber wall. A collector voltage is applied to the SE2 detector, allowing for the collection of low-energy secondary electrons that are not directed towards it to be collected. The collector voltage can also be set to a negative value, adjusted to only collect the highest-energy back-scattered electrons. The surface information given with the SE2 detector is lesser than the in-lens detector due to the back-scattered electrons detected alongside the secondary electrons. The back-scattered electrons originate from further within the sample than the secondary electrons, obscuring the surface information of the secondary electrons. The SE2 detector can give more topological information than the in-lens detector because of its position at the side to the specimen chamber. For both high surface information and topological information, a superposition of images from both the in-lens and SE2 detectors should be used.

Figure 3.13a and b show the contrast of a Au nanosphere imaged with (a) the in-lens and (b) the SE2 detectors as in chapter 4. The higher quality of surface information is evident in this image. The structures studied in this thesis are primarily composed of single nanoparticles and arrays of nanoparticles, reducing the need for high topological information. Therefore, all images were taken with the in-lens detector, giving greater resolution on the sample surface.

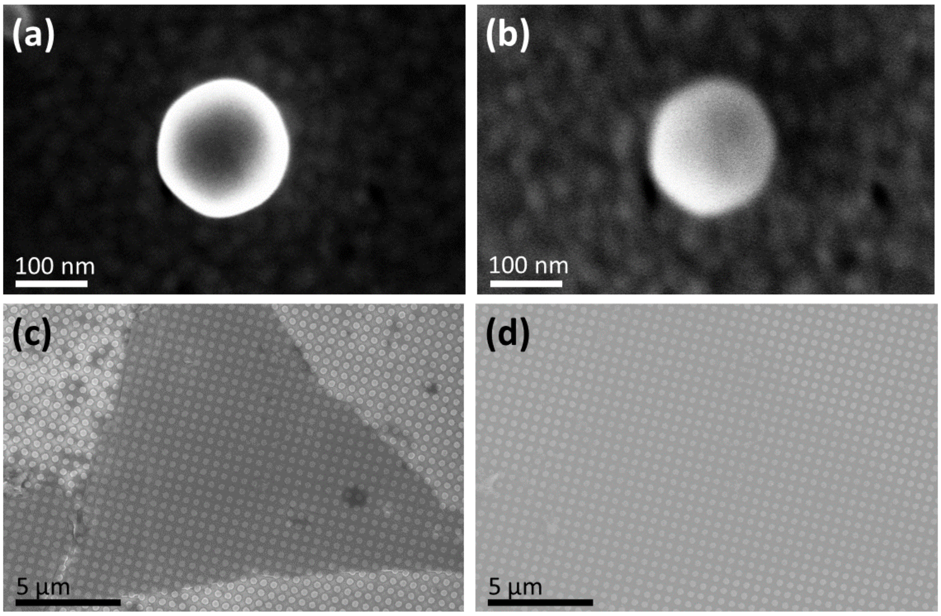

Figure 3.13: (a,b) Au nanosphere as in chapter 4 imaged with the inlens and SE2 detectors, respectively. (c,d) Si disk array with a monolayer of MoS_2 on top as in chapter 6, imaged with the inlens and SE2 detectors, respectively.

Another advantage of the in-lens detector is that it is possible to use it to image 2D materials. Figure 3.13c and d show images of the same position of a Si disk array with a monolayer of MoS_2 on top, as in chapter 6, taken with the in-lens and SE2 detectors, respectively. The position is evident in the in-lens image, with the MoS_2 flake much darker than the surrounding material. This is because the primary electrons have high enough energy to penetrate through the MoS_2 layer, but the MoS_2 has a screening effect on the lower-energy secondary electrons scattered back upwards. This causes the darkening effect, with fewer electrons being detected in the presence of the MoS_2 layer. This effect is less pronounced in the SE2 image due to the presence of the back-scattered electrons. Further, the back-scattered electrons are more likely to be scattered by the Mo in the MoS_2 layer due to its high atomic number in comparison to the surrounding material.

3.7 Photolithography

In chapters 4 and 5, single particle scattering spectra were correlated with SEM images of the same particles. To ensure that the corresponding spectra and SEM images could be paired correctly, a grid was printed on the substrates. This was achieved with photolithography. Photolithography is preferable to electron beam lithography (EBL) for larger structures because it utilises pre-made masks with the desired pattern. This allows for many samples to be printed in quick succession, with a low energy cost, unlike EBL which requires the electron beam to be focused individually on each pattern feathure for each sample made.

The samples were heated for 5 minutes at 150°C, before spinning on S1813 resist. They were then heated for 75 seconds at 115°C. The grid pattern was printed on the resist with an OAI mask aligner. The samples were developed with MF-319 developer for 40 seconds, before being immersed in deionised water to stop the reaction.

The metal for the grids was deposited on the samples by electron beam evaporation with a Temescal. For samples on SiO_2, as in chapter 5, a 35 nm Au layer with a 5 nm Ti adhesion layer were deposited. For samples on an Au film, as in chapter 4, the Au in the grid was replaced with Ag.

Acetone was used to etch away the metal on the resist, leaving behind the grid pattern. The samples were then cleaned with IPA, and dried with a nitrogen gun.

3.8 Conclusion

In conclusion, this chapter introduces all techniques, computational and experimental, involved in this work. The principles of FDTD, the simulation methodology for each chapter in this work, were described. The methods for all fabrication techniques were presented, including the growth of both plasmonic nanoparticles and 2D materials. Finally, the measurement and characterisation techniques were given. These involved optical measurements including PL, Raman, dark field, reflectance and UV-vis. SEM was also employed to visualise the nanostructures measured with the listed optical techniques. It was possible to correlate the SEM images with the individual nanoparticles measured by creating a grid on the sample substrate using photolithography.

> Think left and think right and think low
> and think high. Oh, the thinks you can
> think up if only you try!
>
> Dr. Seuss

4 Spectral Tuning of a Nanoparticle-on-Mirror System with Graphene

4.1 Introduction

The sub-nanometer control of the separation between two metal nanoparticles is of high interest due to the many applications involved exploiting the ability to trap light at the sub-wavelength scale[135, 136]. These include optical switching[137, 138], energy harvesting[22] and molecular detection and sensing[18, 19, 20]. The use of these nanogaps has made it possible to greatly increase the confinement of light to scales of less than one nanometer[135]. It is possible to achieve this effect by confining the light between two nanoparticles, for example in a bowtie formation. This can be done by creating an array of nanoparticles by electron beam lithography, allowing the precise positioning of the nanoparticles to give control over the nanogaps created[77, 139, 140]. Utilising a nanoparticle-on-mirror (NPoM) approach, however, gives stronger and more reproducible gap control. This is achieved by placing a metallic nanoparticle on top of a metallic film, allowing the nanoparticle to couple to its mirror image in the film. The NPoM approach retains the same confinement effects as two nanoparticles coupled together, but instead involves the coupling of a nanoparticle with its mirror image[135].

Two-dimensional materials are interesting to combine with the NPoM geometry. This is because the light is confined within dimensions similar to the atomic thickness material. This gives rise to a pathway for much higher light-matter interaction for 2D materials, allowing much deeper exploration into their optical properties[40, 141, 142]. Another advantage of utilising 2D materials in these systems is that their thicknesses are well known, and constant at the monolayer limit. This constant gap thickness can be useful by keeping the gap size fixed while monitoring other changes in the plasmonic system[143]. Graphene has a tunable surface conductivity response that can be modified by doping both chemically and electrically. This can be manipulated for a wide variety of applications, including a hyperlens, a metacoupler and super-resolution imaging and sensing[144, 145]. Many studies have explored the coupling of graphene to plasmonic structures, mostly in the infrared region. It has been demonstrated that graphene can be used to modulate the plasmonic response by modifying the dielectric properties[146, 147, 148, 149, 150, 151, 152, 153]. This can be achieved by both electrical gating and chemical doping. When the graphene layer overlaps with the electric field hot spot, it can have remarkable effects on the modulation of the plasmonic spectra, even in the visible wavelength range[39, 40, 151, 154].

Two separate works, Shao *et al.*[39] and Mertens *et al.*[40] investigated a system involving a Au nanosphere on top of a Au film, with an intermediate layer of graphene. These systems demonstrated optical modulations, tuned by graphene, in the visible to near-infrared spectrum. This makes these works particularly interesting, as most systems involving the tuning of plasmonic energies with graphene are limited to the infrared region. Both works showed the formation of three different peaks in the scattering spectra. Shao *et al.* attributed the three peaks to the octupolar, quadrupolar and dipolar modes. Mertens *et al.* attributed the three peaks to the transverse plasmon and the coupling between the charge-transfer plasmon (P_{CTP}) and gap plasmon (P_{GAP}).

In this chapter, evidence is presented to show that both of these theories are correct and we demonstrate the conditions under which each is the dominant effect. The system involves a Au nanosphere of 150 nm in diameter, on top of a 100 nm thick Au film, with an intermediate layer of graphene, as shown in figure 4.1. The Au film is on top of a 100 nm thick SiO_2 layer on a Si substrate. Several plasmon modes are visible in the scattering spectrum of this system. Nitric acid is employed to modulate theses modes by two different mechanisms. It serves to dope the graphene, and also to reduce the gap size in between the Au nanosphere and film. The results demonstrate the unification of the theories presented by both Shao *et al.* and Mertens *et al.*, and the regimes in which each is observed.

4.2 Device Design and Fabrication

A 100 nm Au layer was deposited on the SiO_2/Si substrates by electron beam evaporation with a Temescal. The monolayer graphene was grown by chemcial vapour deospsiton (CVD), due to its high monolayer coverage. The CVD graphene was grown and transferred onto the target substrates by the method described in section 3.3.1. The graphene was doped by immersion for five minutes in nitric acid of varying concentrations[49].

Raman maps of the same region of graphene on a SiO_2/Si substrate after immersion

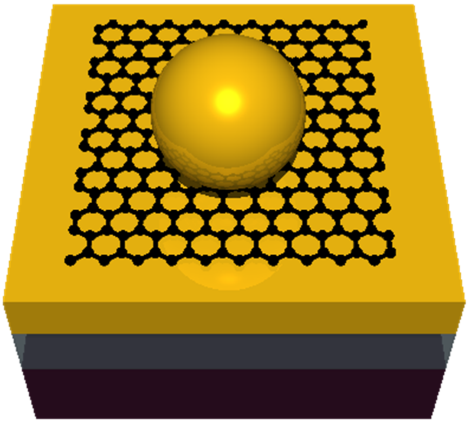

Figure 4.1: Schematic of the system studied with a 150 nm Au nanosphere on a 100 nm Au film separated by an intermediate monolayer of graphene. The system is on top of a 100 nm SiO_2 layer on a Si substrate.

---

in nitric acid of concentrations 0% to 70% are shown in figure 4.2a. The same sample of graphene was immersed in the different concentrations of nitric acid, from a low concentration to a high concentration, with Raman measurements being taken in between. The graphene was not washed in between immersions within the different solutions of nitric acid to ensure the doping level increased between each measurement and to minimise damage to the graphene layer. The Raman maps illustrate the red-shifting of the G and 2D peaks as well as the reduction of the intensity of the 2D peak as the graphene doping level increases. They also show that the D peak intensity remains low for all of the scans, indicating the high quality of the graphene used. After immersion in the 70% nitric acid, there are some areas where the D peak becomes more prominent, indicating that there was a small amount of damage within the graphene monolayer.

Figure 4.2b shows the Raman spectra averaged from the maps in figure 4.2a, and figures 4.2c and d show the average positions of the G and 2D peaks and the intensity ratio of the 2D and D peaks to the G peak, respectively. The G peak is shown to red-shift from 1588.9 ± 1.9 cm^{-1} to 1593.3 ± 2.7 cm^{-1} after immersion in 5% and 70% nitric acid, respectively. The 2D peak is shown to red-shift from 2642.4 ± 4.0 to 2649.0 ± 5.1 cm^{-1}, and the intensity ratio of the 2D peak to the G peak, I_{2D}/I_G, reduces from 1.3 ± 0.2 to 0.6 ± 0.2. This indicates that the p-doping can be estimated to be $\approx 4 \times 10^{13}$ cm^{-2} after doping the graphene in 70% nitric acid, with an average chemical potential of about ≈ 0.8 eV[155]. The doping for the purpose of this work was achieved by simply immersing the graphene in nitric acid, but it is possible to increase the doping level and its stability by annealing the

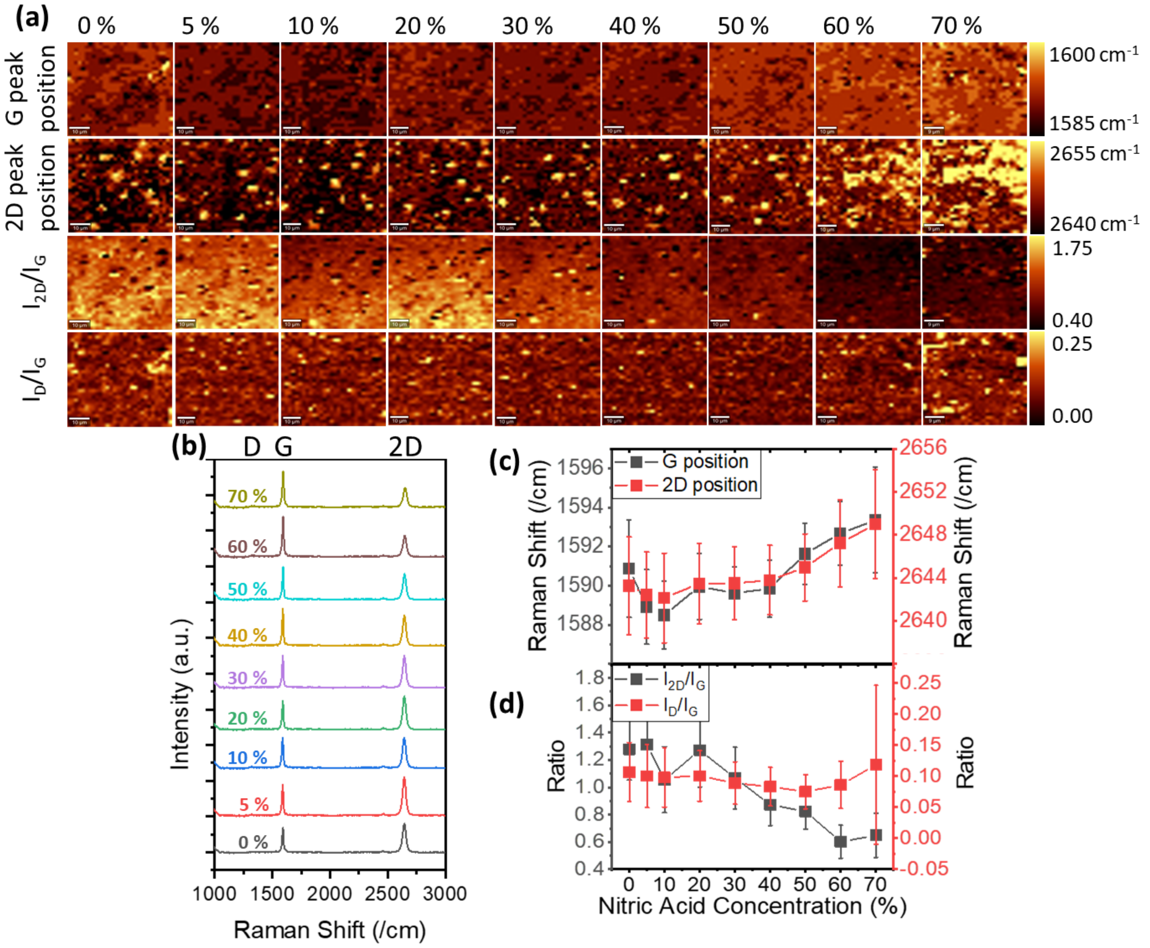

Figure 4.2: (a) Raman maps of the same area within a graphene sample, showing the position of the G peak and the 2D peak and the intensity of the 2D peak and the D peak after each immersion in nitric acid from 0% to 70%. (b) Raman spectra averaged over each map shown in (a). (c) Positions of G peak and 2D peak taken from (a). (d) Ratio of the intensities of 2D peak and D peak to the G peak taken from (a). The data points show the mean value and the error bars show the standard deviation. The blue-shifting of the G peak and the 2D peak and the reduced intensity of the 2D peak indicate a high level of doping. The D peak has a very low intensity for all spectra, indicating the high quality of the graphene.

---

sample after the nitric acid treatment[49].

The ratio of the intensity of the D peak to the G peak, I_D/I_G, was changed from 0.10 ± 0.05 to 0.12 ± 0.12 after changing the concentration of nitric acid from 5% to 70%. This is due to a very low D peak intensity, indicating the high quality of the graphene layer. The standard deviation is very high when the graphene is highly doped from 70% nitric acid. This is because only a few small areas of the graphene measured show a D peak with increased intensity, while the D peak remains low for the rest. This effect is shown in figure 4.2a, where the map of I_D/I_G remains dark with a few bright spots. This indicates that the graphene remains of a high quality when it is highly doped with 70% nitric acid, but with a few small areas of slight damage.

As can be seen in figure 4.2a, the overall peak positions and relative intensities are not at the exact same level across a given Raman map. This is evident in the bright and dark spots visible in each map. While each small section of graphene is not identical in the Raman maps, it is clear that there is a definite trend of the peaks shifting in one direction as the doping of the nitric acid increases.

The electrical resistivity of the graphene was also measured after the immersions in the different concentrations of nitric acid. The graphene was placed on a SiO_2/Si substrate for this. These measurements were taken with an Ossila four-point probe system. The probe spacing was fixed at 1.27 mm for all measurements taken. Therefore any lack of uniformity, breaks or tears in the graphene monolayer would have a high influence on the results measured. It was found that the measured resistivity was highly dependent on the positions of the probes on the sample, indicating some non-uniformity in the monolayer graphene layer. Raman spectra taken in the region of a tear in the graphene would not show any peaks characteristic of graphene, as the graphene in that region was removed. For the measurements of nanoparticles on top of the graphene layer, this was not a problem. This is because it would not be possible to remove the graphene layer between the nanoparticle and film without also removing the nanoparticle. Therefore, every particle that stayed in place between each immersion in the nitric acid solutions had the same layer of graphene underneath as was there at the beginning.

After the graphene sample was immersed in each concentration of nitric acid, six different resistivity measurement were taken, with the probes positioned on different parts of the sample for each measurement. The measurement with the lowest resistivity result was taken as the resistivity of the graphene for that doping level. This minimised the measurements of tears or breaks within the graphene layer. The results are shown in figure 4.3. While these measurements do not give accurate numbers for the exact resistivity of the graphene layer, they do indicate an overall trend. It is clear from this plot that the nitric acid is reducing the resistivity of the graphene, showing that as the nitric acid concentration increases, the doping level also increases[49, 155].

Both the Raman spectroscopy (figure 4.2) and resistivity (figure 4.3) measurements indicate that the doping of the graphene layer was reduced when the sample was immersed in 5% nitric acid before being increased again for higher concentrations of nitric acid. This indicates that the newly-grown graphene was slightly n-doped before being treated with nitric

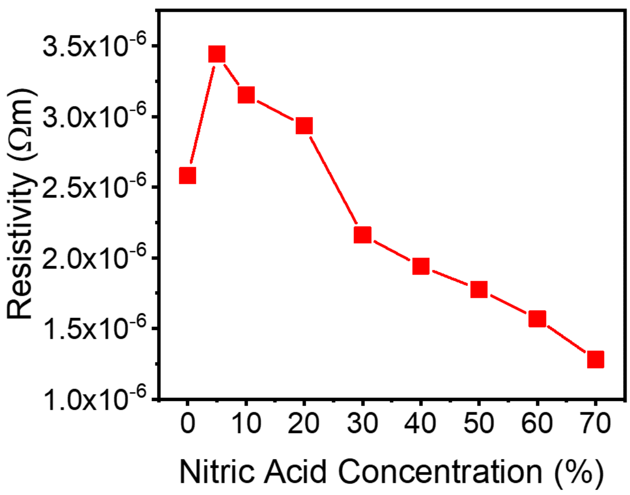

Figure 4.3: Resistivity measured for the same graphene sample on 100 nm SiO_2 on a Si substrate measured after being immersed in nitric acid for five minutes in concentrations from 0% up to 70%.

acid, resulting in a higher level of p-doping.

Au nanospheres were synthesised with a wet chemistry approach, as described in section 3.2.1. This method was chosen to obtain a high yield of nanospheres that were uniform in size and highly spherical. The product was diluted in ethanol and sonicated for $\approx$ 3 minutes before drop-casting onto the substrates. The 150 nm Au nanospheres were drop-cast onto the Au film with a graphene monolayer on top, the Au film without a graphene monolayer, the SiO_2/Si substrate with a graphene monolayer on top and the SiO_2/ Si substrate without a graphene monolayer. The substrates were heated for 10 minutes in 40°C acetone after the deposition to reduce the CTAB (cetrimonium bromide, [(C16H33)N(CH3)3]Br) layer surrounding the particles[149]. This also helped to reduce the amount of residual PMMA remaining on the graphene.

Measurements of scattering spectra were taken at the single particle level under white light excitation with a dark field microscope using a 100x objective lens of numerical aperture 0.9. The spectra were recorded with an Andor CCD camera and an Andor 330i spectrometer. Approximately 50 measurements were taken for single nanospheres drop-cast onto each of the four different substrates considered.

FDTD simulations were carried out using Lumerical solutions. These were used to illustrate how the gap size and changes to the permittivity of the graphene layer modulate the energy of the plasmon modes. The nanospheres were modelled with diameter 150 nm, and approximated as perfect spheres. The dielectric function of Au was taken from a fit of the points measured by Johnson and Christy[156], and the gap between the nanosphere and graphene layer was modelled with the permittivity of of 1.5 to approximate the polymer and CTAB layer[157].

The graphene was modelled with thickness 0.5 nm, with the dielectric function, ε_G, taken from Stauber *et al.*[158]. This model was chosen as it is valid for visible wavelengths. It describes the real (σ_r) and imaginary (σ_i) components of the optical conductivity of graphene with the following equations:

$$\sigma_0 = \frac{\pi e^2}{2h} \tag{4.1}$$

$$\sigma_r(\omega) = \frac{\sigma_0}{4!2^4}\left(\frac{\hbar\omega}{t}\right)^2\left(tanh\frac{\hbar\omega+2\mu}{4k_BT} + tanh\frac{\hbar\omega-2\mu}{4k_BT}\right) \tag{4.2}$$

$$\sigma_i(\omega) = \frac{\sigma_0}{\hbar\omega}\frac{4}{\pi}\left(\mu - \frac{2\mu^3}{9t^2}\right) - \frac{\sigma_0}{\pi}log\frac{|\hbar\omega+2\mu|}{|\hbar\omega-2\mu|} - \frac{\sigma_0}{36\pi}\left(\frac{\hbar\omega}{t}\right)^2 log\frac{|\hbar\omega+2\mu|}{|\hbar\omega-2\mu|} \tag{4.3}$$

where e is the charge of an electron, h is Planck's constant, ω is the angular frequency of the light, t is the hopping parameter of first-nearest neighbours in Stauber's model[158], taken as 3 eV, μ is the chemical potential of the graphene, k_B is the Boltzman constant and T is the Kelvin temperature. The permittivity of the graphene layer can then be found from the optical conductivity model shown above as follows[39].

$$\varepsilon_G = \frac{i\sigma(\omega)}{\omega\varepsilon_0 d} \tag{4.4}$$

where σ is the optical conductivity of graphene, ω is the angular frequency and d is the thickness of the graphene monolayer. The real and imaginary permittivity of graphene, for chemical potentials varying from 0.1 to 1.2, is shown in figure 4.4a and b, respectively.

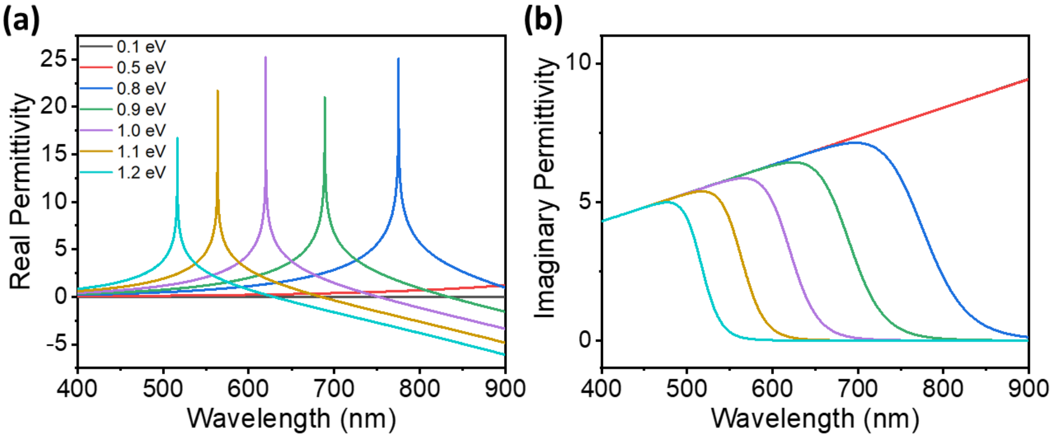

Figure 4.4: (a) Real and (b) imaginary permittivity of a monolayer of graphene as calculated by Stauber *et al.*[158].

4.3 Multipolar Modes in the Nanoparticle-on-Mirror System

Example experimental scattering spectra of four different nanospheres are shown in figure 4.5(a-d). Corresponding SEM images of the particles measured are shown to the right of each scattering spectrum, and a schematic of each system is shown underneath. The scattering spectrum of the Au nanosphere and Au film with the intermediate monolayer of graphene is shown in figure 4.5a. Three peaks are visible in this spectrum, corresponding to the octupolar (570 nm), quadrupolar (597 nm) and dipolar (732 nm) modes, respectively, as identified by Shao *et al.*[39]. The octupolar peak is visible as a shoulder to the quadrupolar peak.

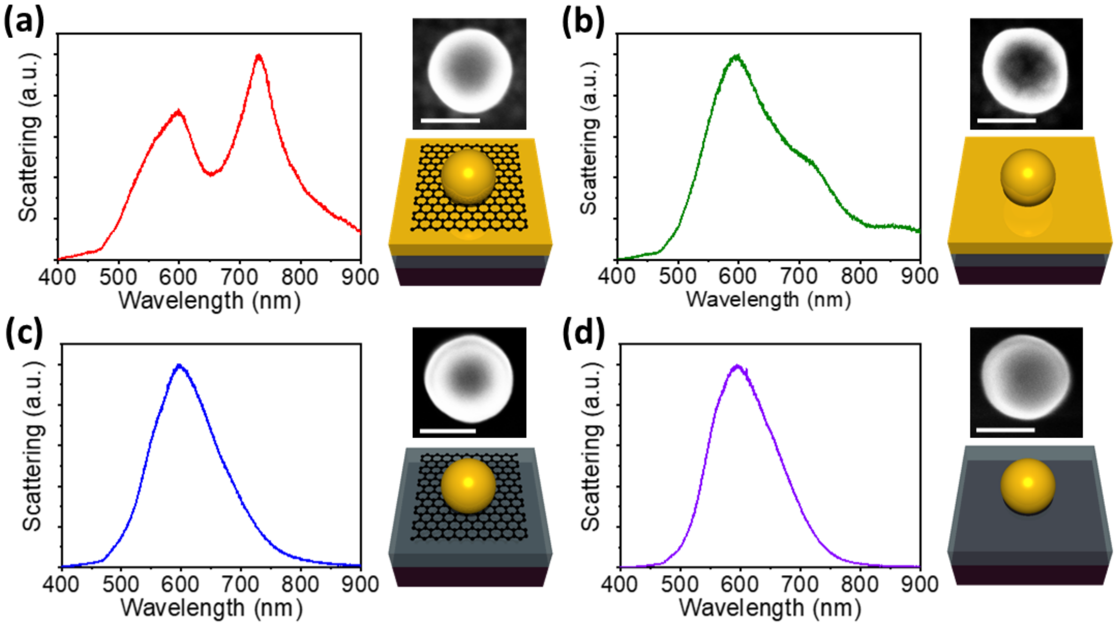

Figure 4.5: (a-d) Experimental scattering results from single 150 nm Au nanospheres (a) on top of a monolayer of undoped graphene on a Au film, (b) directly on top of the Au film, (c) on top of a monolayer of undoped graphene directly on the SiO_2/Si substrate and (d) directly on the SiO_2/Si substrate. An SEM image of the particle measured, with scale bar showing 100 nm is shown to the upper right of each plot. A schematic of each system is shown to the lower right of each plot.

Electric field maps from a simulation of this system are shown in figure 4.6a at the energy corresponding to the quadrupolar mode. The top panel shows the cross section through the center of the sphere and the substrate underneath, and the bottom panel shows the cross section on the top of the Au film directly underneath the sphere and graphene. It is clear from these two maps that the electric field is highly confined in the gap between the Au sphere and film, where the graphene is positioned. This elucidates how this structure can be utilised to maximise the interaction of the plasmonic resonances with a graphene monolayer.

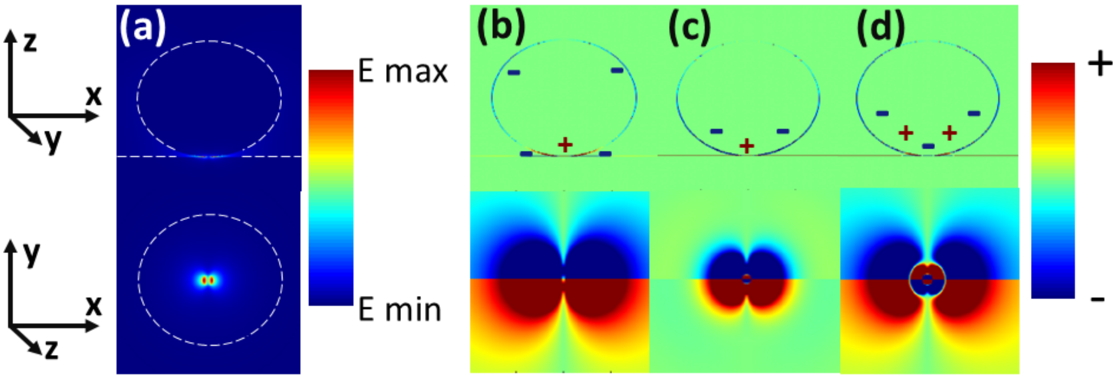

Figure 4.6: Simulated results from a 150 nm Au nanosphere on a monolayer of graphene on the Au film. The gap between the Au sphere and graphene layer is 1 nm and the graphene has a chemical potential of 0.1 eV. The results show (a) electric field maps at the energy of the quadrupolar mode. These are shown through the center of the sphere and the substrate, and at the surface of the Au film, directly underneath the sphere. Contours of the particle and Au film are indicated by the white dashed lines. (b-d) Surface charge distribution maps at the positions of the dipole, quadrupole and octupole, respectively. The cross-section of each map is 200 nm × 200 nm.

The simulated surface charge distribution maps are shown in figure 4.6b-d. These maps show the same planes through the center of the sphere and the substrate and at the top of the Au plane, underneath the nanosphere, as in the electric field maps. They are taken at the energy of the multipolar modes, and correspond to the simulated spectrum in figure 4.8b, of chemical potential 0.1 eV. The lowest energy peak shown in figure 4.6b, corresponding to the peak at 732 nm in the experimental scattering spectrum, is clearly a dipolar mode. Similarly, higher orders of multipoles are evident in figures 4.6c and d, corresponding to the peaks at 597 nm and 570 nm in the experimental spectrum. The top panel in figures 4.6b-d show some features that do not correspond to the dipolar mode. This is because some of the charge in the Au sphere leaked into the polymer and CTAB layer, modelled with permittivity 1.5. Simplified results of the same simulation with the polymer area replaced with air are shown in figure 4.7, demonstrating a clearer dipolar mode when there is no polymer layer for the charge to leak into.

An experimental scattering spectrum of the same system, without the graphene monolayer is shown in figure 4.5b. This spectrum also shows several peaks corresponding to different multipolar modes. There is some variation of where the peaks were positioned for this system, across the different particles measured. As will be discussed below, this is due to the high sensitivity of the plasmon modes to the gap size between the Au nanosphere and

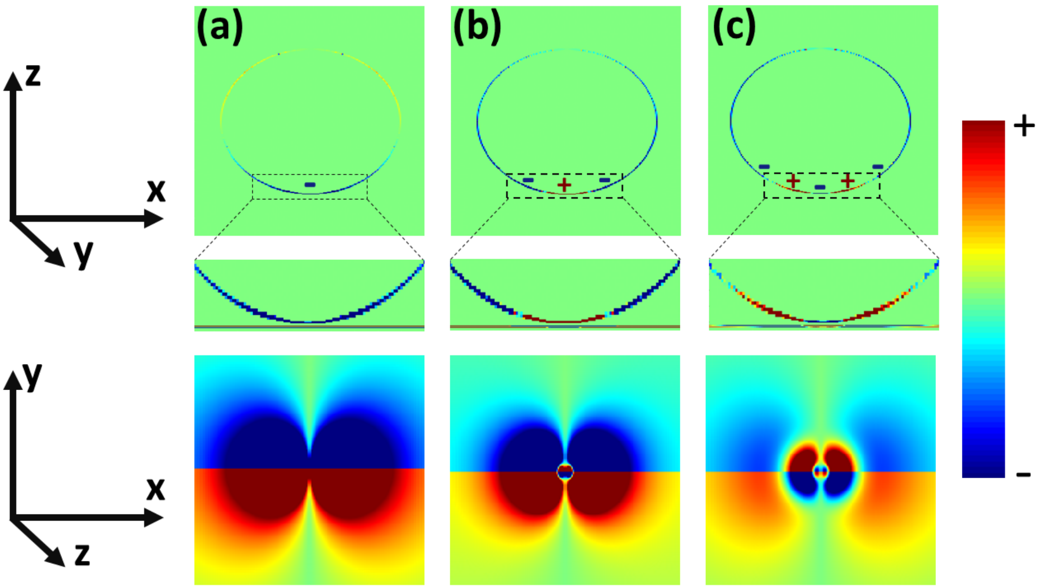

Figure 4.7: Surface charge distribution maps from simulations as in figure 4.6e, but replacing the polymer layer with an air layer. The top panel shows the surface charge distribution through the center of the nanosphere and the substrate, with a closer map shown below giving better resolution to the charge at the top of the Au film and the graphene layer. The bottom panel shows the surface charge distribution at the top of the Au film, directly underneath the Au sphere. Each map shows a cross setion of 200 nm × 200 nm, with the closer-up versions of the top panel maps showing 100 nm × 23 nm. The maps show the surface charge distribution for the (a) dipolar, (b) quadrupolar and (c) octupolar modes. These maps give a simplified approximation to figure 4.6e, as in this case the charge in the sphere does not leak out into the polymer layer.

---

film. This gap can vary by up to $\approx$ 1 nm between nanoparticles. This gap is due to the CTAB layer coating the nanospheres, residual from after heating the substrates in acetone. All four substrates were heated in 40°C acetone to reduce the CTAB layer after the nanospheres were drop-cast[149]. This CTAB layer had the same effect on both the nanoparticles on and off the graphene layer, but only the nanoparticles on the graphene had the PMMA layer.

Experimental scattering spectra of Au nanospheres directly on the SiO_2/Si substrate, with and without a monolayer of graphene are shown in figures 4.5c and d, respectively. Both spectra show one broad peak at $\approx$ 600 nm, comprised of the different multipolar modes too close together to resolve. The lack of the Au film underneath significantly reduces the electric field strength and the interaction between the plasmons and the graphene, resulting in no notable differences between the spectra of the spheres with and without a monolayer of graphene between them and the SiO_2/Si substrate.

4.4 The Effect of Graphene Doping and Gap Size

Gap plasmons have a very high sensitivity to their environment. Therefore, a myriad of factors can cause slight discrepancies between the experimental results from different particles, including the particle shape, size, gap size and surface roughness of the Au film. Due to these small differences between different particles, the simulations employed in this paper are used only to show global trends. The systems corresponding to the spectra in figure 4.5 are simulated with an idealised model, assuming the nanoparticles are perfect spheres of 150 nm diameters, and placed on substrates with completely flat surfaces. These approximations are used to keep the simulations simple and to best observe the trends involved in the evolution of the spectra as the gap size between the nanosphere is modified or as the graphene layer is doped. This simple model is not used to find an exact fit for each experimental spectrum. Therefore, there is a slight discrepancy between the peaks corresponding to each mode in the experimental spectra (shown in figure 4.5) and the simulated spectra (shown in figure 4.8 and 4.10).

The effect of the doping of the graphene layer is shown in figures 4.8a and b. Both plots show the simulated scattering spectra of a Au nanosphere on top of 100 nm Au film, separated by a monolayer of doped graphene. In figure 4.8a, the gap between the sphere and the top of the graphene layer is 0.25 nm, while in figure 4.8b, the gap is 1 nm. In both cases, the dipolar mode is shown to blue-shift as the doping level goes up. This effect is more extreme in the case of the smaller gap size. It blue-shifts by 45 nm in figure 4.8a when the doping is increased from 0.1 eV to 1.1 eV, but it only blue-shifts by 30 nm in figure 4.8b. The blue-shifting of the dipolar mode is due to the reduction of the real part of the permittivity of the graphene at higher doping levels[39, 147, 149]. When the doping level is brought as high as 1.2 eV, the dipolar mode splits in two in figure 4.8b, and all of the modes split in figure 4.8a. The mechanics behind this phenomenon will be discussed in chapter 4.6.

The maximum electric field strength within the graphene layer is shown in figure 4.9. The electric field strength is calculated at the energy of the dipolar, quadrupolar and octupolar modes for a 150 nm Au sphere on a Au film, sandwiching a graphene monolayer with chemical potential 0.1 eV. The gap between the Au sphere and the graphene layer was varied from 0 to 1.5 nm. For each of the multipolar modes, the E field is clearly shown to reduce as the gap is made larger. This shows the importance of keeping the gap size small and minimising the thickness of the CTAB and PMMA layers. It also elucidates how this system can be utilised with fine control to achieve very high electric field intensities, concentrated

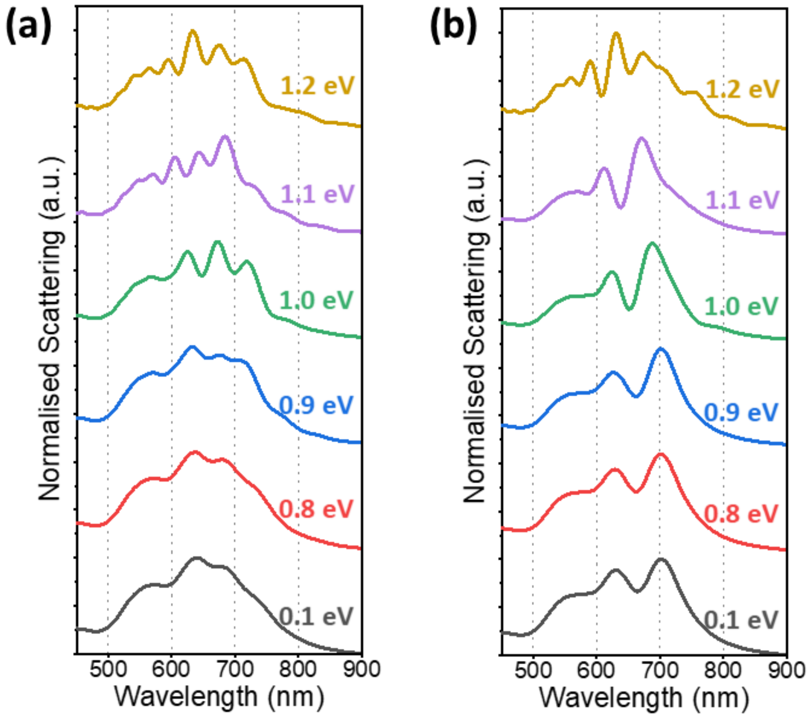

Figure 4.8: Simulated scattering spectra for a 150 nm Au sphere on a 100 nm Au film, sandwiching a monolayer of graphene on a SiO_2/Si substrate with a (a) 0.25 nm and a (b) 1 nm gap between the sphere and the graphene, respectively. The chemical potential of the graphene is increased from 0.1 eV to 1.2 eV.

in the graphene layer. The electric field strength is shown to reach as high as 890 V/m for the dipolar mode when there is no gap between the nanosphere and graphene layer. This is a significant field enhancement, as the incident field strength in Lumerical solutions is 1 V/m. A higher electric field strength overlapping with the graphene layer allows a stronger interaction between the plasmon and the thin 2D material. This is why the blue-shifts of the multipolar modes were shown to be larger for the doped graphene for a smaller gap size as demonstrated in figure 4.8.

Another difference between the spectra in figures 4.8a and b is seen in the higher energies of the modes in the latter. This is more evident when looking at the sharper peaks when the graphene is more highly doped. For example, when the chemical potential is set to 1 eV, the dipole mode is positioned at 688 nm and 717 nm when the gap size is 1 nm and 0.25 nm respectively. This effect can be understood by comparing the system to a capacitor, with the charge built up on either side of the gap, driven by the incoming light. This higher energy is due to the increased gap, causing a reduced capacitance between the Au sphere and film, increasing the oscillation period. Therefore, a lower capacitance causes the energy of the

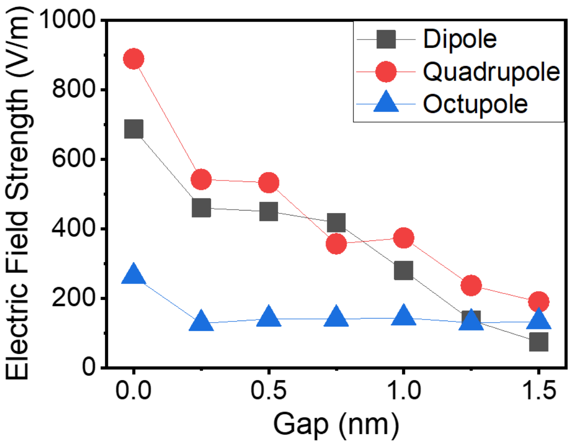

Figure 4.9: Plot showing the maximum electric field strength within the graphene layer at the energy of the dipolar, quadrupolar and octupolar modes for varying gap sizes between the Au sphere and graphene layer. Results were taken from simulations of a 150 nm Au nanosphere on a 100 nm Au film with the chemical potential is fixed at 0.1 eV.

---

plasmonic mode to increase. This effect is also seen in figure 4.10a, where the system is modelled without a graphene layer. The gap between the nanosphere and film is reduced from 1.5 nm to 0 nm, with the edge of the sphere only just coming into contact with the film. The scattering peaks are seen to red-shift[159], with more multipolar modes appearing as the gap size is brought to just 0.25 nm. A schematic illustrating the effect of the sphere being brought closer to the Au film is shown to the right of this plot. The PMMA layer modelled as a medium of refractive index 1.5 has the effect of some extra small peaks forming in the spectra due to the charge leaking described in section 2. Versions of figures 4.8a and b and figure 4.10a are shown in figure 4.11, with the PMMA modelled as air instead. These plots give a clearer view of the trends occurring due to the change of gap size and chemical potential.

When a Au nanoparticle is brought into contact with a Au substrate, a neck is formed in between them by the rearrangement of the atoms of the nanoparticle touching the sphere[40, 160, 161, 162]. With the formation of this neck, it is no longer possible for the multipolar modes to form because the capacitor effect cannot occur without the gap region between the Au sphere and film. Simulations of this effect are shown in figure 4.10b, with the radius of the neck being increased from 20% of the radius of the nanosphere to 100% of the radius of the nanosphere. This is illustrated to the right of the plot. When the neck is still small compared to the radius of the diameter, some plasmonic modes are still visible in the scattering spectrum, suggesting that the sphere can still couple with the film for very small neck

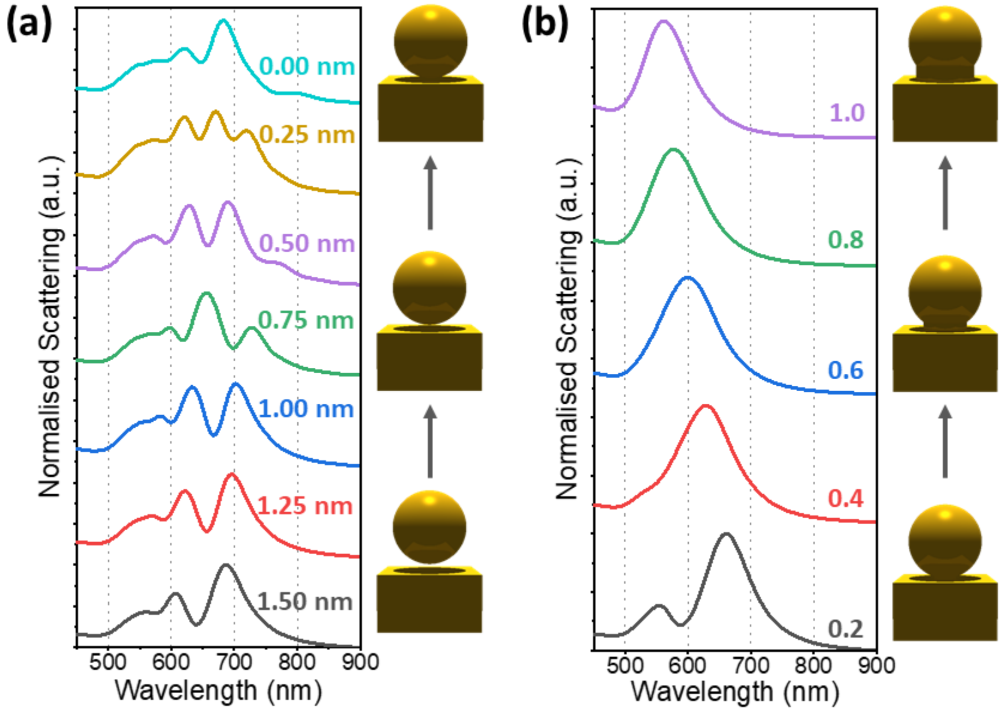

Figure 4.10: (a) Simulated scattering spectra for the same system, without the graphene layer. The gap between the Au film and Au sphere is reduced from 1.5 nm to 0 nm. This effect is illustrated to the right. (b) Simulated scattering of the same system as in figure (c), but with no gap between the Au sphere and film. The system is simulated with a neck formed between the sphere and film, with the ratio of the neck to sphere diameter being increased from 0.2 to 1. This effect is illustrated to the right.

sizes. As the neck size is increased, however, the scattering peaks collapse into one, showing that the coupling between the sphere and film is no longer happening. As the neck radius increases, the plasmon is shown to blue-shift. This result is supported by similar findings in the literature[160, 162].

4.5 Nitric Acid for the Control of both Doping of Graphene and Gap Size

The two effects described above were experimentally realised by the immersion of the samples in nitric acid (HNO_3). The nitric acid was used as a method to effectively p-dope the graphene layer, and also etch away the residual CTAB and PMMA between the Au sphere and film, reducing the gap size between the two. The samples were immersed in 5%, 10%, 20%, 30%, 40%, 50%, 60% and 70% nitric acid for five minutes each. The nitric acid has the effect of p-doping the graphene[49]. Raman spectra were taken of the graphene after each

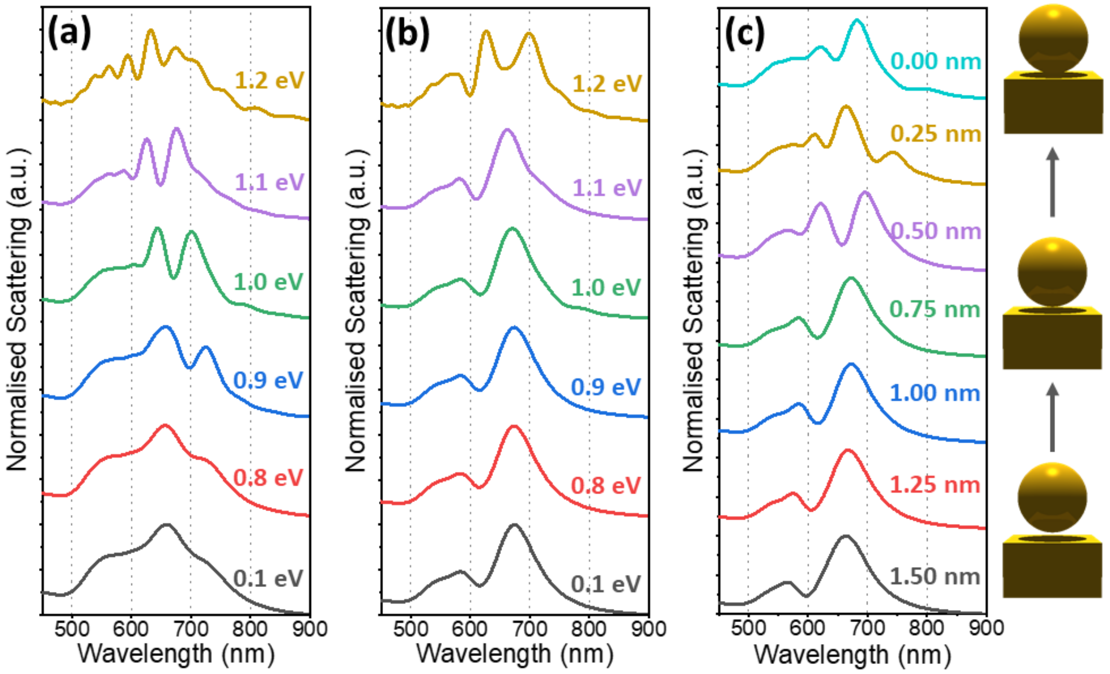

Figure 4.11: (a,b) Simulated scattering spectra for a 150 nm Au sphere on a 100 nm Au film, sandwiching a monolayer of graphene on a SiO_2/Si substrate with a 0.25 nm and a 1 nm gap between the sphere and the graphene, respectively. The chemical potential of the graphene is increased from 0.1 eV to 1.2 eV. (c) Simulated scattering spectra for the same system, without the graphene layer. The gap between the Au film and Au sphere is reduced from 1.5 nm to 0 nm. This effect is illustrated to the right. These simulations are the same as in figures 4.8a and b and figure 4.10a, but with the gap between the sphere and substrate modelled as air instead of PMMA.

---

immersion in the various concentrations of nitric acid. The results are shown in figure 4.2, and can confirm a high level of doping across the entire graphene monolayer[49, 163]. The doping is estimated to be between 0.9 eV and 1.1 eV after being immersed in 70% nitric acid, with slight variations across the graphene sample. This is evidenced by the Raman spectra presented in figure 4.2[155], as well as the experimental spectra shown in figures 4.12 and 4.13.

Dark field scattering spectra were obtained in between each immersion of the sample in nitric acid for all fifty nanospheres measured on each substrate type. Results of sample spectra are shown in figures 4.12 and 4.14. As was seen in figures 4.8 and 4.10, the plasmon modes are highly sensitive to both the gap size and the doping of the graphene layer. Therefore, there was a variety seen in the change of the spectra for the different particles measured. Despite these differences, the overall trends remain constant across all of the experimental spectra.

An example of a 150 nm Au nanosphere on a 100 nm Au film, separated by a monolayer of graphene, is shown in figure 4.12a, with experimentally measured dark field spectra for each concentration of nitric acid up to 70%. Further examples of experimental spectra for each concentration of nitric acid are shown in figure 4.13. As for the simulated results shown in figure 4.8, the largest changes occurred for the dipolar mode.

The dipolar mode is seen to red-shift slightly as the nitric acid concentration is brought from 0% to 20% in figure 4.12a. This is expected, because before the sample is immersed in a high concentration of nitric acid, a lot of residual CTAB and PMMA is still present, resulting in a large gap between the Au sphere and film. Therefore, the first few immersions in nitric acid primarily serve to etch away the PMMA and CTAB in the gap region, reducing the gap size and resulting in the red-shift as shown in figure 4.10a. As the graphene is doped initially with low concentrations of nitric acid, only a slight blue-shift would be expected, not as high as the red-shift evident from the reducing gap size. Further, as demonstrated in figure 4.8a and b, blue-shifts due to the doping of the graphene only occur at high chemical potentials, demonstrating why a blue-shift is only apparent in the experimental spectra when the 30% nitric acid is used. When 0% to 20% nitric acid is used, a very slight red-shift of about 6 nm is shown, indicating that the rate of etching of the PMMA and CTAB layers is having a slightly more dominant effect on the system at these levels than the doping effect of the nitric acid.

A significant blue-shift of 50 nm is shown when the sample is immersed in 30% nitric acid. This indicates that the graphene is now heavily doped, possibly reaching the chemical potential of about 1 eV. As the nitric acid concentration is increased further, from 40% to 70%, the plasmon energy is shown to red-shift slightly again, indicating that the gap is still reducing in size. Another interesting effect is that the dipolar mode has begun to split into two peaks, as shown in figure 4.8. This indicates that the chemical potential has been brought up to about 1.1 eV.

The same system was simulated as shown in figure 4.12b, with the chemical potential being increased from 0.1 eV to 1.1 eV and the gap size being reduced from 1 nm to 0 nm. The simulations show the same trend as the experiments, with the doping level and gap size chosen to match as close as possible to the experiments. The doping level was increased from 0.1 eV to 1.1 eV in the first five spectra shown, matching the trend in the experiments from 0% to 30% nitric acid. The simulated gap size was then reduced from 1 nm to 0 nm for the remaining spectra, matching the 30% to 70% nitric acid spectra in the experiments. There is a slight discrepancy in the energy of the dipolar mode, the simulations predicting

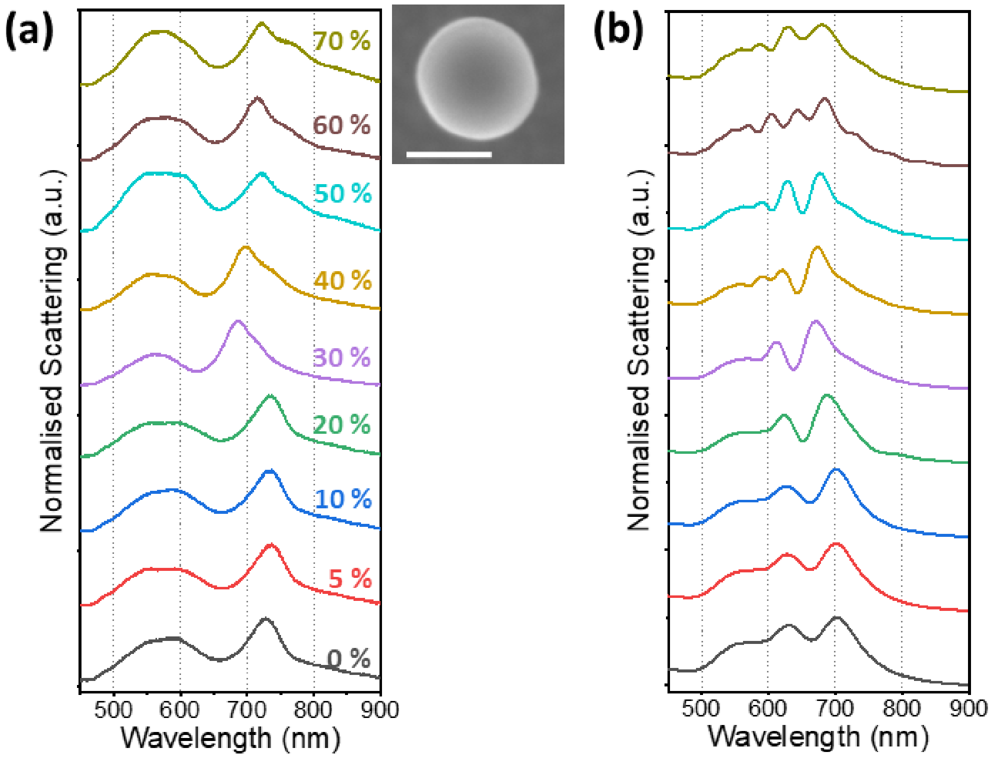

Figure 4.12: (a) Experimental and (b) simulated scattering spectra of the same nanosphere after being immersed for five minutes in nitric acid of increasing concentrations. The 150 nm Au nanosphere is on top of a monolayer of graphene on a 100 nm Au film. A SEM image of the nanosphere is shown to the right of (a), with the white scale bar showing 100 nm.

---

it to have a higher energy. The other difference between the simulations and experiments is that the gap change and doping level appear to have a larger effect on the quadrupolar mode in the simulations than they do in the experimental data. Many factors could contribute to this slight discrepancy between experiments and simulations. These include the uniformity of the permittivity between the nanoparticles and graphene or the quality of the graphene layer itself.

Figure 4.14a shows an example of another Au sphere on a 100 nm Au film, this time without the monolayer of graphene in between. Further examples of experimental spectra for each concentration of nitric acid are shown in figure 4.15. The plasmon energies are again seen to shift due to the change in the gap region. The changes in the gap region are due to the etching of the CTAB layer between the nanoparicle and film, and subsequent reduction of the gap size. The peaks red-shift slightly as the nitric acid concentration is increased to 30%. The positions of the peaks indicate that the gap size is very small before the sample is immersed in nitric acid, especially the dipolar peak at $\approx$ 780 nm. The dipolar peak is very

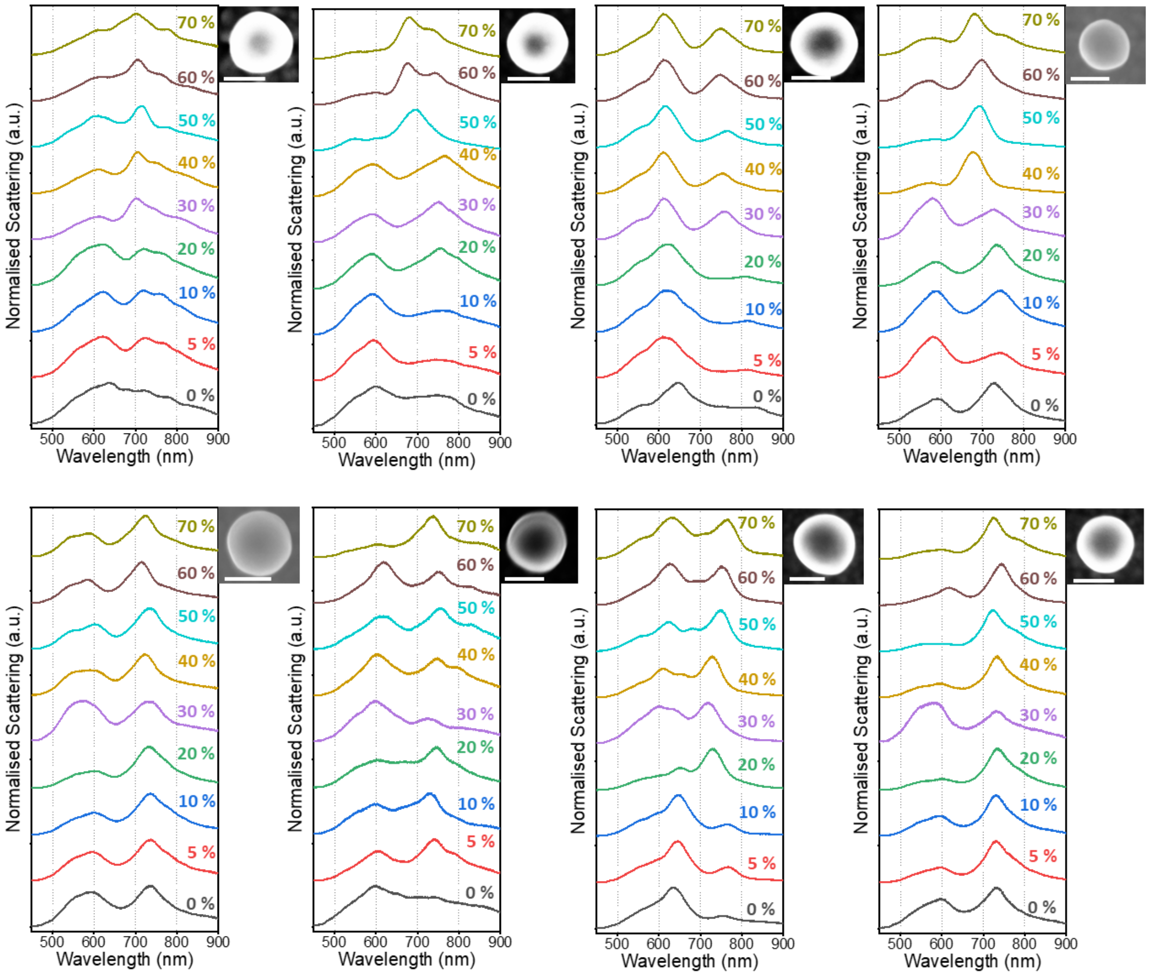

Figure 4.13: Experimental spectra of 150 nm Au spheres on a 100 nm Au film with an intermediate layer of graphene. Spectra are taken after immersing the sample in 0-70% nitric acid, as in figure 4.12. Corresponding SEM images are shown to the right of each spectra. Scale bars show 100 nm. The scattering peaks are shown to blue-shift due to the doping of the graphene layer (especially the dipolar mode), before red-shifting again as the gap size decreases. The dipolar mode is shown to split into two peaks.

---

diffuse with a low intensity when there is a small gap, as demonstrated in figure 4.10a. The reason for this very small gap is because the sample was immersed in acetone heated to 45°C before the measurements were taken. This removed a lot of the CTAB around the particles. The other reason is that there was no PMMA coating the Au film as there is coating the graphene, which helps to keep the gap small. As the nitric acid concentration is increased to 70%, the multipolar modes disappear, giving rise to one single plasmon mode, as shown in figure 4.10b. This is a clear indication that a neck is forming between the Au sphere and film, aided by the immersion in the nitric acid. The plasmon is shown to blue-shift with each immersion from 40% to 70%, indicating that the neck is increasing in diameter as the nitric acid concentration increases. This could be due to the nitric acid removing more CTAB with each immersion, freeing more Au atoms on the lower side of the nanosphere to rearrange and fuse with the Au film underneath.

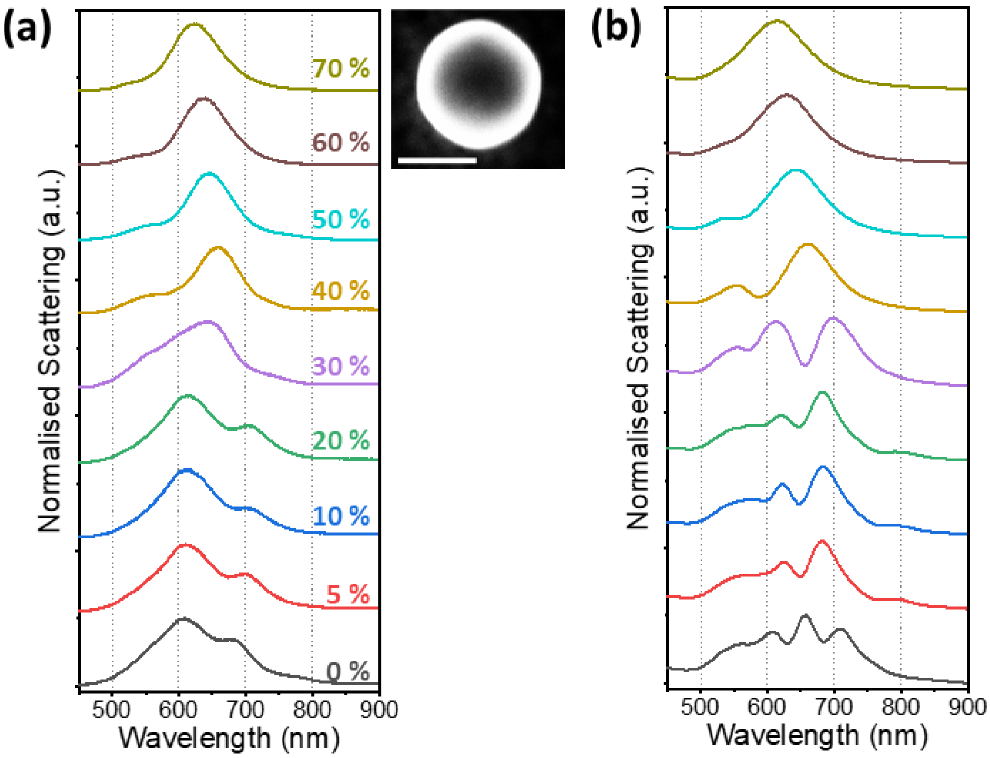

Figure 4.14: (a) Experimental and (b) simulated scattering spectra of the same nanosphere after being immersed for five minutes in nitric acid of increasing concentrations. The 150 nm Au nanosphere is directly on top of the 100 nm Au film. An SEM image of the nanosphere is shown to the right of (a), with the white scale bar showing 100 nm.

The scattering spectra for this system were also approximated with simulations. As the nitric acid concentration was increased to 20%, simulations were carried out with a gap size reduced from 0.3 nm to 0 nm. As the nitric acid concentration was increased further to 70%, the neck radius was increased from 0 % to 50% of the radius of the sphere's diameter. It can be seen in both the experimental and simulated results that as the gap decreases, the plasmons red-shift. After the sphere comes into contact with the Au film, the plasmons start to blue-shift again as the neck increases in diameter. This blue-shift is due to a reduced capacitance as the neck becomes more substantial, allowing more charge to tunnel through. The experiment and simulation show very similar results as the nitric acid concentration reaches 40%, giving good predictions as to how thick the neck becomes after the treatment with nitric acid. Most of the nanospheres measures showed evidence of a neck being formed

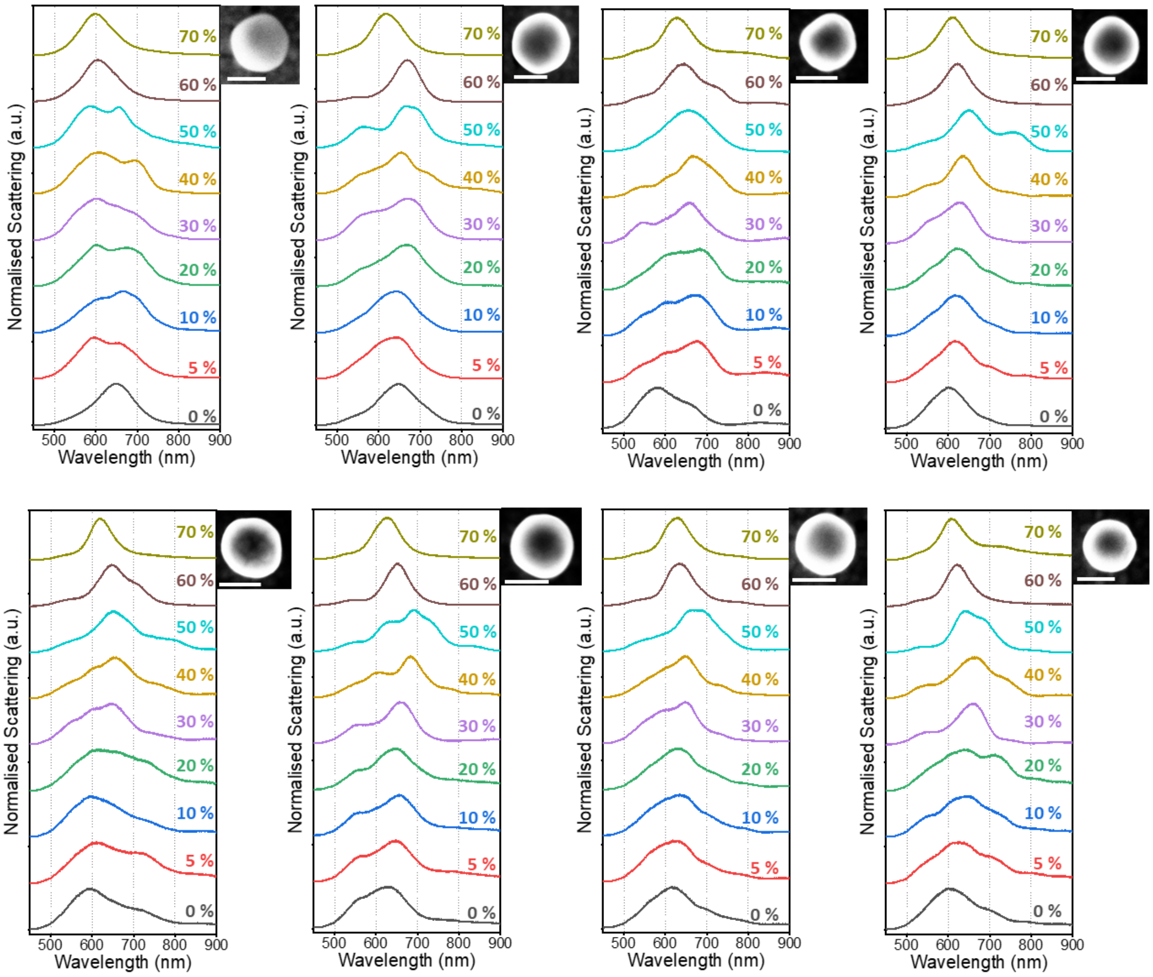

Figure 4.15: Experimental spectra of 150 nm Au spheres placed directly on a 100 nm Au film, with no intermediate layer of graphene. Spectra are taken after immersing the sample in 0-70% nitric acid, as in figure 4.14a. Corresponding SEM images are shown to the right of each spectra. Scale bars show 100 nm. The peaks are shown to red-shift as the gap decreases before blue-shifting again, collapsing into a single, blue-shifted peak as the neck between the nanosphere and film forms.

---

with diameter 40% to 60% of the diameter of the nanosphere.

Experimental scattering spectra for a 150 nm nanosphere on a SiO_2/Si substrate, with and without a graphene layer in between, immersed in 0 to 70% nitric acid as in figures 4.12 and 4.14 are shown in figures 4.16a and b, respectively. No changes in these spectra are detected after treating the samples with nitric acid. This is due to the absence of the Au film underneath the nanoparticles, and therefore, the absence of the high electric field confined within the small gap. This confirms that the shifts observed with the Au film underneath are only possible when the electric field is confined in the small volume between the Au sphere and film. Simulations were also carried out to confirm that no changes took place in the scattering spectrum of a Au nanosphere directly on the SiO_2/Si substrate when the gap distance or doping level was changed.

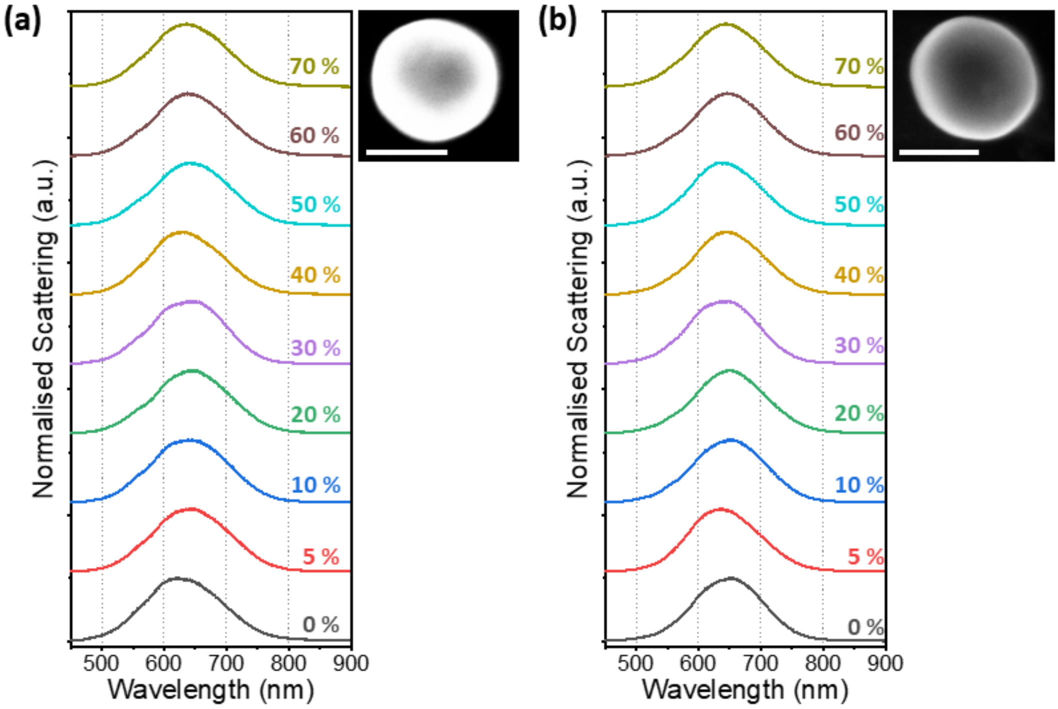

Figure 4.16: Experimental scattering spectra of the same nanosphere after being immersed for five minutes in nitric acid of increasing concentrations. The 150 nm Au nanosphere is on top of a monolayer of graphene on the SiO_2/Si substrate (a) with and (b) without an intermediate monolayer of graphene in between. A SEM image of the nanospheres are shown to the right of the corresponding spectra, with the white scale bars showing 100 nm.

4.6 The splitting of the Dipolar Mode for high Doping Levels

We have seen that the peaks in the scattering spectra of the nanoparticle-on-mirror system correspond to the multipolar modes as described in Shao *et al.*[39]. However, we have not yet examined the theory given by Mertens *et al.*[40], theorising that the two lower energy peaks are due to the charge-transfer plasmon (P_{CTP}) and the gap plasmon (P_{GAP}) interacting. The charge-transfer plasmon is the dipolar resonance of the whole system. The gap is conductive, and gives rise to an equal and opposite charge in the Au sphere and the Au mirror film, as demonstrated in figure 4.6b-d. The gap plasmon is highly localised in the vicinity of the gap, and is therefore more dependent on the doping of the graphene layer. The two plasmons interact as follows:

$$P_+ = P_{CTP} + P_{GAP} \tag{4.5}$$

$$P_- = P_{CTP} - P_{GAP} \tag{4.6}$$

As the doping gets larger, P_{GAP} increases, causing the dipolar mode to split into two new modes, P_+ and P_-. This is supported by both experimental results and simulations (see figures 4.8 and 4.12). For smaller gaps, the quadrupolar and octupolar modes are also seen to split by the same mechanism (see figure 4.8a).

Further simulations were carried out to ensure the surface charge distribution matched this theory. A 150 nm sphere on a Au film, separated by a monolayer of graphene with chemical potential 1.2 eV was simulated, with a gap of 1 nm between the sphere and graphene layer as in figure 4.8b. The surface charge distribution was investigated at the wavelengths of the peaks shown in the scattering spectrum, at (a) 673 nm, (b) 629 nm, (c) 590 nm and (d) 558 nm. The results are shown in figure 4.17. The peaks at (c) 590 nm and (d) 558 nm show the quadrupolar and octupolar modes, as expected, matching the maps shown in figure 4.6. Interestingly, the peak at (a) 673 also appears octupolar when viewing the surface charge distribution at the surface of the Au film, despite being lower in energy to the peak at (b) 629 nm, which is clearly dipolar. These results indicate that the dipolar plasmon has split into two new plasmons, P_+ and P_-[40, 164, 165].

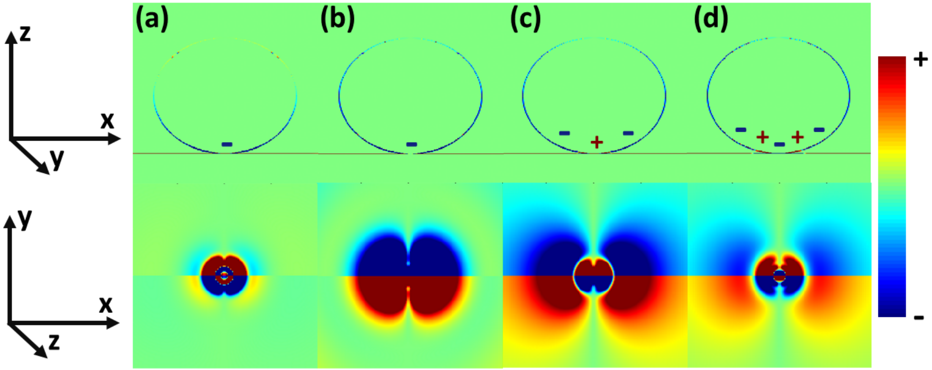

Figure 4.17: Surface charge distribution maps positioned through the nanosphere and the substrate (top panel) and positioned at the surface of the Au film, directly underneath the nanosphere (bottom panel). The gap between the sphere and graphene layer is 1 nm, and the graphene is doped with chemical potential 1.2 eV, as in figure 4.8b. The maps correspond to the position of the peaks at (a) 673 nm, (b) 629 nm, (c) 590 nm and (d) 558 nm. The cross section of each map is 200 nm × 200 nm.

P_- occurs as a result of P_{CTP} and P_{GAP} acting in opposite directions. This has the effect of reducing the energy of the plasmon, and also distorting the surface charge distribution. This gives it the appearance of an octupolar mode, despite being lower in energy. P_+ occurs as a result of P_{CTP} and P_{GAP} acting in the same direction. This has the effect of enhancing the dipolar effect, and also increasing the plasmon energy.

4.7 Conclusion

A single Au nanoparticle on a Au mirror film separated by a monolayer of graphene has been investigated. It has been demonstrated with both numerical simulations and experimental results how sensitive the plasmon modes are to both the gap size and the level of doping in the graphene layer, even at visible wavelengths. The coupling of the nanosphere and film gives rise to multipolar modes which can be tuned to blue-shift by doping a monolayer of graphene in between them, or by altering the gap size. At high doping levels, the plasmons are seen to split into two new energy levels. The results serve to explain how different theories in the two previous papers, Shao *et al.* and Mertens *et al.*, are both correct under different levels of doping and different gap sizes. These results will be useful for the design and fabrication of future devices employing the use of a nanoparticle-on-mirror system, separated by a 2D material. They give a deeper understanding of the interactions between the different plasmonic modes and how they can be controlled. The control of the energy of plasmonic modes as shown in this chapter has potential applications in sensing in the visible region.

> Look deep into nature, and then you
> will understand everything better.
>
> Albert Einstein

5 Rabi splitting between Plasmons of Gold Nano-Bipyramids and the Excitons of Monolayer MoS_2

5.1 Introduction

The longitudinal plasmon (oscillation of electrons along the long axis) of a Au nano-bipyramid is an ideal resonance for strong coupling. The plasmonic resonance is sharper than other, similar structures such as nanorods[119]. More importantly, however, the tunable, sharp tips provide the ideal platform for reducing the mode volume of the resonator. This is because the electric field enhancement is confined mostly in the tips, even for larger bipyramids. As described in section 2.4.2, a low mode volume results in a higher coupling strength for Rabi splitting. This is because $g \propto \frac{1}{\sqrt{V}}$, where g is the coupling strength and V is the mode volume of the resonator, as described in equation 2.15. They adapt a reduced-symmetry configuration on a substrate, only one of their ten sides touching the surface[52]. This further reduces the mode volume of the resonance with only one sharp tip interacting with the quantum emitter. An even more important effect of this reduced symmetry is that the plasmon oscillation is tilted towards the MoS_2. In other similar systems using different nanoparticle shapes, the plasmon oscillation is in parallel to the substrate, causing the electric field hot spots to be misaligned with the dipole moment of the exciton underneath. This misalignment can greatly reduce the strength of the Rabi splitting[52].

MoS_2 was chosen to couple with the bipyramids of this system due to the lower temperatures required for its synthesis[122] as well as its A exciton energy being in the visible range[15, 134]. Chemical vapour deposition (CVD) is the preferred method for obtaining monolayer MoS_2. This is due to the large monolayer area coverage of single flakes as well as the higher crystallinity and larger flake size compared with what can be obtained by other methods[123, 166].

In this system, the strong coupling between the longitudinal plasmon of a Au bipyramid and the A exciton of a monolayer of MoS_2 on a 300 nm SiO_2 on Si substrate is investigated. All experiments and simulations were carried out at room temperature and atmospheric pres-

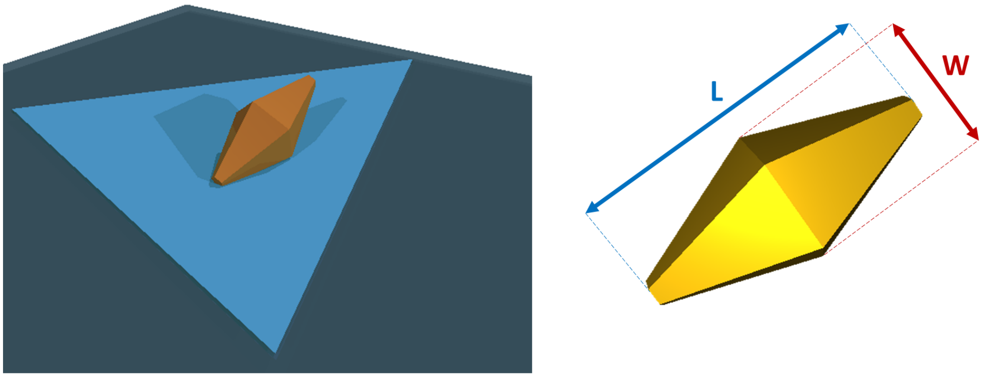

Figure 5.1: Schematic of the system, with a single Au nano-bipyramid drop-cast on a monolayer of MoS_2 on top of a 300 nm SiO_2 on Si substrate. A single bipyramid is also shown with its length and width marked as L and W, respectively.

---

sure. All measurements, both in experiments and in simulations, were carried out at the single particle level. A schematic of the system is shown in figure 5.1.

5.2 The Interaction between Gold Bipyramids and Monolayer MoS_2

Bipyramids have two plasmons, a longitudinal and a transverse. These are the oscillations of electrons along the longitudinal axis (L as shown in figure 5.1) and the transverse axis (W as shown in figure 5.1). In the transverse case, the scattering is much weaker. Additionally, the transverse peaks have a higher energy, at about 2.5 eV for the bipyramids studied. This is much higher than the energy of the A exciton of monolayer MoS_2, making any interaction with it negligible. Therefore, only the longitudinal plasmon of the Au bipyramids were considered in this investigation.

As previously discussed in section 2.4.2, the longitudinal plasmon of the Au bipyramid and the exciton of the monolayer of MoS_2 couple together to achieve Rabi splitting. The bipyramids are grown with a size and shape to give a plasmon that overlaps with the energy of the A exciton of monolayer MoS_2. This energy was found by taking the photoluminescence of the MoS_2 flakes (figure 3.11b in section 3.4.2). Raman spectroscopy was also carried out to ensure all of the MoS_2 flakes investigated were monolayer (see figure 3.11). Rabi splitting is also possible with few-layered transition metal dichalcogenides[52], but to keep the MoS_2 consistent, only the monolayer flakes were considered for this work.

A wide variety of plasmon energies are possible when tuning the size and shape of the bipyramids. This is shown in figure 5.2, where the scattering spectra of single bipyramids are shown with their corresponding SEM images. Figure 5.2a shows bipyramids of length

100 nm and figure 5.2b shows bipyramids of length 80 nm. This highlights how the size of a bipyramid influences the energy of the plasmon. Smaller bipyramids are shown to have a higher plasmon energy. The plasmon energy can also be controlled with the aspect ratio (ratio of length, L, to width, W) of a bipyramid, or by changing the radius of the tips on either side of the bipyramid. This is shown in figure 5.2, as even bipyramids of the same length have different plasmon energies when the aspect ratio or tip radii are changed. A lower aspect ratio reduced the plasmon energy. Sharp tips were also seen to lower the plasmon energy. Sharp tips, however, are important for the bipyramids as the sharp tips increase the local field confinement, strengthening the Rabi splitting.

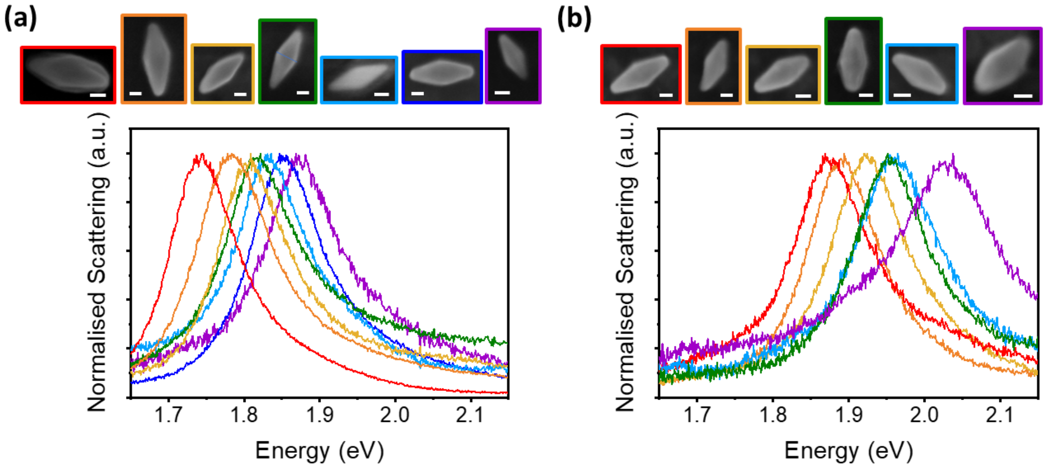

Figure 5.2: Single particle scattering spectra for bipyramids drop-cast directly onto the 300 nm SiO_2 and Si substrate for bipyramids of length (a) 100 nm and (b) 80 nm. White scale bars show 20 nm.

Figure 5.3 shows the scattering spectra of two different single bipyramids and their corresponding SEM images. Both bipyramids are a similar size and shape, but are drop-cast onto different substrates. The bipyramid in figure 5.3a is drop-cast onto a plain substrate of 300 nm SiO_2 on Si. This bipyramid shows a single peak in the scattering spectrum corresponding to the longitudinal plasmon energy. The bipyramid in figure 5.3b is drop-cast onto a single monolayer of MoS_2 on top of the same substrate as in figure 5.3a. For this bipyramid, the scattering spectra for both the longitudinal and transverse polarisations were taken. The longitudinal measurement shows two distinct peaks, characteristic of Rabi splitting. The measurement indicates that the plasmon has split into two new eigenstates. The transverse measurement was also taken to confirm that both peaks were present due to the single longitudinal plasmon interacting with the exciton. No features were visible in the transverse case, giving a further indication of Rabi splitting. A very small longitudinal signal is still present in the transverse measurement of figure 5.3b due to a slight offset of the polariser in the experimental set-up.

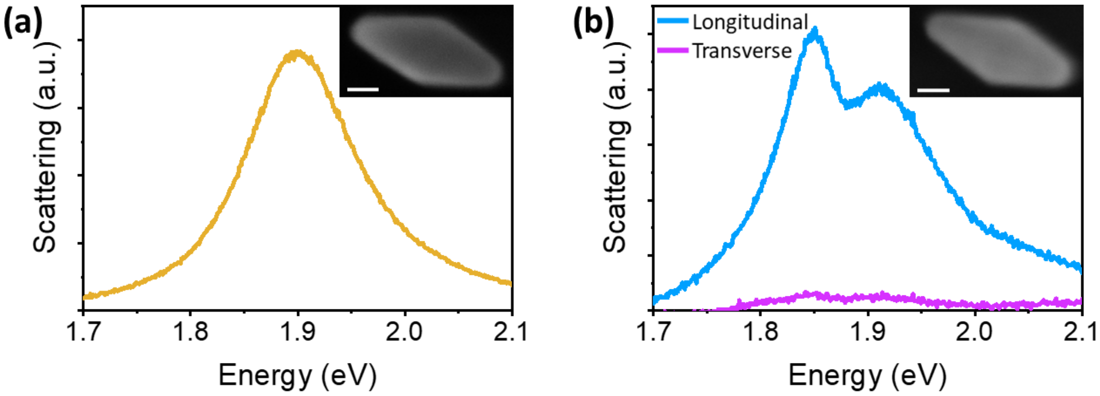

Figure 5.3: Single particle scattering spectra for a bipyramid on (a) the SiO_2/Si substrate and (b) the MoS_2 monolayer on the SiO_2/Si substrate. Light polarised in both the longitudinal and transverse directions is shown in (b). Insets show corresponding SEM images. The white scale bars show 20 nm.

As shown in figure 5.2, the plasmon energy of the single bipyramids can be controlled by changing the length and aspect ratio. This can be done to detune the plasmon energy from the exciton energy. The photoluminescence peak for the monolayer MoS_2 monolayer on the SiO_2/Si substrate was measured at about 1.88 eV, corresponding to the energy of the A exciton. The effect of detuning the plasmon energy from the energy of the A exciton of monolayer MoS_2 is shown in figure 5.4a. The bipyramids were detuned by changing the length and keeping the aspect ratio constant. As discussed previously, smaller bipyramids have higher energy plasmons, while larger bipyramids have lower energy plasmons. When the plasmon energy is higher than the exciton energy, there is more scattering from the upper polariton. Similarly, when the plasmon energy is lower than the exciton energy, there is more scattering from the lower polariton.

As discussed in section 2.4.2, it is possible for splitting to occur in the scattering spectrum due to a Fano-like interference causing an anti-resonance. This occurs when the rate of exchange of energy from the exciton to the plasmon is quicker than the decay rate of the exciton, but the rate of exchange of energy from the plasmon back to the exciton is slower than the decay rate of the plasmon. The feedback from the exciton to the plasmon can cause a dip in the scattering spectrum of the plasmonic response, but the lack of feedback from the coupling of the plasmon back to the exciton is revealed by the absence of splitting in the emission spectrum of the exciton[98]. The two peaks in the PL spectrum could be used to confirm Rabi splitting because the PL directly measures the excitons in the system. This

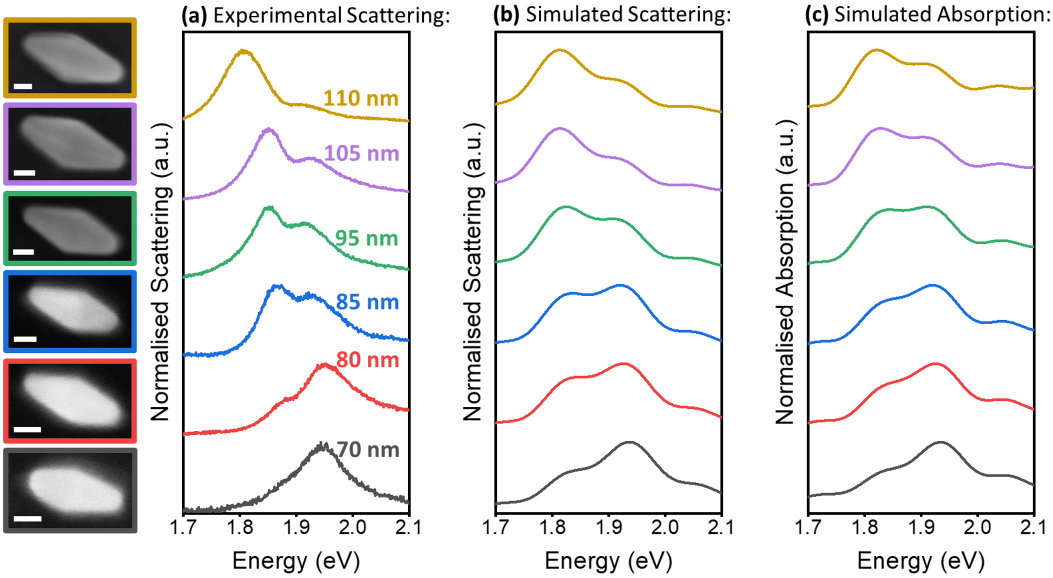

Figure 5.4: (a) Single particle scattering spectra for single bipyramids of varying lengths and of aspect ratio ≈ 2.3 on a monolayer of MoS_2 on an SiO_2/Si substrate. Corresponding SEM images for each bipyramid are shown to the left. The white scale bars show 20 nm. (b) FDTD simulations showing the scattering spectra of the same Au bipyramids as in (a). (c) FDTD simulations showing the absorption spectra of the same Au bipyramids as in (a).

---

is difficult to achieve experimentally due to the large sheet of MoS_2, with a large number of uncoupled excitons, surrounding each bipyramid. This means that it would be difficult to observe the PL signal of a split A exciton emission peak from the area of MoS_2 directly underneath the bipyramid tip when the much greater area of surrounding MoS_2 is emitting one, uncoupled peak.

FDTD simulations were used to confirm that Rabi splitting was taking place. The experimental scattering results were reproduced with FDTD simulations as shown in figure 5.4b. There is a strong agreement between the simulations and the experiment. FDTD simulations were taken further to calculate the absorption spectra (figure 5.4c). The dip in the absorption spectra confirms that Rabi splitting was achieved between the plasmons and excitons of the system, as Fano resonances do not show a dip in the absorption of the system[98].

There are slight differences between the experimental and simulated scattering spectra. There is an extra peak at about 2.05 eV present in the simulated data. This is attributed to the presence of the B exciton. The refractive index used to model the MoS_2 was taken from Jung *et al.*[67] (figure 2.7), and differed slightly from the experimental MoS_2, having a stronger B exciton. Further simulations were performed using the 85 nm Au bipyramid in figure 5.4. The scattering and absorption results of these simulations are shown in figures 5.5a and b, respectively. In these simulations, three different refractive indexes were used to model the MoS_2. These were the refractive index in figure 2.7, a refractive index with Lorentzian functions matching the peaks corresponding to the A exciton and a refractive index with Lorentzian functions matching the peaks corresponding to the B exciton. The results show that when MoS_2 is modelled with only the A exciton, there is no extra scattering peak at 2.05 eV. When it is modelled with only the B exciton, the peak at 2.05 eV is present, but there is no Rabi splitting from the absent A exciton.

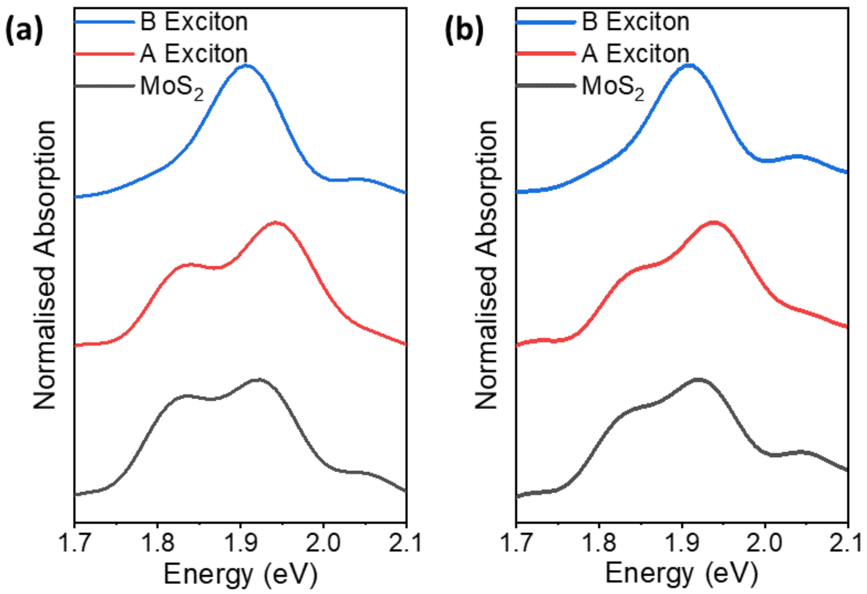

Figure 5.5: (a) Scattering and (b) absorption spectra for an 85 nm long bipyramid with aspect ratio 2.3 on MoS_2 on an SiO_2/Si substrate. The MoS_2 is modelled with the refractive index from Jung *et al.*[67] (black), with only the A exciton (red) and with only the B exciton (blue).

The simulated scattering spectra are also shown to have slightly broader peaks. This is also due to the refractive index used for the simulation being slightly different to the experiment. When the refractive index is altered to have a higher amplitude for the excitonic peaks, the simulated peaks in the scattering spectrum narrow.

Scattering spectra were measured for a few hundred bipyramids of different lengths and aspect ratios. The scattering spectrum of each particle was correlated with its SEM image, revealing its size and shape. The bipyramids measured were then split into four different size categories, of lengths 60-75 nm, 76-85 nm, 86-95 nm, and 96-115 nm. Bipyramids from each size category were measured from different substrates to ensure any differences found were due to the differently sized bipyramids instead of a difference between the MoS_2 flakes between different samples. Bipyramids with a wide variety of aspect ratios were also used within each category, giving a range of plasmon energies for each size of bipyramid used.

The energy of the two new polaritons were plotted against the energy of the original uncoupled plasmon for each bipyramid measured. Separate plots were made for each size category, as shown in figure 5.6. The energy of the PL peak varied by about 0.02 eV for different MoS_2 flakes measured on different samples. To account for this when comparing the energies of the plasmons and polaritons, everything was plotted in terms of detuning from the energy of the A exciton of MoS_2. Clear anticrossing behaviour, characteristic of Rabi splitting, is visible in each plot. This shows the energy of the two new polariton peaks splitting above and below the energy of the original, uncoupled plasmon and exciton.

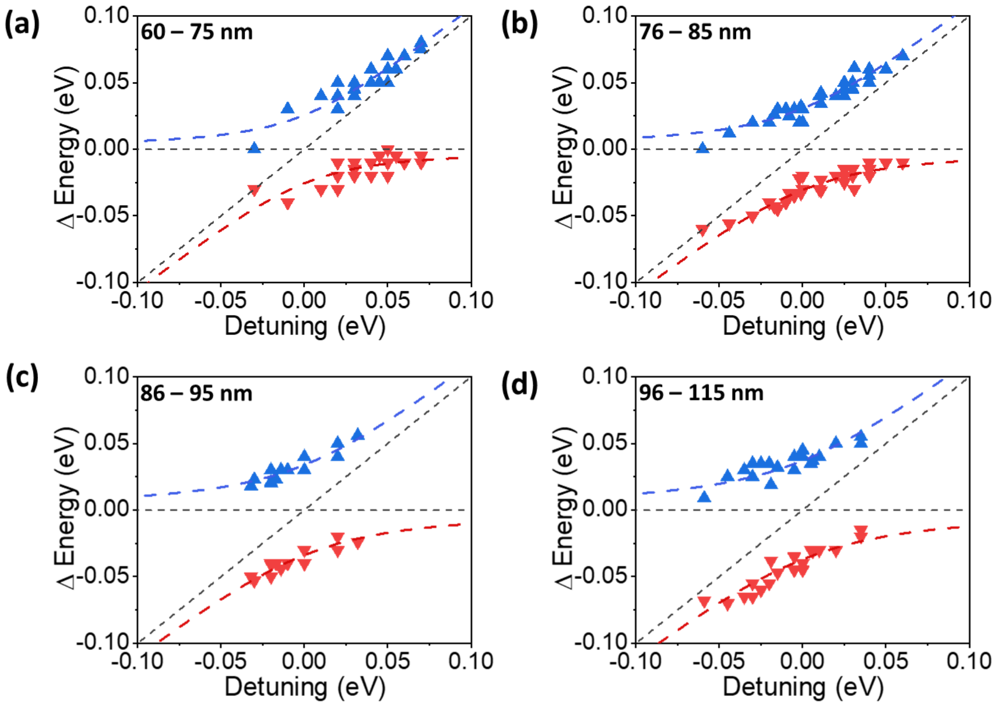

Figure 5.6: Anti-crossing plots for single Au bipyramids coupled to MoS_2 showing the energies of the two polaritons plotted against the energy of the original, uncoupled plasmon. The energy is plotted in terms of detuning from the energy of the A exciton of monolayer MoS_2. Plots for bipyramids in the length catagories 60-75 nm, 76-85 nm, 86-95 nm, and 96-115 nm are shown in (a), (b), (c) and (d), respectively. The black horizontal and diagonal dashed lines show the energy of the A exciton in MoS_2 and plasmon energy of the bipyramids, respectively. The blue triangles show the energy of the upper polariton and the red triangles show the energy of the lower polariton. The dashed blue and red lines show the fit calculated from the coupled oscillator model from equation 5.1

.

Rabi splitting can be modelled as an anti-crossing curve. This means that the resonance energy of the two new polaritons have higher and lower energy than that of the original exciton and plasmon. The energy of the two new polaritons is given by[97]:

$$\omega_{\pm} = \frac{\omega_{pl} + \omega_{ex}}{2} \pm \sqrt{g^2 + \frac{1}{4}\left[\omega_{pl} - \omega_{ex} - \frac{i}{2}(\gamma_{pl} - \gamma_{ex})\right]^2} \tag{5.1}$$

where ω_{pl} and ω_{ex} give the plasmon and exciton energies, g gives the coupling strength and γ_{pl} and γ_{ex} give the plasmon and exciton dissipation rates, respectively.

By subtracting ω_- from ω_+ in the case where the plasmon and exciton overlap in energy ($\omega_{ex} = \omega_{pl}$), it is clear to see that a higher coupling constant, g gives a stronger energy splitting of the two polaritons:

$$\Omega = \omega_+ - \omega_- = \sqrt{4g^2 - \frac{(\gamma_{pl} - \gamma_{ex})^2}{4}} \tag{5.2}$$

The coupled oscillator model from equation 5.1 was used to fit the data from the dark field scattering measurements. This is shown by the dashed curved lines on the plots in figure 5.6 with the blue and red lines showing the fit of the upper and lower polaritons, respectively. The positions of the uncoupled exciton and plasmon are also indicated by the dashed horizontal and diagonal lines, respectively.

The energies of the upper and lower polaritons (ω_+ and ω_-, respectively) were taken as the highest points in intensity in the center of the polariton peaks of the scattering specra. The PL of the MoS_2 gave the energy of the A exciton (ω_{ex}). The energy of the uncoupled plasmon, ω_{pl}, was calculated as:

$$\omega_{pl} = \omega_+ + \omega_- - \omega_{ex} \tag{5.3}$$

The plasmon dissipation rate (γ_{pl}) was measured as the full-width-half-maximum (FWHM) of the single particle scattering measurements on the SiO_2/Si substrate (figure 5.2). This was confirmed to be constant for all sizes of bipyramid by FDTD simulations, so γ_{pl} was taken as the average of all experimental spectra, as $\approx$ 105 meV. The dissipation rate of the exciton (γ_{ex}) was taken by averaging the FWHM of the PL measurements of the MoS_2 flakes. It was found to be $\approx$ 50 meV.

Equation 5.1 was used to estimate the coupling constant, g. This was done by finding a g such that the average difference in predicted and measured (from the experimental scattering spectra) polariton energies was minimised ($<$ 2 meV) within the sample of bipyramids.

When calculating the energy of the polariton peaks from experimental methods, the results can vary depending on the method used[167]. This can lead to some inaccuracies with the experimental results. The FDTD simulations showed that the difference between the splitting in the scattering spectra and the splitting in the absorption spectra was 7 ± 4% of the splitting in the scattering spectra. The scattering, therefore, shows a higher splitting than the absorption. The coupling strength, g, calculated from the scattering spectra, can then be estimated with a small margin of error of about $\approx 10\%$, according to the simulations.

The plots in figure 5.6 are put together in figure 5.7a. In this plot, it is shown that the polariton energy separation increases for larger bipyramids. Figure 5.7b summarises these results, showing that the coupling strength, g, and the Rabi splitting, Ω, increases for larger bipyramids. The Rabi splitting value is defined as the energy separation between the two polaritons when there is zero detuning between the plasmon and exciton. It is calculated by equation 5.2.

In figure 5.7b, the coupling strength is shown to increase from about 25 to 40 meV, and the Rabi splitting strength is shown to increase from about 50 to 80 meV when the bipyramid size changed from 70 to 100 nm. This effect is also visible in figure 5.4, where the splitting is shown to be stronger for the larger bipyramids.

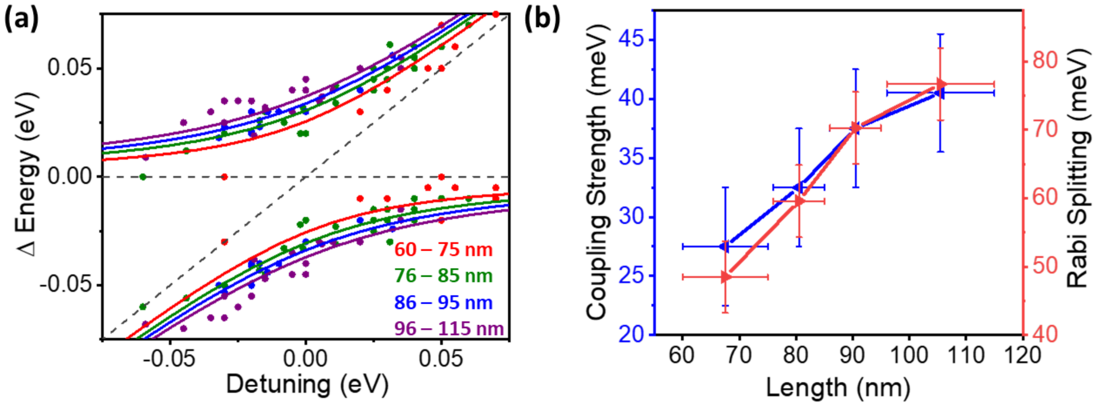

Figure 5.7: (a) Anti-crossing plot for single Au bipyramids coupled to MoS_2 showing the energies of the two polaritons plotted against the energy of the original, uncoupled plasmon. The energy is plotted in terms of detuning from the energy of the A exciton of monolayer MoS_2. Bipyramids in different length catagories are shown in different colours. The black horizontal and diagonal dashed lines show the energy of the A exciton in MoS_2 and plasmon energy of the bipyramids, respectively. (b) All experimental data compiled together to show the coupling strength and Rabi splitting of the differently sized bipyramids coupled to the MoS_2.

Several reports indicate different criteria for the coupling strength to achieve Rabi splitting. These include $g > \gamma_{pl}, \gamma_{ex}$[102, 96], $g > \sqrt{\gamma_{pl}\gamma_{ex}}$[102] and $g > \frac{\gamma_{pl}+\gamma_{ex}}{2}$[52, 96, 108]. In this work, Ω ranges from 50 to 80 meV, and γ_{pl} and γ_{ex} are 105 meV and 50 meV, respectively. Therefore, only the bipyramids above 90 nm in length meet these requirements. This is primarily due to the broad linewidth of the plasmon resonances.

Despite this, other evidence suggests that strong coupling is occurring for all bipyramid sizes investigated. The FWHM was measured across the two peaks in the scattering spectrum for bipyramids over a range of sizes coupled to the MoS_2. There was $\approx$ zero detuning between the plasmon and exciton energy for each of the FWHM measured. The average FWHM across both peaks was found to be ≈ 150 meV. This is significantly larger than the FWHM across the single scattering peak found for bipyramids drop-cast directly onto the SiO_2/Si substrate, which was found to be ≈ 105 meV. These results indicate that more than just an interference effect is taking place, with the two new polariton peaks being spaced further apart. This effect is visible in figure 5.3. The simulated absorption spectra also support that Rabi splitting is occurring (figure 5.4). It is therefore possible that g is underestimated for the experimental measurements. Further work could be done to confirm this. Altering the slit width of the spectrometer used to measure the scattering light when measuring the FWHM of the PL and scattering spectrum of an uncoupled plasmon could give more accurate representations of the decay rates of the plasmon and exciton.

As the lengths of the bipyramids were increased, so did the overall metal volume. A longer length resulted in a necessary reduction in aspect ratio to keep the plasmon energy overlapping with the exciton energy. This further added to the effect of the metal volume increasing for larger bipyramids. Therefore, the coupling strength is seen to increase with the overall metal volume. These results are in contrast to previous studies which found that an increased metal volume reduced the coupling strength[66, 102]. This indicates that a different mechanism is occurring for Rabi splitting achieved with a bipyramid-shaped nanoparticle.

5.3 Electric Field Enhancement at the Tip of the Bipyramids

FDTD simulations were carried out to confirm the trend of larger bipyramids resulting in a larger coupling strength (figure 5.8a), with the bipyramid's length being varied from 70 to 110 nm. For a clearer comparison, a lower aspect ratio was used for the larger bipyramids so that the plasmon energy directly overlapped with the exciton energy. The tip radius was kept constant at 7 nm for each simulation. The trend clearly showed a larger Rabi splitting strength for the larger bipyramids, in agreement with the experimental data. Similarly, the effect of the tip radius on the coupling strength was investigated with FDTD simulations (figure 5.8a). For these simulations, the bipyramid length was fixed at 80 nm, the tip radius was adjusted from 4 to 12 nm and the aspect ratio was adjusted to ensure the plasmon's energy was overlapped with the exciton. These simulations clearly show that the Rabi splitting is stronger for bipyramids with a lower tip radius.

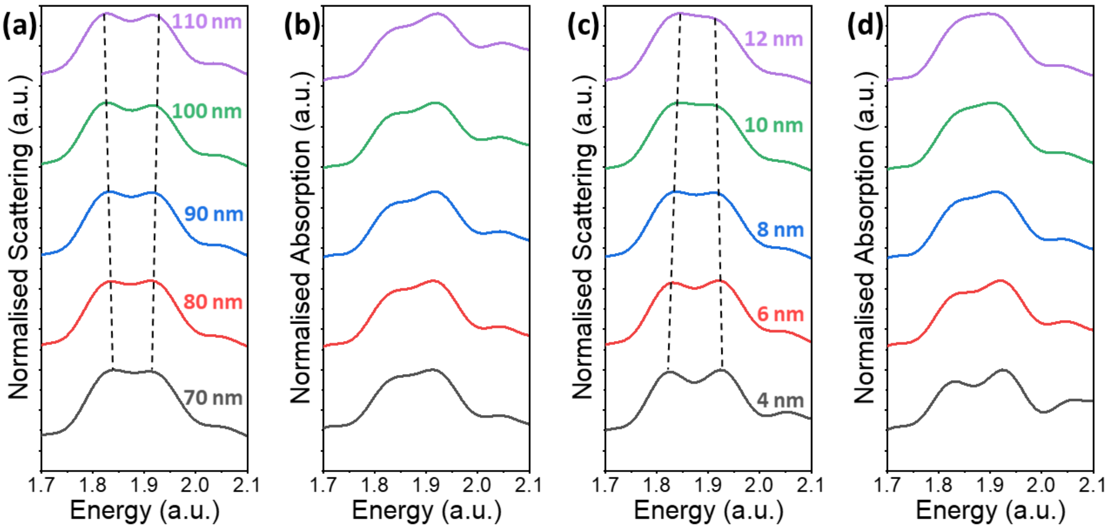

Figure 5.8: (a) Scattering and (b) absorption spectra for bipyramids coupled to MoS_2 with lengths varied from 70 to 110 nm. The tip radii were kept constant at 7 nm. (c) Scattering and (d) absorption spectra for bipyramids coupled to MoS_2 with tip radii varied from 4 to 12 nm. The length was kept constant at 80 nm. In all simulations, the aspect ratio was adjusted to keep the plasmon's energy overlapping with that of the exciton.

The FDTD simulations were examined further to investigate why the larger bipyramids were had a stronger coupling strength with the MoS_2. Electric field maps, plotted in V/m, are shown for an 85 nm bipyramid coupled to an MoS_2 monolayer (figure 5.9a and b). Figure 5.9a shows the electric field map through the bipyramid, perpendicular to the substrate. Figure 5.9b is positioned within the MoS_2 layer underneath the bipyramid and is perpendicular to figure 5.9a. The purple dashed line in figure 5.9a indicates the position of figure 5.9b and vice versa. Both maps show the electric field strength at the frequency of maximum electric field enhancement of an 85 nm bipyramid, of aspect ratio 2.3 and tip radius 7 nm, on a monolayer MoS_2 layer. The electric field enhancement is clearly confined at the tip of the bipyramid that is in contact with the MoS_2.

The maximum electric field strength at the tip of the bipyramid in contact with the MoS_2 for a variety of bipyramid sizes is shown in figure 5.9c. The maximum electric field strength (in V/m) was taken at the wavelength of the maximum field enhancement, which was at the energy of the A exciton of the MoS_2. The blue line shows the maximum electric field strength at the tips of the bipyramids simulated in figure 5.8a and b. In these bipyramids, the tip radius is kept constant, and the aspect ratio is altered to the plasmon is kept in tune with the exciton for all lengths considered. The overall trend is that the electric field strength

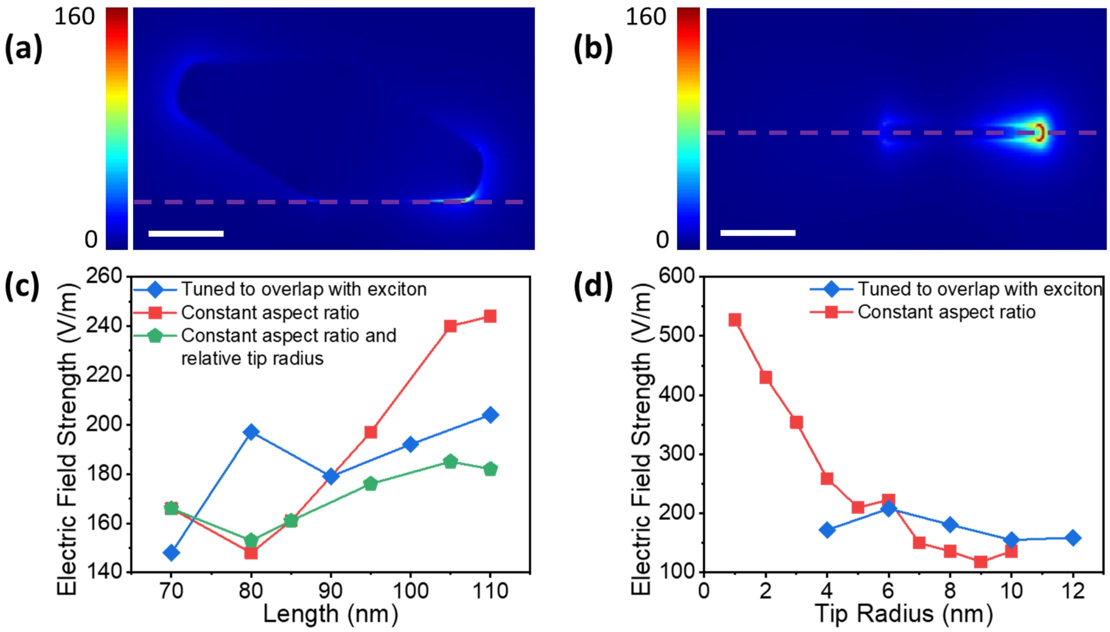

Figure 5.9: (a) and (b) show typical electric field strength maps in V/m, cutting through the bipyramid perpendicular to the surface and within the MoS_2 layer underneath the bipyramid, respectively. The purple dashed line in (c) shows the position of the perpendicular slice shown in (d) and vice versa. The white scale bars show 20 nm. (c) Plot of the maximum electric field strength (V/m) at the tip of different bipyramids with varying length between 70 and 110 nm. The blue plot corresponds to the bipyramids presented in figure 5.8a and b with the aspect ratio adjusted to keep the plasmon energy overlapping with the exciton. The red plot corresponds to bipyramids with a fixed aspect ratio and a fixed tip radius of 7 nm, as shown in figure 5.4. The green plot corresponds to bipyramids with a fixed tip radius to width ratio and aspect ratio. (d) Plot of the maximum electric field strength (V/m) at the tip of different bipyramids with varying tip radius between 1 and 12 nm. The blue plot corresponds to the bipyramids presented in figure 5.8c and d with the aspect ratio adjusted to keep the plasmon energy overlapping with the exciton. The red plot corresponds to bipyramids with a fixed aspect ratio and a fixed length of 80 nm.

---

increases for longer bipyramids, mirroring the trend of increased Rabi splitting. There is an unexpected drop in electric field strength for the 90 nm bipyramid. This can be attributed to the decreased aspect ratio for the longer bipyramids required to keep the plasmon's energy equal to the energy of the exciton. This caused a blunting effect on the tips and a lower electric field density.

Further simulations were carried out to reduce the blunting effect. The red line in figure 5.9c shows the maximum electric field strength for bipyramids with a constant aspect ratio of 2.3 and constant tip radii of 7 nm. The scattering and absorption spectra for these bipyramids are shown in figure 5.4. In this plot, there is no blunting effect for the larger bipyramids because the aspect ratio is kept constant. Therefore, a much clearer trend is seen than was visible in the blue plot, with the electric field strength increasing for the larger bipyramids. The one exception to this is the shortest, 70 nm long, bipyramid. This is because the highest electric field strength for this bipyramid was at 636 nm, not overlapping with the exciton energy as is the case with the other bipyramids. This is because the plasmon is too detuned from the exciton to follow the trend of the other bipyramids.

Keeping the aspect ratio constant is not the only factor to consider when increasing the length of the bipyramids. In the red line in figure 5.9c, the tip radius was kept constant, meaning that the exact proportions of each bipyramid simulated were not identical. The tip radii were smaller in proportion to the bipyramid as a whole when it was made longer. Further simulations were carried out to investigate the impact of this on the electric field strength. The green line shows bipyramids of varying length with both the tip radii and the aspect ratio adjusted to keep the proportions of the shape constant. The proportions of an 85 nm bipyramid of aspect ratio 2.3 and tip radius 7 nm was chosen for these simulations. The green line shows a similar trend to the red line, with the electric field strength increasing for larger bipyramids. This shows that the increased Rabi splitting strength is due to the increased size of the bipyramid because the electric field strength is enhanced with the bipyramid size. Even when the tip radius in increased to keep the bipyramid shape proportions constant, the electric field strength increases, demonstrating the importance of metal volume on Rabi splitting strength. When the bipyramid reaches 110 nm in length, the electric field strength is shown to decrease again. This is attributed to the large increase in tip radius, reducing the electric field confinement. The electric field strength increases less rapidly for the green line than the red line for the same reason. The electric field enhancement is spread over a larger volume at the larger tip as its radius increases.

The importance of a low tip radius was investigated further with FDTD simulations. Figure 5.9d shows how the maximum electric field strength at the bipyramid tip at the wavelength of maximum enhancement changes for different tip radii. In the blue plot, the length of the bipyramids are fixed at 80 nm, and the aspect ratio is adjusted so the plasmon overlaps in energy with the exciton. A decrease in the electric field is observed for larger tips, as expected. The bipyramid with the 4 nm tip radius has a lower electric field strength than expected, attributed to the low aspect ratio required to blue-shift the plasmon to the correct energy, causing a blunting effect.

The red line in figure 5.9d shows the electric field strength at the tips of bipyramids with varying tip radii, with the length fixed at 80 nm and the aspect ration fixed at 2.3. The tip radii were varied from 1 to 10 nm. The field decreased with a larger tip radius and got very large when the radius was reduced to unfeasibly small sizes. The field for the 6 nm tip radius was higher than expected. Upon further investigation, it was observed that this is the bipyramid with closest to zero detuning between its plasmon and the exciton. It therefore has the strongest interaction with the MoS_2, resulting in a slightly larger electric field strength.

5.4 The Effect of the Bipyramid Tilt on Rabi Splitting Strength

The above results clearly show that the electric field strength at the tips of the bipyramids increases as the bipyramid length increases, and as the bipyramid tip radius is reduced. This gives a good explanation as to why the Rabi splitting strength increases with an increasing metal volume in the bipyramid. However, it must be noted that there are other changes in the system when a larger bipyramid is used which also increase the Rabi splitting strength.

Figure 5.10 elucidates this. Part (a) shows three bipyramids of increasing lengths, and with decreasing aspect ratios to keep the plasmon energy constant. The angle of the tilt of the plasmon is increased from ϕ_1 to ϕ_3 as the aspect ratio is reduced. The bipyramid with the smallest aspect ratio and the largest tilt angle results in a larger overlap of the electric field with the MoS_2. This offers a further explanation of why the Rabi splitting is higher for larger bipyramids. The decreased aspect ratio required for larger bipyramids increases the tilt angle, tilting the plasmon resonance more directly towards the MoS_2.

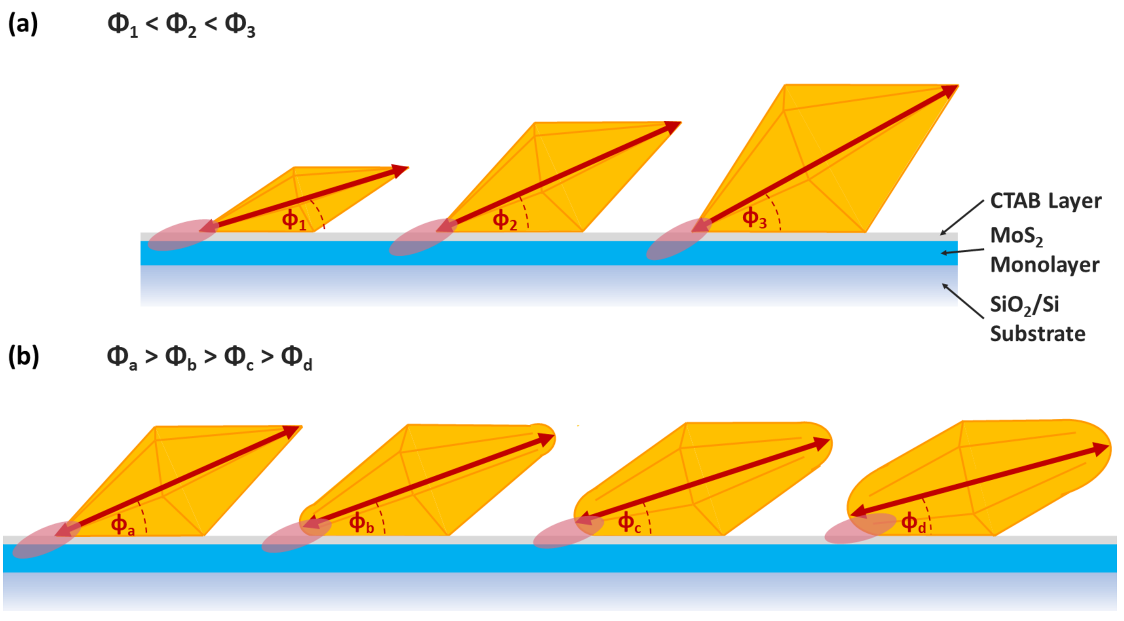

Figure 5.10: (a) The effect on the tilt of the plasmon when a bipyramid's aspect ratio is reduced. (b) The effect on the tilt of a plasmon when a bipyramid's tip radii are increased.

Similarly, part (b) shows four bipyramids of the same length and aspect ratio, but with different tip radii. As the tip radii are increased, the plasmon tilt is reduced from ϕ_a to ϕ_d. This reduces the overlap of the plasmon resonance and the exciton of the MoS_2. Therefore, a larger tip would result in a lower electric field strength, a lower confinement and an increased mode volume, severely reducing the Rabi splitting strength.

Further simulations were carried out to investigate how the tilt of the bipyramid influences the overlap of the electric field strength and the MoS_2. Figure 5.11a and b shows the average electric field strength in the CTAB and MoS_2 layer directly underneath each bipyramid. This was done for the same bipyramids as previously discussed from figures 5.9, with varying lengths and tip radii. The average electric field strength in the CTAB and MoS_2 increases with bipyramid length, especially when the bipyramid tip is sharp in comparison with the rest of the bipyramid dimensions. The average electric field strength underneath the bipyramids is also shown to increase for bipyramids with sharper tips, except for when they are tuned to overlap with the energy of the exciton. This is attributed to the larger modal volume. These results are consistent with the previous results of the maximum electric field strength value being increased for larger bipyramids and bipyramids with smaller tip radii.

These simulations were investigated further to check the ratio of the average electric field strength within the CTAB layer to the MoS_2 layer underneath. The results are shown in figure 5.11c and d. These are important results, as they show how the shape of the bipyramid influences the level of interaction between the plasmon and exciton. A larger ratio between the average electric field strength in the MoS_2 layer to the CTAB layer indicates a stronger interaction between the plasmon and exciton.

Figure 5.11c shows that the interaction with the MoS_2 layer is stronger for larger bipyramids. The one outlier is the 70 nm bipyramid with aspect ratio 2.3, not adjusted to overlap with the exciton energy. The plasmon of this bipyramid is particularly far from the exciton energy, as described above, which explains why it does not follow the same trends as the others. Figure 5.11d shows that a sharper tip results in a higher interaction between the bipyramid and the MoS_2, with the high electric field strength overlapping more closely with the MoS_2 for the bipyramids with the smaller tip radii.

These results confirm what was shown in figure 5.10. A lower aspect ratio, or tip radius that is sharper in relation to the rest of the bipyramid dimensions results in a stronger interaction with the MoS_2 layer. This is due to the natural bipyramid tilt towards the substrate, which is increased under these conditions.

Another interesting feature of the bipyramid as a nanoantenna is the mode volume. as

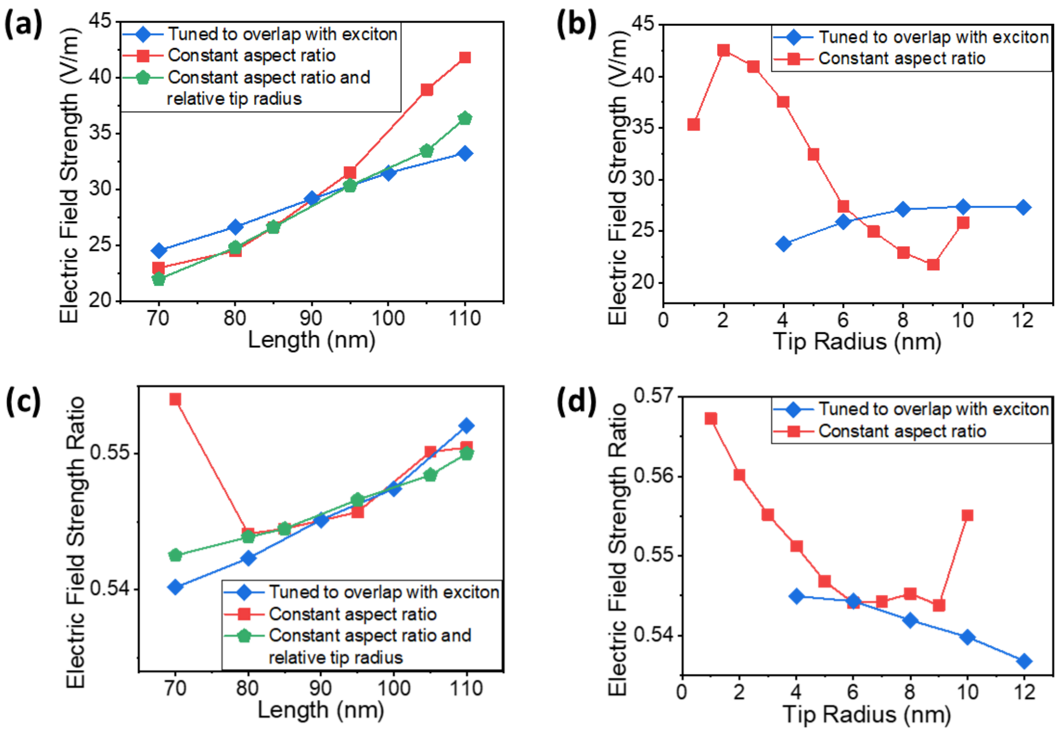

Figure 5.11: (a,b) The average electric field strength (V/m) in the CTAB and MoS_2 layers underneath bipyramids of varying lengths and tip radii, respectively. (c,d) The ratio of the average electric field strength within the MoS_2 layer to the average electric field strength within the CTAB layer underneath bipyramids of varying lengths and tip radii, respectively. The same bipyramids were investigated as in figure 5.9 for all plots.

---

shown in equation 2.15, the coupling strength increases as the mode volume decreases. Bipyramids have a strong electric field confinement at their tips, resulting in a low mode volume, even when the overall size of the bipyramid is increased. The mode volume primarily depends on the tip radius. The mode volume is defined as

$$V = \frac{\int \varepsilon E^2 dV}{Max(\varepsilon E^2)} \tag{5.4}$$

where ε is the permittivity and E is the electric field strength.

Simulations were carried out to find the mode volume for each of the bipyramids simulated in figure 5.9, with varying lengths and tip radii. Equation 5.4 was used, integrating only within the MoS_2 layer underneath the bipyramid as this was the area of interest. The results are shown in figure 5.12.

When the tip radius is increased to keep the proportions constant, as in the green line in figure 5.12a, or when the tip radii are increased, as in both lines in figure 5.12b, there is a clear trend of an increasing mode volume with increasing tip radii, as expected. This further clarifies the need for sharp tips to achieve strong coupling with the plasmons of bipyramids.

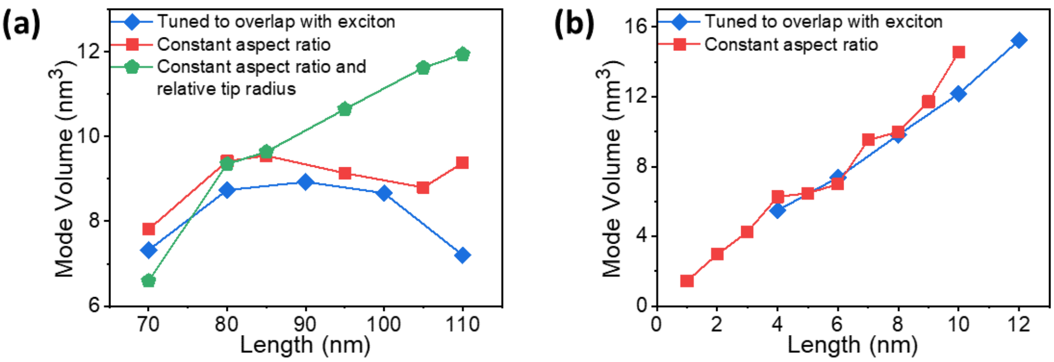

Figure 5.12: The mode volume within the layer of MoS_2 for changing (a) lengths and (b) tip radii of bipyramids. The same bipyramids were investigated as in figure 5.9.

A sharper tip concentrates the electric field into a smaller volume, as well as directing the plasmon resonance more directly towards the substrate. A more direct overlap of the plasmon resonance and the exciton also reduces the mode volume as the electric field is directed at a less oblique angle towards the exciton (see figure 5.10).

There is very little change in the mode volume when the bipyramid length is changed, with the tip radius kept constant. This is especially true when the aspect ratio is kept constant (see red line, figure 5.12a). The outlier here is again the 70 nm bipyramid with its plasmon further away in energy to the exciton. The changes are slightly different when the aspect ratio is changed to keep the plasmon energetically overlapping with the exciton (blue line, figure 5.12a). A slight increase in mode volume when the bipyramid length is increased from 70 nm to 80 nm can be explained by the change in aspect ratio required to keep the plasmon energy constant for the longer bipyramids. The decreased aspcet ratio can have a slightly rounding effect on the bipyramid tips, incerasing the mode volume. Conversely, the decrease in aspect ratio also has the effect of tilting the plasmon towards the substrate (see figure 5.10). This has the effect of bringing the mode volume back down again, as can be seen as the length is increased from 100 to 110 nm.

These results show that the interaction between the plasmon and exciton can be controlled in many ways. Bipyramids are a particularly interesting shape to demonstrate this. The sharp tips can confine the electric field enhancement into very small volumes, even for much larger bipyramids, as the tip radius does not need to increase when the bipyramid length does. The Rabi splitting can be increased by keeping the tip radii as small as possible, and also by reducing the aspect ratio.

5.5 Conclusion

Bipyramids are a particularly interesting nanoparticle to study for the effect of Rabi splitting due to their unusual shape and natural tilt towards the substrate on which they are resting. The Rabi splitting strength between the longitudinal plasmon of a Au bipyramid and the A exciton of a monolayer of MoS_2 can be controlled by a bipyramid's length, aspect ratio and tip radius. A bipyramid with increased metal volume has a stronger plasmon, resulting in a stronger electric field strength at its tips. Therefore, the interaction is stronger with the MoS_2, resulting in a higher Rabi splitting strength.

There are, however, many other factors which influence the Rabi splitting strength of a system with bipyramids. The electric field strength at a bipyramid's tips is increased when the tip radii are reduced. Low tip radii also have the effect of reducing the overall mode volume of the resonance. Both effects increase the Rabi splitting strength. A bipyramid's tips do not have to increase in radius when the overall metal volume increases because the size of the tip radius is dependent on a thermodynamic limit, not on the rest of the particle size. Therefore, there is no trade-off necessary between the metal volume and tip radius of a bipyramid. It is possible to have both a large bipyarmid and a low tip radius, maximising the Rabi splitting strength.

The natural tilt of a bipyramid resting on top of a substrate gives it another advantage over other nanoparticle shapes such as spheres, rods or prisms. A bipyramid's plasmonic resonance is directed towards the substrate on which it is resting. This greatly reduces the problem of a lack of alignment between the electric field and excitonic dipole moment that can affect Rabi splitting systems that utilise other nanoparticle types. This princlple can also be used to control the degree of coupling with a bipyramid by altering the aspect ratio and tip radius. A low aspect ratio increases the angle of the tilt of the bipyramid towards the substrate. Similarly, a low tip radius increases the tilt angle. An increased tilt angle, tilting the plasmon resonance more directly towards the substrate, causes an increased Rabi splitting strength in both cases.

This investigation is the first demonstration of the increase of Rabi splitting strength with increased metal volume of a plasmonic nanoresonator, without increasing the number of excitons coupled into the system. Therefore, this investigation has revealed an entirely new mechanism by which the control of Rabi splitting strength can take place.

I dwell in Possibility

Emily Dickinson

6 Photoluminescence Enhancement of Monolayer MoS_2 with a Silicon Disk Array

6.1 Introduction

Two-dimensional materials are widely investigated for many optical and electronic applications, including nanolasers[168], photodecectors[169] and nonlinear optic devices[170]. The low dimensionality of 2D materials make them easy to integrate with other device components. Their atomic thickness can also cause a problem for their use in photonic devices, due to the Beer-Lambert absorbance law:

$$A = \varepsilon c l \tag{6.1}$$

where A = absorbance, ε = molar absorption, c = concentration and l = path length. This equation puts severe limits on the utility of 2D materials in photonic devices due to the low absorbance of thin materials. Therefore, photonic devices must be designed to increase the absorption of incident light into the small dimension of 2D materials to convert photon energy into other forms of energy.

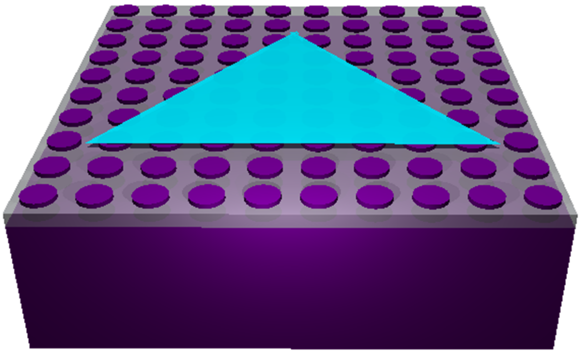

Figure 6.1: A schematic of the system of a Si disk array on a SiO_2/Si substrate, topped with a monolayer of MoS_2.

In this chapter, both experiments and FDTD simulations are employed to demonstrate the increased absorption of light within a monolayer of MoS_2 when it is integrated with a Si disk array on a SiO_2/Si substrate. A schematic of this system is shown in figure 6.1. Further simulations are carried out to demonstrate how this system can be optimised to increase the absorbance of the MoS_2 layer and the Si disk array. The FDTD simulations carried out in this chapter modelled MoS_2 with a thickness of 0.75 nm with the permittivity given by Li *et al.*[171].

6.2 Design and Fabrication of the Si Disk Array coupled to a monolayer of MoS_2

The Si disk array was fabricated using a Si-on-insulator wafer, with 45 nm Si on 150 nm SiO_2 on a Si substrate, commercially bought from Soitec. This was coated in A3 poly(methyl methacrylate) (PMMA) by spinning at 3000 rpm to use as a resist for patterning with electron beam lithography (EBL). Methyl isobutyl ketone–isopropyl alcohol (MIBK-IPA) at a ratio of 1:3 was used as a developer. Cr was deposited by e-beam evaporation using a Temescal, and hot Remover 1165 was used to lift-off. The patterned Cr was then used as a hard mask to transfer the pattern into the Si layer with inductively coupled plasma (ICP), etching through the top Si layer. The Cr mask was then removed with a commercial Cr etchant from Sigma Aldrich.[3] The MoS_2 monolayer was grown using CVD and was transferred onto the Si disk substrate[125] as described in section 3.3.2.[4]

The Si disk arrays were designed to have periodicity 500 nm in both the x and y directions. Several different arrays were fabricated with Si diameters varying from 300 to 320 nm. The heights of the Si disks were 45 nm and the thickness of the SiO_2 layer was 140 nm. An SEM image of the MoS_2 layer on top of the Si disks is shown in figure 6.2a. A closer image is shown in figure 6.2b, showing more clearly the uniformity of the Si disks investigated.

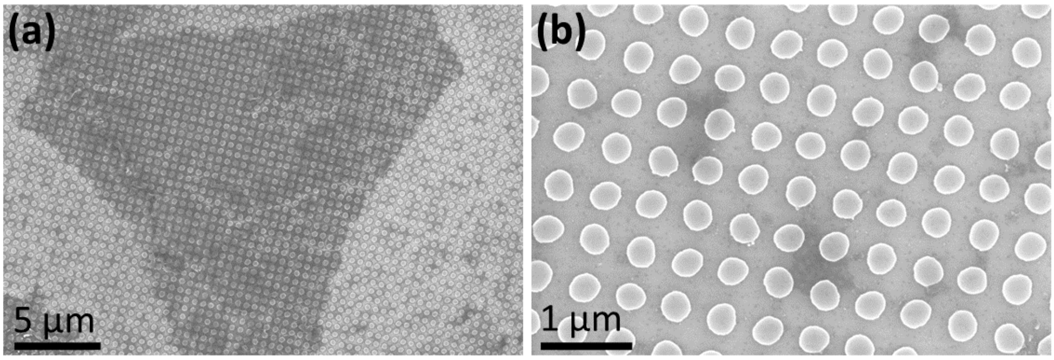

Figure 6.2: SEM images of the Si disk array topped with a monolayer of MoS_2.

---

[3] The fabrication of the Si disk array was carried out by Jing Li.

[4] The growth and transfer of the MoS_2 flakes was carried out by Lisanne Peters and Niall McEvoy.

Raman spectroscopy was performed on the MoS_2 flakes both on and off of the arrays to ensure that the flakes were all monolayer. This measurement also confirmed that the strain on the flakes from the Si disks underneath did not significantly distort the vibration modes of the MoS_2, ensuring that the quality of the flakes was kept high for all measurements undertaken. The distance between the E^1_{2g} and A_{1g} peaks in /cm units was mapped out for flakes both on the Si disk array and for flakes directly on the SiO_2/Si substrate. For bilayer MoS_2, the separation between the two peaks is $> 22cm^{-1}$[172]. The separation between the peaks is $19.2cm^{-1}$ for the flakes on top of the Si disk array and $18.2cm^{-1}$ for the flakes directly on the SiO_2/Si substrate. This clearly indicates that both maps show a flake of monolayer MoS_2. The small difference between the flakes on and off the Si disk arrays show that the Si disks have a small impact on the MoS_2 flakes, but do not introduce any significant strain or significantly influence the doping level. The small differences in the distances between the peaks are expected, as they are highly dependent on the material of the substrate the MoS_2 monolayer is placed on[173].

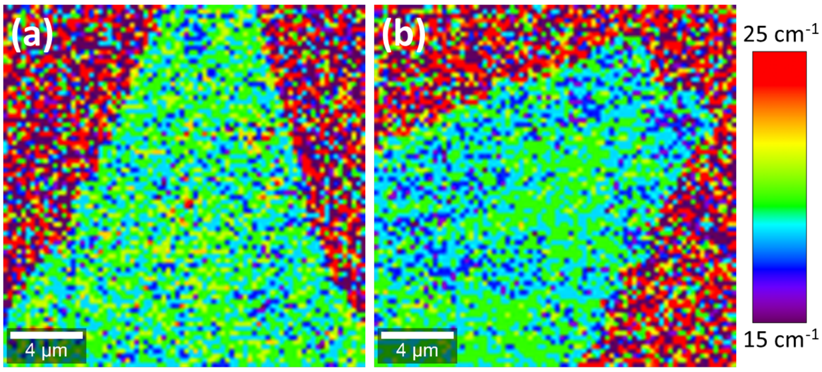

Figure 6.3: Raman maps of an MoS_2 flake (a) on a Si disk array and (b) directly on the SiO_2/Si substrate. The maps show the distance between the E^1_{2g} and A_{1g} peaks in cm^{-1} units. White scale bars show 4μm.

6.3 Photoluminescence Enhancement

The absorption of a quantum dot, or in this case, a TMDC monolayer, can be probed by measuring the photoluminescence intensity, because the fluorescence is proportional to the absorption of the laser light. The PL intensity of the MoS_2 flakes both on and off the arrays was measured by using lasers at two different wavelengths, 405 nm and 532 nm. The Si disks were shown to enhance the PL intensity for both wavelengths of laser, but by different amounts. The PL spectra for 320 nm Si disks are shown in figure 6.4 The results were averaged over 40 different spectra taken over the MoS_2 flakes on the arrays with 320 nm Si disks.

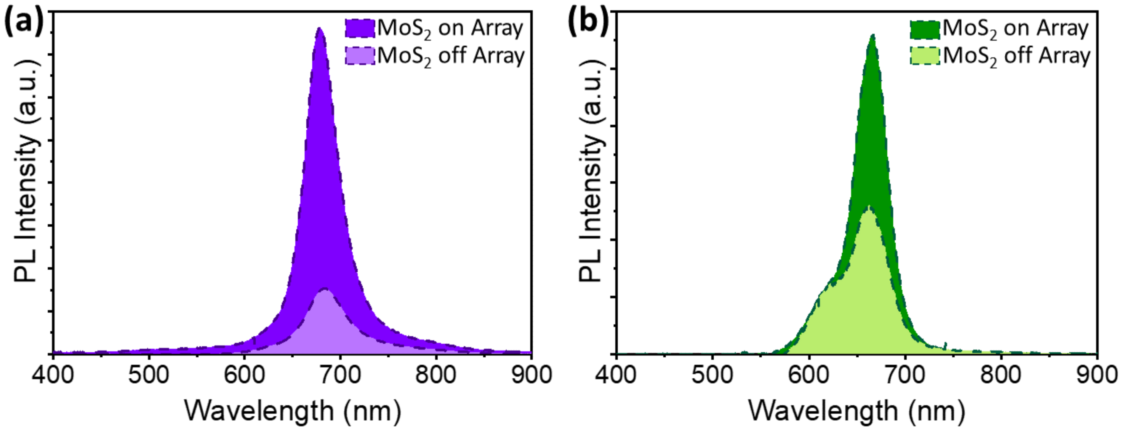

Figure 6.4: PL spectra of MoS_2 flakes on and off of the Si disk arrays. The spectra were taken using a (a) 405 nm and a (b) 532 nm laser.

The Si disk arrays are shown to increase the PL intensity using both lasers. The PL enhancement of the MoS_2 in the presence of the Si disks obtained with the 405 nm laser is 5.0 ± 1.8 and for the 532 nm laser it is 2.1 ± 0.7. The laser frequency dependence strongly indicates that the presence of the Si disks underneath the MoS_2 layer is having a strong influence on the absorption of the MoS_2. This is because the emission of the PL is the same regardless of the pump energy of the laser used, so if the PL intensity is different for different pump laser energies, the absorbance must be altered. PL spectra were taken on MoS_2 flakes on the arrays with differently sized disks. For each different size of disk, the average of 40 measurements was taken. The results of the enhancement are shown in figure 6.5a. As can be seen, there was no change in the PL spectra over the Si disk diameter range investigated.

There is a slight difference in the shape of the PL spectra obtained with the two different laser frequencies, as seen in figure 6.4. The peak corresponding to the B exciton is much stronger in the spectrum in figure 6.4b, obtained with the 532 nm laser, appearing as a shoulder to the right of the main peak of the A exciton. This is attributed to a different laser power of both lasers used. The 405 nm laser was used at a power of ≈ 0.2 mW, while the 532 nm laser was used at a power of ≈ 0.8 mW. For the MoS_2 on the disks in figure 6.4b, the B exciton emission does not seem to increase in intensity as the A exciton emission does for the MoS_2 on the Si disks. This indicates that the B exciton has become saturated with the higher absorption of light due to the presence of the Si disks. The B exciton is not visible at all in the 405 nm case, as shown in figure 6.4a, indicating that more light is being absorbed by the 405 nm laser than the 532 nm laser. Further investigation was carried out to confirm the dependence of the MoS_2 spectrum wavelength of maximum intensity on the laser power used. The results are shown in figure 6.5b.

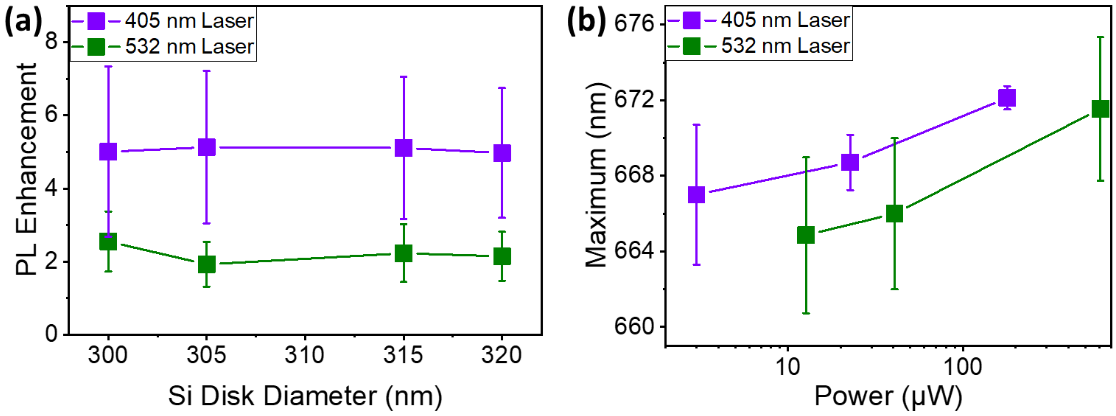

Figure 6.5: (b) Positions of the maximum intensity in the PL spectra taken from the MoS_2 on the Si disk arrays for different laser powers for both the 405 nm and the 532 nm lasers.

For both lasers used, the position of the maximum intensity is shown to red-shift slightly as the laser power was increased. This effect was also demonstrated by Kaplan *et al.*[174]. This shows that the A exciton becomes more dominant over the B exciton in absorbing the incoming light for an increased laser power. The 405 nm laser is shown to give a more red-shifted PL spectrum compared to the 532 nm laser for the same laser power. This indicates that the absorption is higher for the 405 nm laser than the 532 nm laser.

It is evident from the above results that the Si disks are driving an increased absorption in the MoS_2 monolayer. However, the PL measurements alone cannot predict the exact level of absorption within the MoS_2 layer. This is because the Si disks can also have an influence over the emission from the system by altering the quantum efficiency within the MoS_2 layer[175]. The absorbance of the entire system can be measured experimentally as

$$A = 1 - R - T \tag{6.2}$$

where A is the absorbance, R is the reflectance and T is the transmittance. The transmittance in this system is 0, because of the thickness of the Si substrate used. Therefore, the total absorbance, including the absorbance within the Si substrate, can be calculated from the reflectance as $A = 1 - R$.

A small portion of light is also scattered. The scattering spectra were calculated for all systems investigated in this chapter using FDTD simulations, and it was found that the scattered light consisted of $\approx 1.4\%$ of all incident light for each system across the wavelength range considered. Due to this very small proportion, the scattered light is neglected for the rest of this chapter.

Figure 6.6 shows the experimentally measured reflectance as well as the reflectance calculated by FDTD simulations. There is good agreement between the two spectra. When the MoS_2 layer was added, the point of lowest reflectance red-shifted by 8 nm in both the experimentally measured and simulated spectra for the system with 300 nm disks. It also shifted by 18 nm and 11 nm for the experimental and simulated spectra with the 320 nm disks. It is also interesting to note that the disks with larger diameters have a slightly blue-shifted minimum, corresponding to the point of the system's highest absorbance. The minimum of the system with 300 nm disks with an MoS_2 layer on top red-shifts by 27 nm and 20 nm for the experimental measurements and simulations, respectively when the diameters are increased to 320 nm.

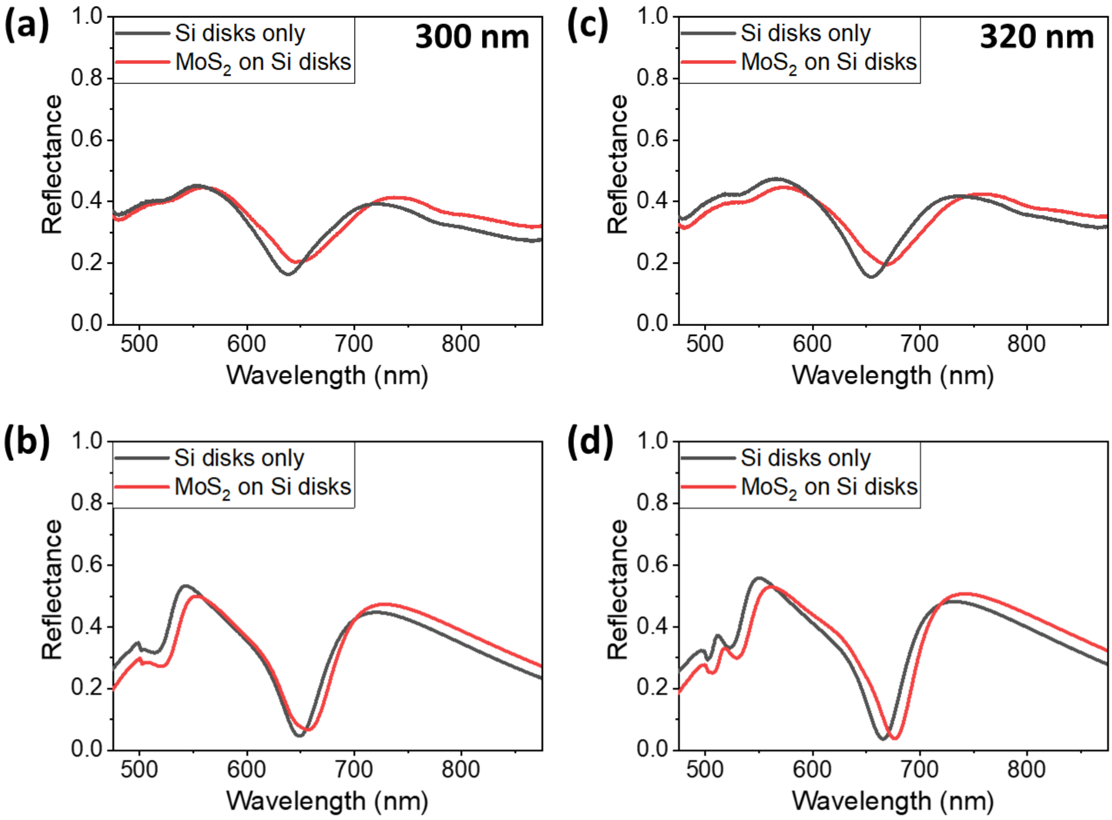

Figure 6.6: (a) Experimental and (b) simulated results for the total reflectance for a the system with 300 nm disks. (c) Experimental and (d) simulated total reflectance for the same system with 320 nm disks.

While this can be used to experimentally measure the absorbance of the entire system, including the substrate, another method must be employed to measure the absorbance of the separate elements within the system. From the reflectance spectra in figure 6.6, it is not possible to determine if the absorbance is high because of the interaction of the MoS_2 layer and Si disks with the incoming light, or simply because the thick Si substrate absorbs most of the non-reflected light. FDTD simulations were employed to find the absorbance of the different components in the hybrid MoS_2 and Si disk system.

The absorbed power per unit volume can be calculated by taking the divergence of the Poynting vector as follows

$$P_{abs} = \frac{1}{2} Re(\nabla \cdot \vec{P}) = \frac{1}{2} Re(i\omega \vec{E} \cdot \vec{D}) = \frac{1}{2} \omega \varepsilon_0 Im(\varepsilon)|E|^2 \tag{6.3}$$

P_{abs} is the absorbance, $\vec{P}$ is the Poynting vector, ω is the angular frequency of the light, $\vec{E}$ is the electric field vector, $\vec{D}$ is the displacement field vector, $Im(\varepsilon)$ is the imaginary part of the permittivity within the volume being examined and $|E|$ is the electric field amplitude. The divergence of the Poynting vector is changed to a form where it is more stable for FDTD simulations, and less sensitive to numerical problems. Therefore, the absorption over the volume of the structure considered is given by

$$P_{abs} = \frac{1}{2} c \varepsilon_0 k_0 \int\int\int_V Im[\varepsilon(r)]|E(r)|^2 dV \tag{6.4}$$

where k_0 is the free-space wave-vector. The absorbance, α, is the ratio of the absorbed power, P_{abs} to the incident power, P_{inc}[176, 177, 178].

$$\alpha = \frac{P_{abs}}{P_{inc}} = \frac{k_0}{S_0|E_0|^2} \int\int\int_V Im[\varepsilon(r)]|E(r)|^2 dV \tag{6.5}$$

where S_0 is the exposed surface area, $|E_0|$ is the electric field amplitude of the incident light and $P_{inc} = \frac{1}{2} c \varepsilon_0 S_0 |E_0|^2$.

This model can be used to calculate the absorbance of both the MoS_2 layer and the Si disks individually. FDTD simulations are used to calculate $|E(r)|^2$ within both the MoS_2 layer and the Si disks. The simulation is carried out with periodic boundary conditions over the unit cell of area 500 × 500 nm, S_0. To measure the absorbance within the MoS_2 layer, V is taken as $S_0 \times t$, where t is the thickness of the MoS_2 layer. To measure the absorbance of the Si disks, V is taken as $\pi \times R_{disk}^2 \times h_{disk}$, where R_{disk} is the disk radius (160 nm), and h_{disk} is the height of the disks (45 nm).

The absorbance within the MoS_2 layer and within the disks was calculated for the whole system with a Si disk array of height 45 nm, diameter 320 nm and periodicity 500 nm in both directions, on 140 nm SiO_2 on Si, topped with a monolayer of MoS_2. The absorbance was also calculated for the MoS_2 layer on the same substrate but without the Si disks, and for the Si disks on the same substrate but without the MoS_2 monolayer.

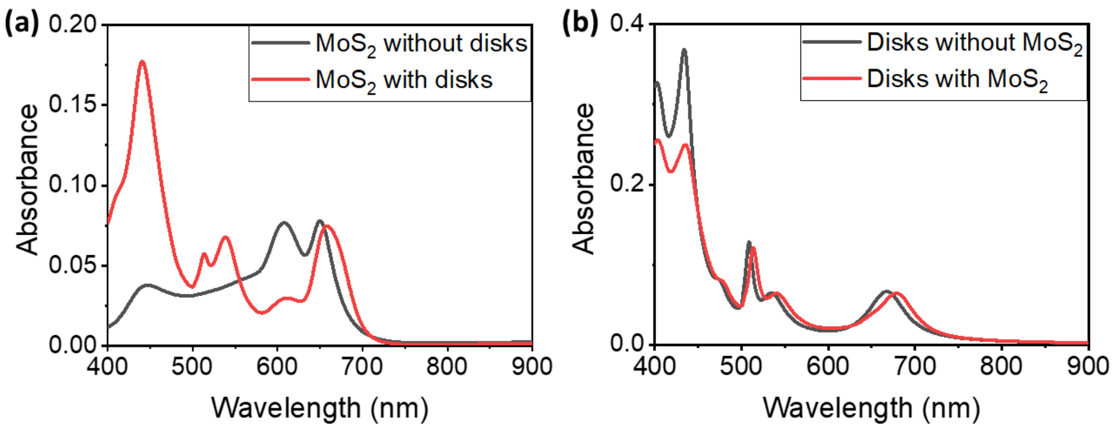

Figure 6.7: (a) Absorbance of the MoS_2 layer directly on the SiO_2/Si substrate and on the Si disk array on the substrate. (b) Absorbance of the Si disk array without the MoS_2 layer on top and with the MoS_2 layer on top.

The absorbance within the MoS_2 layer is shown in figure 6.7a, for the case of the MoS_2 layer sitting directly on top of the SiO_2/Si substrate without any Si disks, and for the case of the MoS_2 layer sitting on top of the Si disk array on top of the SiO_2/Si substrate. It is evident that the presence of the Si disks has a large effect on the absorbance of the MoS_2 layer. To investigate this, the absorbance within the Si disks was also calculated as shown in figure 6.7b. This plot shows the absorbance of the Si disks on the SiO_2/Si substrate both with and without the layer of the MoS_2 on top.

For the case with the Si disks without the MoS_2 layer, in the range of 400 to 450 nm, about 30% of the incident light is absorbed by the Si disks. This large absorbance is mirrored in the MoS_2 layer when the Si disks are present underneath, increasing the absorbance from $\approx 4\%$ to $\approx 16\%$. This shows that an increased absorbance in the Si disks can help increase the absorbance in the thin MoS_2 layer, especially where the negative permittivity is high. Similarly, the high absorbance in the Si disks, up to $\approx 10\%$, in the range of 500 to 550 nm has an influence on the MoS_2 layer, increasing its absorbance too. Interestingly, the lower absorbance in the disks in the range 550 to 650 nm of about 2% also has an influence on the MoS_2 absorbance, reducing it compared with the case of no Si disks underneath. The presence of the MoS_2 layer is also shown to have an influence on the absorbance of the Si disks. The absorbance in the range 400 to 450 nm is significantly reduced due to the high absorbance of the MoS_2 layer over those wavelengths. The other wavelengths of increased absorbance are slightly red-shifted when the MoS_2 layer is added.

The electric field strength in the Si disks serves to influence the electric field strength within the MoS_2 layer, altering its absorbance. This is demonstrated most clearly in equation 6.4, showing how a high electric field strength increases the absorbance within the material. This can explain why the PL enhancement due to the presence of the Si disks is different for the two different laser frequencies used. The absorbance in the MoS_2 layer at 405 nm is increased a lot more than the absorbance at 532 nm. The absorption enhancement within the MoS_2 layer can be calculated by the ratio of the absorbance of the MoS_2 layer on the Si disk array to the absorbance of the MoS_2 layer directly on the SiO_2/Si substrate. This is shown in figure 6.8.

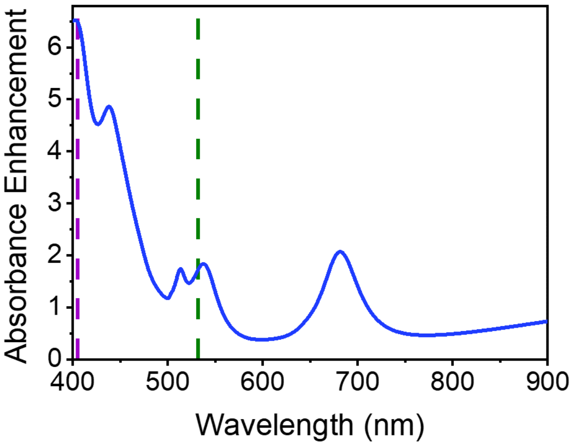

Figure 6.8: Ratio of the absorbance of the MoS_2 layer on top of the Si disk array on the SiO_2/Si substrate to the absorbance of the MoS_2 layer directly on top of the SiO_2/Si substrate. The pump wavelengths are marked with a purple (405 nm) and a green (532 nm) dashed line.

The absorption enhancement at the wavelengths of both lasers used to experimentally measure the PL are 6.5 and 1.7 for the 405 nm and the 532 nm lasers, respectively. The positions of the laser pump wavelengths are marked by the purple (405 nm) and green (532 nm) dashed lines. However, to gain a more complete understanding of the experimentally measured PL enhancement the modification of the emission at the wavelength of the PL must also be considered. The full equation to account for the PL enhancement is given by[179]

$$\eta = \frac{\alpha(\lambda_{pump})}{\alpha^0(\lambda_{pump})}\frac{q(\lambda_{em})}{q^0(\lambda_{em})} \tag{6.6}$$

where α is the absorbance of the MoS_2 layer with the Si disks, α^0 is the absorbance of the MoS_2 layer without the Si disks, λ_{pump} is the wavelength of the laser used to take the PL measurement, q is the quantum efficiency in the MoS_2 layer with the Si disks, q^0 is the quantum efficiency in the MoS_2 layer without the Si disks and λ_{em} is the wavelength of the peak emission of the PL spectrum.

The quantum efficiency is less than 1 because the excitonic relaxation rate (γ) is split into two types, the radiative (γ_r) and the non-radiative (γ_{nr}) rates. In the presence of a nanoantenna, an additional non-radiative decay rate (γ_{loss}) must also be considered. This accounts for the photons absorbed into the nanoantenna. Therefore, the quantum efficiency of a system is given by

$$q = \frac{\gamma_r}{\gamma_r + \gamma_{nr} + \gamma_{loss}} \tag{6.7}$$

The decay rates, γ_r, γ_{nr} and γ_{loss} cannot be calculated by FDTD simulations, but the quantum yield can still be found by using an electric dipole source in the simulation. The ratio of the decay rate of the emitter with a nanoantenna to the decay rate without a nanoantenna is the same as the ratio of the power emitted by the electric dipole with a nanoantenna to the power emitted without a nanoantenna, $\frac{\gamma_r}{\gamma_r^0} = \frac{P_r}{P_r^0}$ and $\frac{\gamma_{nr}}{\gamma_{nr}^0} = \frac{P_{nr}}{P_{nr}^0}$.

The radiative rate of an electric dipole in free space is defines as $\Gamma_0 = \frac{P_r^0}{\hbar\omega}$, where P_r^0 is the total power emitted by the dipole in all directions. The optical properties of a dipole are modified in the presence of the Si disks, so the Purcell factor is calculated as

$$g_P = \frac{\Gamma_r}{\Gamma_r^0} = \frac{P_r}{P_r^0} = \sum_{box} T_i \tag{6.8}$$

where T_i is the calculated transmission through each face of a monitor box around the entire system with the electric dipole. The modified radiative emission rate in the presence of the Si disks is then calculated as

$$\gamma_r = \gamma_r^0 \int_{400}^{1000} g_P f_0(\lambda) d\lambda \tag{6.9}$$

where γ_r^0 is the radiative emission rate of MoS_2 surrounded by vacuum[180], λ is wavelength and $f_0(\lambda) = \frac{PL(\lambda)}{\int PL(\lambda) d\lambda}$ is an integral normalised PL spectrum, where $\int f_0(\lambda) d\lambda = 1$. $PL(\lambda)$ is taken from the experimentally measured PL spectra as seen in figure 6.4. The shape is slightly different, as discussed previously for the two different lasers used, so the quantum efficiency calculations were carried out separately for both laser powers used.

Similarly, the modified non-radiative emission rate can be calculated as

$$\gamma_{loss} = \gamma_r^0 \int_{400}^{1000} g_{Loss} f_0(\lambda) d\lambda \tag{6.10}$$

where g_{Loss} is the total power absorbed by the system. It can be calculated by using the same power box around the system as for g_P, and another power box around the dipole only. It can then be calculated by

$$g_{Loss} = \frac{P_{Loss}}{P_0} = \frac{P_{dip} - P_r}{P_0} \tag{6.11}$$

where P_{Loss} is the total power absorbed by the system and P_{dip} is the total power emitted by the dipole in the system. Therefore, the modified decay time of the emission of the MoS_2 in the presence of the Si disks can be written as

$$\tau_{PL} = \frac{1}{\gamma_r + \gamma_{loss} + \gamma_{nr}} \tag{6.12}$$

with the non-radiative decay rate (γ_{nr})[180] unchanged by the presence of the Si disks. The quantum yield can then be calculated as $q = \tau_{PL}\gamma_r$, as in equation 6.7.

The detection rate is also taken into account when determining the PL. Only the photons emitted upwards are detected with an optical microscope, so instead of using the Purcell factor, g_p, to calculate the quantum yield of detected photons, γ_{det} is calculated by only considering the power transmission through the top monitor in the power box around the whole system. Therefore, $g_{det} = \gamma_r^0 \frac{P_{det}}{P_0}$, with P_{det} being the total power transmitted through the top panel of the monitor box around the entire system. The total quantum efficiency can then be calculated as[175]

$$q = \tau_{PL} g_{det} f_0(\lambda) \tag{6.13}$$

These calculations were carried out for electric dipoles positioned in nine different locations within the unit cell, as shown in figure 6.9a, above the Si disks where the MoS_2 layer is positioned. Only the two orientations parallel to the substrate were considered, mimicking the dipole moment of the A exciton in monolayer MoS_2[181]. The quantum efficiency was averaged over the results found for the dipoles positioned at the nine different places. Only one orientation was calculated for the dipole situated in the center of the Si disk and in the center of four disks (in the corner of the unit cell) due to the xy symmetry of the Si array. The total quantum efficiency for the MoS_2 over the whole disk was approximated by averaging all of the results from the 16 different dipoles with contributions proportional to the areas corresponding to each dipole position as shown in figure 6.9b. The quantum efficiency of a dipole positioned directly on top of the SiO_2/Si substrate was also calculated. Therefore, the PL enhancement due to the presence of the Si disks was calculated with equation 6.6.

The quantum efficiency was quenched in the MoS_2 positioned over the Si disks, but enhanced for the dipoles positioned between the disks in the array compared to the MoS_2 placed directly on the SiO_2/Si substrate. This is shown in figures 6.9c and d, showing the emission enhancement for the shape of the PL spectrum obtained with the 405 nm laser and the 532 nm laser, respectively. The emission enhancement was slightly different for the two different shapes of PL spectra. For the spectrum obtained with the 405 nm and 532 nm lasers, the ratio, $\frac{q(\lambda_{em})}{q(\lambda_{em})^0}$, was found to be 1.06 and 1.22, respectively.

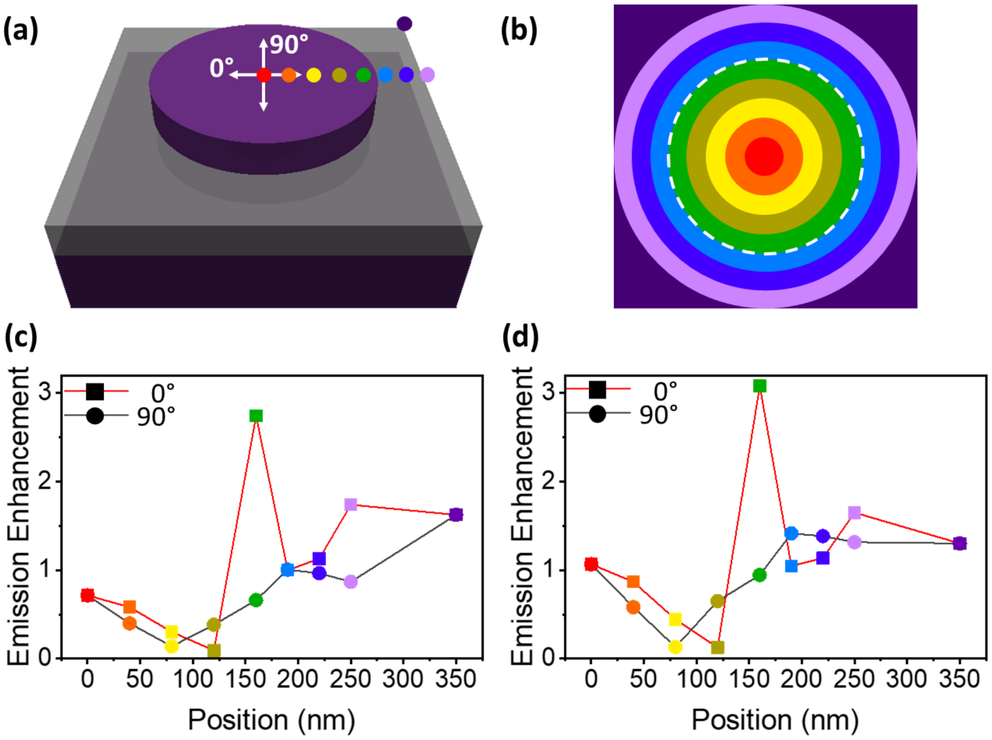

Figure 6.9: (a) Positions within the unit cell (in terms of distance from the center of an Si disk) where the dipoles were placed to calculate the average emission enhancement. (b) Colour-coded areas where the emission enhancement for each dipole was calculated. The white ring shows the position of the Si disk. (c,d) Emission enhancement calculated with the shape of the PL spectrum from the 405 nm laser and the 532 nm lasers, respectively. The enhancement is shown for dipoles positioned at each colour-coded area in figures (a) and (b) with two different orientations.

The absorption enhancement (figure 6.8) was multiplied by the quantum efficiency quenching factor calculated for both of the PL spectrum shapes for the two different lasers used. This showed the total PL enhancement, η, as shown in equation 6.6. The results are shown in figure 6.10, with the experimental results also marked in on the graphs. For the 405 nm laser, the simulations predicted a PL enhancement of 6.9, while the experiments showed a PL enhancement of 5.0 ± 1.8. For the 532 nm laser, the simulations predicted a PL enhancement of 2.1, while the experiments showed a PL enhancement of 2.1 ± 0.7. This demonstrates a close agreement between the experiments and the simulations.

A few factors could be contributing to the slight discrepancy between the simulated and experimental results. The experimental disks were not as perfectly circular as could be modelled with numerical simulations. Further, the refractive index used for the monolayer MoS_2 was slightly different than the MoS_2 used for the experiments due to small discrepancies in the literature[67, 171]. The numerical simulations could also be increased in accuracy by

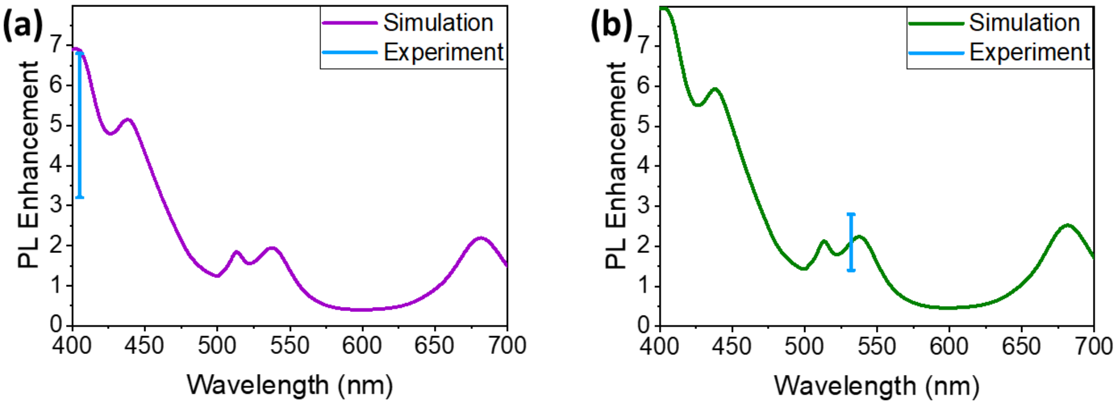

Figure 6.10: Simulated numerical calculations of the PL enhancement of the MoS_2 layer with a 320 nm Si disk array with a height of 45 nm and a periodicity of 500nm. Results are shown for the laser wavelengths of (a) 405 nm and (b) 532 nm. Experimental results are marked by the blue error bars.

---

performing more simulations with dipoles positioned at a larger number of points across the unit cell.

6.4 Optimisation for a Perfectly Absorbing System

The presence of the Si disks underneath the MoS_2 modifies the absorption of the MoS_2, but the absorption still remains low, reaching a high of 17.7% at 441 nm, and only 7.5% at the peak close to the A exciton at 658 nm (figure 6.7). Further simulations were carried out to investigate how this could be optimised. Figure 6.11 shows how the absorbance, reflectance and transmittance can be modified by the substrate that the Si disks and MoS_2 layer are sitting on 320 nm Si disks with a 45 nm height and a 500 nm xy periodicity with a monolayer of MoS_2 on top were inspected with three different substrates. The system was investigated suspended in air, with a substrate of 140 nm SiO_2 on Si and with a substrate of 140 nm SiO_2 on Au.

Schematics of each of these systems are shown in figure 6.11, with spectra of the reflectance, absorbance and transmittance underneath. No light is transmitted all the way through a Si or Au substrate, so the overall transmittance is zero for those systems. However, with the aim of investigating the absorption within the MoS_2 layer and Si disks only, the transmittance is taken as the transmittance through just the MoS_2 layer and the Si disks in the plots shown. Similarly, only the light absorbed by the Si disks and MoS_2 layer is considered for the absorbance. By comparing figures 6.11a and b, it is clear that the presence of the SiO_2/Si substrate reduces the absorbance. It is not experimentally realisable to design a system with Si disks suspended in air, but the Si in the substrate can be replaced with another material. Au was chosen as an efficient back-reflector, enabling the photons reflected from its surface to be absorbed by the hybrid Si disk and MoS_2 system. As can be seen in figure 6.11c, the absorbance in the MoS_2 and Si disks at 680 nm is 74%, slightly red-shifted from the peak of 40% absorbance at 669 nm for the system with no substrate beneath the Si disks. The lowest absorbance is shown for the Si disks on an SiO_2/Si substrate, where the maximum absorbance shown is 13% at 668 nm. The spectra in figure 6.11c also show an increased reflectance and a reduced transmittance of light through to the Au substrate. This indicates that the Au layer works by reflecting the originally transmitted photons back to be absorbed. At 680 nm, the reflectance reaches 0%, indicating that all of the incoming light is either absorbed by the MoS_2 and Si disk hybrid system or by the Au layer underneath. This design is therefore an example of a perfectly absorbing system.

The plots beneath the reflectance, absorbance and transmittance plots in figure 6.11 show the absorption of the Si disks and the MoS_2 layer separately. The plots below these show what the absorption would be in the MoS_2 layer without the Si disks present, and what the absorption in the Si disks would be without the MoS_2 layer present. For each substrate, when the MoS_2 monolayer is added on top of the Si disks, the absorption in the Si disks reduces with the maximum peak red-shifting slightly. This is due to the MoS_2 layer absorbing some of the light that the Si disks would have absorbed if the MoS_2 layer were not present. It is evident that the MoS_2 layer is absorbing light at the same wavelength as the Si disks underneath due to the very different absorption spectra of the MoS_2 layer when the Si disks are added to the system. The two peaks of high absorption in the MoS_2 corresponding to the high imaginary permittivity (610 nm and 650 nm) are quenched in the presence of the Si disks. A new peak corresponding to the peak of maximum absorption in the Si disks is greatly enhanced. By optimising the resonances of the Si disks, it is therefore possible to control what wavelength of light the MoS_2 layer will primarily absorb.

Further simulations were carried out to test if the absorption within the monolayer of MoS_2 could be increased if the point of maximum absorption within the Si disks was tuned to more closely overlap with the high imaginary permittivity of the MoS_2 layer. As was shown in figure 6.6, reducing the diameters of the Si disks blue-shifts the resonances. The same simulations were carried out to show the reflectance, absorbance and transmittance as well as the absorption within the MoS_2 layer and Si disks, but with a Si disk diameter of 300 nm and a SiO_2 layer thickness of 100 nm to increase the overall absorption.[5] The results are

---

[5] The optimisation for this system was carried out by Xia Zhang.

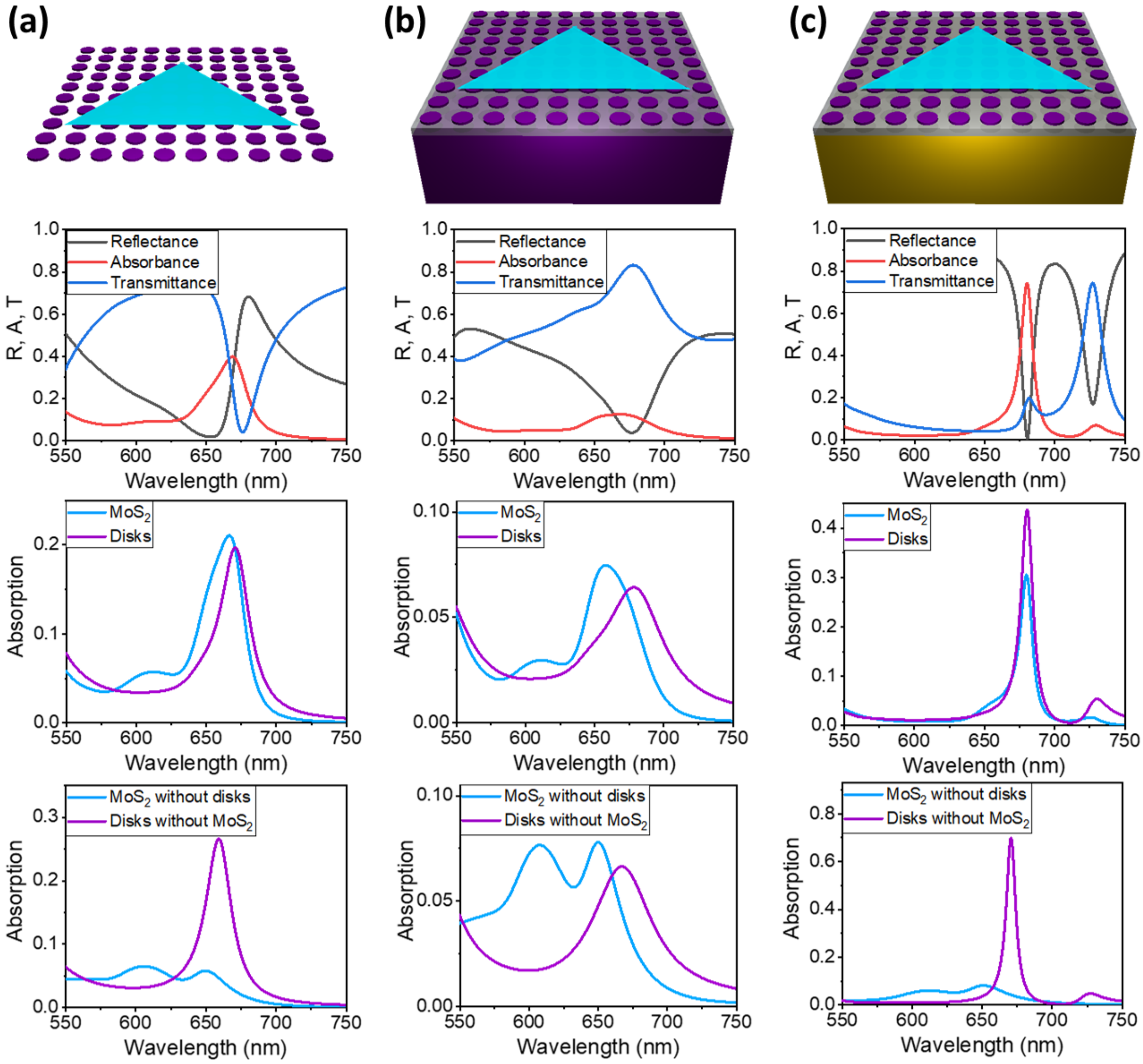

Figure 6.11: Reflectance, absorbance and transmittance for a MoS_2 monolayer on a Si disk array of diameter 320 nm, height 45 nm and xy periodicity of 500 nm. The spectra are of this system (a) in air, (b) on 140 nm SiO_2 on a Si substrate and (c) on 140 nm SiO_2 on a Au substrate. A schematic of each system is shown at the top. Below, spectra are shown of the reflectance from the whole system, the absorbance within the MoS_2 layer and the Si disks only and the transmittance through the MoS_2 layer and Si disks only. The second line of spectra show the absorbance within the MoS_2 layer and the Si disks for each system. The final line of spectra show what the absorbance in the MoS_2 layer would be without the Si disks present and what the absorbance in the Si disks would be without the MoS_2 layer present.

---

shown in figure 6.12.

With the smaller Si disk diameters and the thinner SiO_2 thickness, the maximum absorbance of the hybrid system blue-shifts to 646 nm, with 46% absorbance for the system suspended in air, 18% absorbance on the SiO_2/Si substrate and 81% absorbance on the

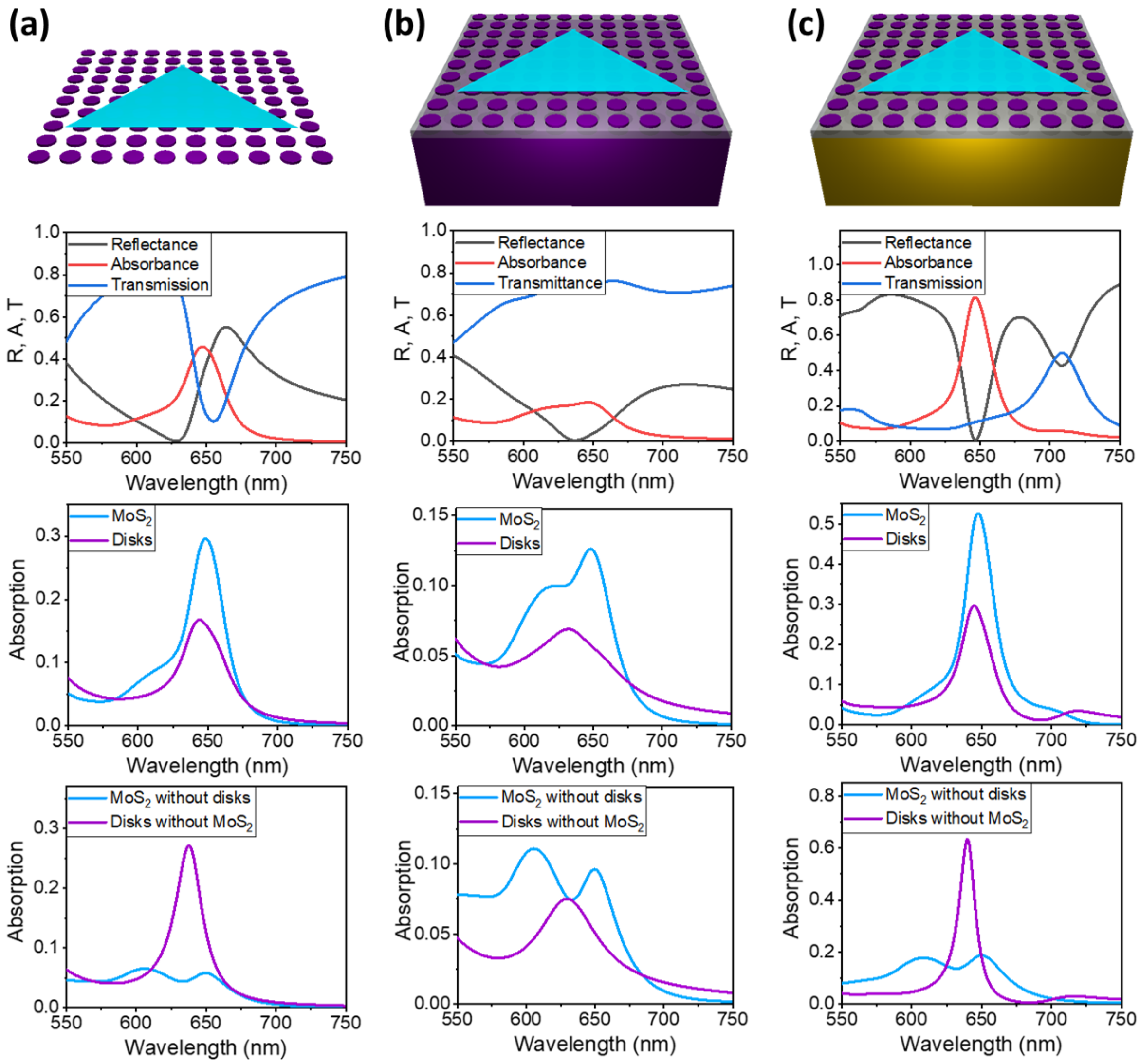

Figure 6.12: Reflectance, absorbance and transmittance for a MoS_2 monolayer on a Si disk array of diameter 300 nm, height 45 nm and xy periodicity of 500 nm. The spectra are of this system (a) in air, (b) on 100 nm SiO_2 on a Si substrate and (c) on 100 nm SiO_2 on a Au substrate. A schematic of each system is shown at the top. Below, spectra are shown of the reflectance from the whole system, the absorbance within the MoS_2 layer and the Si disks only and the transmittance through the MoS_2 layer and Si disks only. The second line of spectra show the absorbance within the MoS_2 layer and the Si disks for each system. The final line of spectra show what the absorbance in the MoS_2 layer would be without the Si disks present and what the absorbance in the Si disks would be without the MoS_2 layer present.

SiO_2/Au substrate. This is increased from the previous system shown in figure 6.11. The spectra showing the absorption of the MoS_2 layer without the Si disks and the absorption of the Si disks without the MoS_2 layer show a large overlap. This overlap drives the increased absorption of the MoS_2 layer when the disks are present. The MoS_2 monolayer absorbs more light than the Si disks for the system on all three substrates. The MoS_2 layer alone absorbs 30%, 13% and 53% of light at 647 nm. This is a huge enhancement from the absorbance of MoS_2 at this wavelength when it is suspended in air (6%), demonstrating the high control possible with modifications of the metasurface underneath.

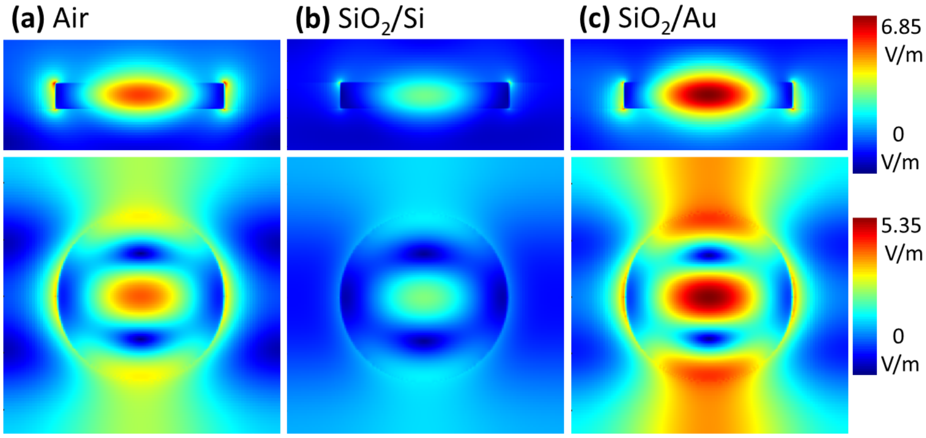

Figure 6.13: Maps showing the electric field strength within the system with the MoS_2 layer and 300 nm Si disks (a) in air, (b) on a 100 nm SiO_2 on Si substrate and (c) on a 100 nm SiO_2 on Au substrate. The top maps show the electric field strength through the Si disks, MoS_2 layer and substrate. The lower maps show the electric field strength within the MoS_2 layer. Each map shows one unit cell, with the x × z area for the top maps being 500 nm × 200 nm and the x × y area for the bottom maps being 500 nm × 500 nm.

Electric field maps at the wavelength of highest absorbance (646 nm) of the three systems in figure 6.12 are shown in figure 6.13. The maps show the cross-section of one unit cell perpendicularly through the Si disk and substrate and also through the MoS_2 layer above. The maximum electric field strength within the MoS_2 layer is 5.89 V/m for the Si disks suspended in air, 2.68 V/m for the SiO_2/Si substrate and 5.35 V/m for the SiO_2/Au substrate. The maximum electric field strength within the Si disks is 4.23 V/m for the system suspended in air, 3.63 V/m for the SiO_2/Si substrate and 6.85 V/m for the SiO_2/Au substrate. A higher electric field strength corresponds to a higher absorbed power from the incident light, as described in equation 6.4. This trend matches the absorbance of the system, with the structure on the Au substrate absorbing the most light, followed by the structure suspended in air, with the structure on the Si substrate absorbing the least. The total absorption is higher in the MoS_2 layer, despite its lower volume and lower electric field strength, due to the higher imaginary permittivity.

The highest absorbance within the MoS_2 layer was realised by utilising a Au mirror to back-reflect transmitted light back towards the MoS_2-Si disk hybrid system. However, a Au substrate would be very expensive and impractical to make experimentally. Further simulations were carried out, utilising a thin Au layer between a SiO_2 layer and a Si substrate instead. The thickness of the Au layer was varied between 0 and 100 nm. This is demonstrated in figure 6.14.

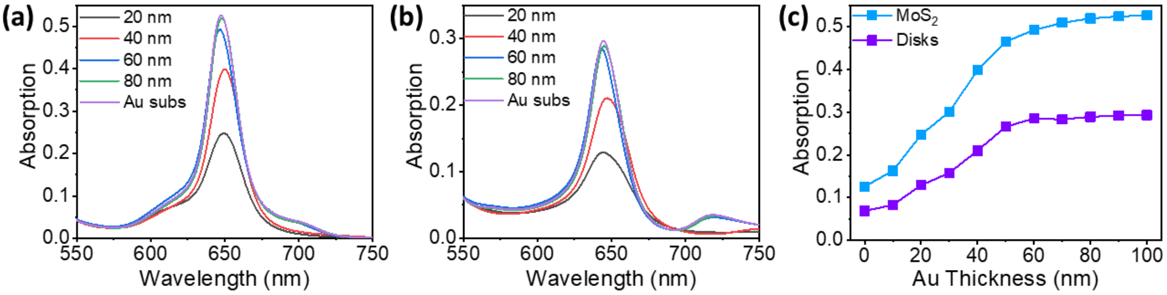

Figure 6.14: FDTD absorption calculations for a system with a MoS_2 monolayer on 300 nm Si disks and 100 nm SiO_2 on Au of varying thickness on a Si substrate. (a) and (b) show the absorption within the MoS_2 layer and the Si disks, respectively. (c) The absorption within the MoS_2 layer and the Si disks at the wavelength of maximum absorption for Au thicknesses varied from 0 to 100 nm.

It was found that a Au layer of thickness 70 nm on top of a Si substrate results in an absorbance of 51% in the MoS_2 and an absorbance of 78% within the hybrid MoS_2 layer and Si disks together at the wavelength 647 nm. This absorption is $> 95\%$ of the light absorbed when the entire substrate is Au, showing it to be an efficient and cost-effective alternative for the fabrication of this device. When the Au layer is increased to 100 nm, the absorbance, transmittance and reflectance behave in the same way as they do for an entire Au substrate.

6.5 Conclusion

Si disk arrays can be used as an effective metasurface to modify the optical properties of 2D materials. This was demonstrated both experimentally and numerically by investigating the effect of the PL intensity of a monolayer of MoS_2 with and without a Si disk array underneath. The PL was modified by a change in both the absorption and emission. The absorption was shown to be enhanced and quenched at different excitation wavelengths in the presence of the Si disk arrays, while the quantum efficiency was shown to be quenched slightly, reducing the emission of the PL.

Further simulations were carried out to optimise the absorption in the system, especially within the MoS_2 layer. It was found that the disk diameters could be modified to tune the resonance to overlap with the high imaginary permittivity in the MoS_2 layer, corresponding to the excitons. This resulted in a largely increased absorption in the MoS_2 layer at the resonance wavelength.

The materials in the substrates on which the Si disks were positioned were also investigated and optimised. It was found that using Au as a back-reflector under a layer of SiO_2 was the most efficient method of using the substrate to maximise the absorption within the MoS_2 layer. An absorbance of 53% within the MoS_2 layer was demonstrated by utilising a Si disk array on top of a SiO_2/Au substrate.

> The truth is rarely pure and never simple.
>
> Oscar Wilde

7 Conclusions

Three separate nanophotonic devices were investigated and studied in this thesis. In each device, the spectral response of a nanoparticle was modulated by coupling it to a two-dimensional material. Each system was investigated both experimentally and with numerical simulations. The wavelengths studied for each structure were primarily in the visible region.

In **chapter 4**, a system with a 150 nm Au sphere on a 100 nm Au film with an intermediate monolayer of graphene was explored. The Au sphere coupled with the Au film, creating three plasmonic modes, the dipolar, quadrupolar and octupolar modes. These modes were modulated by immersing the system in nitric acid. The nitric acid modified the system by doping the graphene layer. It also had the effect of removing residual CTAB and PMMA between the Au sphere and film, reducing the gap size. Both modifications in the gap region drive strong spectral shifts, primarily in the dipolar mode. The doping of the graphene has the effect of blue-shifting the plasmon modes, while the reduction of the gap size has the effect of red-shifting the plasmon modes. When the doping of the graphene is brought to 1.1 eV, the dipolar mode is shown to split into two new modes. This is attributed to the coupling of the gap plasmon and the charge transfer plasmon. The spectral response due to the doping of the graphene is demonstrated to be more pronounced when the gap between the Au sphere and film is reduced. This is because a smaller gap size increases the electric field strength confinement. Understanding the origin of the observed peaks and how to control them is essential for the development of photonic devices. The findings in this work show the fundamental behaviour of the plasmonic modes in a nanoparticle-on-mirror structure and give strong direction on how they can be manipulated and controlled within other systems.

Similarly to chapter 4, **chapter 5** demonstrates a system where the structure of a Au nanoparticle is designed to maximise the overlap of the region of the highest electric field strength with a 2D material. Instead of confining the light between a nanoparticle and film, the nanoparticle shape is designed to direct the light towards the 2D material underneath. A bipyramid structure is used for this because only one of its ten sides is in contact with the substrate on which it is drop-cast. This enables the plasmon to be tilted directly towards the substrate. The structure investigated is a single Au bipyramid on a monolayer of MoS_2 on a SiO_2/Si substrate. Rabi splitting was achieved between the longitudinal plasmon of the Au bipyramids and the A exciton of the MoS_2. It was demonstrated that larger bipyramids couple more strongly with the MoS_2. This is because larger bipyramids have a higher electric field enhancement at their tips. It is also because a lower aspect ratio between the bipyramid lengths and widths was used for the larger bipyramids to keep the energy of the plasmon the same as the energy of the A exciton, which has the effect of tilting the plasmon resonance more directly towards the MoS_2 layer. Sharper tips also increase the coupling strength by causing a higher electric field strength and a stronger tilt towards the substrate. This chapter shows the first demonstration of a higher Rabi splitting strength being achieved with a higher metal volume of nanoparticle, without increasing the number of excitons being coupled into the system. Therefore, it is demonstrated that the bipyramid structure is particularly useful for Rabi splitting applications and for the design of other photonic devices. The bipyramid's field confinement at the tips could also be beneficial in other types of structures, for example by coupling to up-converting nanoparticles.

Chapter 6 also investigates the coupling of nanoparticles with MoS_2. The weak coupling effect is observed between a Si disk array on a SiO_2/Si substrate with a monolayer of MoS_2 on top. Photoluminescence enhancement is demonstrated on the MoS_2 layer when the Si disks are present for both a 405 nm and a 532 nm laser. This enhancement was shown to be primarily due to the increased absorption of the light at the pump frequencies. The system was further investigated to show how the absorption within the atomically thin MoS_2 layer can be enhanced by replacing the Si in the substrate with Au to act as a back-reflector. At 648 nm, the system is shown to be a perfect absorber, with no reflection. The MoS_2 and Si disk hybrid structure is shown to absorb 81% of the light, with the Au underneath absorbing the rest. 53% of the light was absorbed by the MoS_2 layer only. This is a huge absorption enhancement from the absorption of just 6% in the atomically thin MoS_2 layer suspended in air. This work demonstrates the tuning of the metasurface modes to overlap with the energy of the excitons of monolayer MoS_2. Therefore, it is possible to tune the modes of the metasurface to achieve high absorption at different photon energies by coupling with other materials. For example, the metasurface modes could be tuned to overlap with the A exciton of WS_2, which has an energy of 2.05 eV[66]. Enhancing the absorption of light into nanophotonic devices is of integral importance for many applications, particularly for optoelectronics and solar cells.

In conclusion, this thesis has investigated three coupled nanosystems. It has been demonstrated that the plasmon energy within a nanoparticle can be modulated and controlled with a 2D material. It has also been shown how a metasurface can greatly increase the amount of light being absorbed by a 2D material. The work in this thesis has many applications, including molecular sensing, SERS and energy harvesting.

7.1 Outlook

The results presented in this thesis show a broad range of systems with nanoparticles coupled to 2D materials. They can be explored further in a few different ways. It is possible to tune the spectral response of a plasmonic structure coupled to graphene post-fabrication by inducing a gate voltage to modify the doping level. The system in chapter 4 could be further investigated to show this, with top electrolyte gating with an ionic liquid placed over the nanostructures[149, 182]. This dynamic system would allow the control of the plasmon energies with a varying gate voltage, without modifying the gap size between the Au nanosphere and film. This could improve the system by giving more reproducible control over the spectral features. It would also be interesting for sensing applications, as the range of wavelengths covered by the spectral features post fabrication would be increased.

The system demonstrated in chapter 5 could also be modified into a dynamic system by electrical gating. A similar system with a Ag prism on a WS_2 monolayer was modified electrically, where the plasmon was shown to couple more strongly to a lower-energy trion when the gate voltage was increased[66]. The Rabi splitting between the Au bipyramid and the MoS_2 monolayer could also be modified in a similar manner.

Further investigations to increase the light absorption within a MoS_2 monolayer could be undertaken. More work could be carried out to modify the Si disk structure so the electric field strength enhancement overlaps more directly with the MoS_2. A stronger overlap between the high electric field and the MoS_2 serves to increase the absorption, according to equation 6.4.

While there are many potential avenues to take by further investigating the structures in these three systems, there are still a myriad of other structures that are still yet to be explored. One such system is to couple bipyramids to quantum dots instead of MoS_2. 2-photon-polymerisation can be used to selectively polymerise a photosensitive formulation at the tips of the bipyramids, at the position of the highest electric field enhancement. By adding quantum dots to the polymerisable solution, the quantum dots may be selectively positioned at the bipyramid tips. This system takes advantage of the bipyramid structure's high field enhancement and confinement at the tips, and also the relative strength of the longitudinal plasmon compared with the transverse plasmon. The electron oscillation is primarily along the longitudinal direction, which negates the necessity of polarising the light along the desired axis of polymerisation, which is necessary for other shapes of nanoparticles[24]. This potential use for a bipyramid shape in a different nanostructure demonstrates that the findings within this thesis can be used and modified to fit into a range of other potential structures and devices.

References

[1] V. Ilardi. Renaissance vision from spectacles to telescopes, 2007.

[2] Kutluay Uluç, Gregory C. Kujoth, and Mustafa K. Başkaya. Operating microscopes: Past, present, and future. *Neurosurgical Focus*, 27:E4, 2009.

[3] Allan Chapman. Thomas Harriot: the first telescopic astronomer., 2008.

[4] Alain Aspect. From Huygens' waves to Einstein's photons: Weird light., 2017.

[5] R.W. Ditchburn. Optics after newton. theories of light in Britain and Ireland, 1704-1840. *Optica Acta: International Journal of Optics*, 31:850–851, 1984.

[6] Thomas Young. II. The Bakerian Lecture. On the mechanism of the eye. *Philosophical Transactions of the Royal Society of London*, 91:23–88, 1801.

[7] Dipak L. Sengupta and Tapan K. Sarkar. Maxwell, Hertz, the Maxwellians, and the early history of electromagnetic waves. *IEEE Antennas and Propagation Magazine*, 45:13–19, 2003.

[8] Brian Vohnsen. A short history of optics. *Physica Scripta T*, T109:75, 2004.

[9] Richard P. Feynman. There's plenty of room at the bottom., 1959.

[10] Alf Mews. Nanomaterials handbook. edited by yury gogotsi. *Angewandte Chemie International Edition*, 46:2143, 2007.

[11] Boon K. Teo and X. H. Sun. From top-down to bottom-up to hybrid nanotechnologies: Road to nanodevices. *Journal of Cluster Science*, 17:529–540, 2006.

[12] Ulf Leonhardt. Invisibility cup. *Nature Photonics*, 1:207–208, 2007.

[13] Gustov Mie. Beiträge zur optik trüber medien, speziell kolloidaler metallösungen. annalen der physik, 1908.

[14] K. S. Novoselov, A. K. Geim, S. V. Morozov, D. Jiang, Y. Zhang, S. V. Dubonos, I. V. Grigorieva, and A. A. Firsov. Electric field in atomically thin carbon films. *Science*, 306:666–669, 2004.

[15] Kin Fai Mak, Changgu Lee, James Hone, Jie Shan, and Tony F. Heinz. Atomically thin MoS_2: A new direct-gap semiconductor. *Physical Review Letters*, 105:136805, 9 2010.

[16] Paul R. West, James L. Stewart, Alexander V. Kildishev, Vladimir M. Shalaev, Vladimir V. Shkunov, Friedrich Strohkendl, Yuri A. Zakharenkov, Robert K. Dodds, and Robert Byren. All-dielectric subwavelength metasurface focusing lens. *Optics Express*, 22:26212–26221, 2014.

[17] Ehsan Arbabi, Amir Arbabi, Seyedeh Mahsa Kamali, Yu Horie, and Andrei Faraon. Mul-

tiwavelength polarization-insensitive lenses based on dielectric metasurfaces with metamolecules. *Optica*, 3:628–633, 2016.

[18] Jae Myoung Kim, Chungyeon Lee, Yeonhee Lee, Jinhaeng Lee, So Jung Park, Sungho Park, and Jwa Min Nam. Synthesis, assembly, optical properties, and sensing applications of plasmonic gap nanostructures, 2021.

[19] Jialong Peng, Hyeon Ho Jeong, Qianqi Lin, Sean Cormier, Hsin Ling Liang, Michael F.L. De Volder, Silvia Vignolini, and Jeremy J. Baumberg. Scalable electrochromic nanopixels using plasmonics. *Science Advances*, 5:eaaw2205, 2019.

[20] Nuttawut Kongsuwan, Xiao Xiong, Ping Bai, Jia Bin You, Ching Eng Png, Lin Wu, and Ortwin Hess. Quantum plasmonic immunoassay sensing. *Nano Letters*, 19:5853–5861, 2019.

[21] En Cao, Weihua Lin, Mengtao Sun, Wenjie Liang, and Yuzhi Song. Exciton-plasmon coupling interactions: From principle to applications. *Nanophotonics*, 7:145–167, 2018.

[22] Yang Li, Chongjia Lin, Zuoxu Wu, Zhongying Chen, Cheng Chi, Feng Cao, Deqing Mei, He Yan, Chi Yan Tso, Christopher Y.H. Chao, and Baoling Huang. Solution-processed all-ceramic plasmonic metamaterials for efficient solar–thermal conversion over 100–727 °c. *Advanced Materials*, 33:2005074, 2021.

[23] Xiao Xiong, Jia Bin You, Ping Bai, Ching Eng Png, Zhang Kai Zhou, and Lin Wu. Ultrastrong coupling in single plexcitonic nanocubes. *Nanophotonics*, 9:257–266, 2019.

[24] Dandan Ge, Sylvie Marguet, Ali Issa, Safi Jradi, Tien Hoa Nguyen, Mackrine Nahra, Jéremie Béal, Régis Deturche, Hongshi Chen, Sylvain Blaize, Jérôme Plain, Céline Fiorini, Ludovic Douillard, Olivier Soppera, Xuan Quyen Dinh, Cuong Dang, Xuyong Yang, Tao Xu, Bin Wei, Xiao Wei Sun, Christophe Couteau, and Renaud Bachelot. Hybrid plasmonic nano-emitters with controlled single quantum emitter positioning on the local excitation field. *Nature Communications*, 11:1–11, 2020.

[25] Russell A. Jensen, I. Chun Huang, Ou Chen, Jennifer T. Choy, Thomas S. Bischof, Marko Lončar, and Moungi G. Bawendi. Optical trapping and two-photon excitation of colloidal quantum dots using bowtie apertures. *ACS Photonics*, 3:423–427, 2016.

[26] Gao Yang, Lihua Li, Wing Bun Lee, and Man Cheung Ng. Structure of graphene and its disorders: a review, 2018.

[27] Andrea C. Ferrari and Denis M. Basko. Raman spectroscopy as a versatile tool for studying the properties of graphene, 2013.

[28] N. D. Mermin. Crystalline order in two dimensions. *Physical Review*, 176:250, 1968.

[29] Eduardo Fradkin. Critical behavior of disordered degenerate semiconductors. II. Spectrum and transport properties in mean-field theory. *Physical Review B*, 33:3263, 1986.

[30] Phillip Richard Wallace. The band theory of graphite, 1947.

[31] Can Kun Zhang, Wei Yi Lin, Zhi Juan Zhao, Ping Ping Zhuang, Lin Jie Zhan, Ying Hui Zhou, and Wei Wei Cai. CVD synthesis of nitrogen-doped graphene using urea. *Science China: Physics, Mechanics and Astronomy*, 58:1–6, 2015.

[32] Boitumelo J. Matsoso, Kamalakannan Ranganathan, Bridget K. Mutuma, Tsenolo Lerotholi, Glenn Jones, and Neil J. Coville. Time-dependent evolution of the nitrogen configurations in n-doped graphene films. *RSC Advances*, 6:106914–106920, 2016.

[33] Cecilia Mattevi, Hokwon Kim, and Manish Chhowalla. A review of chemical vapour deposition of graphene on copper. *Journal of Materials Chemistry*, 21:3324–3334, 2011.

[34] Xuesong Li, Weiwei Cai, Jinho An, Seyoung Kim, Junghyo Nah, Dongxing Yang, Richard Piner, Aruna Velamakanni, Inhwa Jung, Emanuel Tutuc, Sanjay K. Banerjee, Luigi Colombo, and Rodney S. Ruoff. Large-area synthesis of high-quality and uniform graphene films on copper foils. *Science*, 324:1312–1314, 2009.

[35] Ramesh Rudrapati. Graphene: Fabrication methods, properties, and applications in modern industries, 2020.

[36] Yanyan Xu, Huizhe Cao, Yanqin Xue, Biao Li, and Weihua Cai. Liquid-phase exfoliation of graphene: An overview on exfoliation media, techniques, and challenges, 2018.

[37] Hua Hong, Gang Xiong, Zhizhong Dong, Bernard H. Kear, and Stephen D. Tse. Open-atmosphere flame synthesis of monolayer graphene. *Carbon*, 182:307–315, 2021.

[38] Yannick Bleu, Florent Bourquard, Teddy Tite, Anne Sophie Loir, Chirandjeevi Maddi, Christophe Donnet, and Florence Garrelie. Review of graphene growth from a solid carbon source by pulsed laser deposition (pld), 2018.

[39] Lei Shao, Xiaomu Wang, Haitao Xu, Jianfang Wang, Jian Bin Xu, Lian Mao Peng, and Hai Qing Lin. Nanoantenna-sandwiched graphene with giant spectral tuning in the visible-to-near-infrared region. *Advanced Optical Materials*, 2:162–170, 2014.

[40] Jan Mertens, Anna L. Eiden, Daniel O. Sigle, Fumin Huang, Antonio Lombardo, Zhipei Sun, Ravi S. Sundaram, Alan Colli, Christos Tserkezis, Javier Aizpurua, Silvia Milana, Andrea C. Ferrari, and Jeremy J. Baumberg. Controlling subnanometer gaps in plasmonic dimers using graphene. *Nano Letters*, 13:5033–5038, 2013.

[41] Farag S. Al-Hazmi, Ghada H. Al-Harbi, Gary W. Beall, A. A. Al-Ghamdi, A. Y. Obaid, and Waleed E. Mahmoud. Synthesis and structure of high quality graphene prepared via solvothermal exfoliation of intercalated graphite flakes. *Superlattices and Microstructures*, 86:270–274, 2015.

[42] Qingzhong Zhao, Marco Buongiorno Nardelli, and J. Bernholc. Ultimate strength of carbon

nanotubes: A theoretical study. *Physical Review B - Condensed Matter and Materials Physics*, 65:144105, 2002.

[43] Yunxiang Bai, Hongjie Yue, Jin Wang, Boyuan Shen, Silei Sun, Shijun Wang, Haidong Wang, Xide Li, Zhiping Xu, Rufan Zhang, and Fei Wei. Super-durable ultralong carbon nanotubes. *Science*, 369:1104–1106, 2020.

[44] M. F. Craciun, S. Russo, M. Yamamoto, J. B. Oostinga, A. F. Morpurgo, and S. Tarucha. Trilayer graphene is a semimetal with a gate-tunable band overlap. *Nature Nanotechnology*, 4:383–388, 2009.

[45] Alexander A. Balandin, Suchismita Ghosh, Wenzhong Bao, Irene Calizo, Desalegne Teweldebrhan, Feng Miao, and Chun Ning Lau. Superior thermal conductivity of single-layer graphene. *Nano Letters*, 8:902–907, 2008.

[46] Scott J. Goncher, Liuyan Zhao, Abhay N. Pasupathy, and George W. Flynn. Substrate level control of the local doping in graphene. *Nano Letters*, 13:1386–1392, 2013.

[47] Pooja Rani and V. K. Jindal. Designing band gap of graphene by B and N dopant atoms. *RSC Advances*, 3:802–812, 2013.

[48] Brian J. Schultz, Robert V. Dennis, Vincent Lee, and Sarbajit Banerjee. An electronic structure perspective of graphene interfaces, 2014.

[49] Lorenzo D'Arsié, Santiago Esconjauregui, Robert S. Weatherup, Xingyi Wu, William E. Arter, Hisashi Sugime, Cinzia Cepek, and John Robertson. Stable, efficient p-type doping of graphene by nitric acid. *RSC Advances*, 6:113185–113192, 2016.

[50] Rui Dong and Irma Kuljanishvili. Review article: Progress in fabrication of transition metal dichalcogenides heterostructure systems. *Journal of Vacuum Science Technology B, Nanotechnology and Microelectronics: Materials, Processing, Measurement, and Phenomena*, 35:030803, 2017.

[51] Joy Heising and Mercouri G. Kanatzidis. Exfoliated and restacked MoS_2 and WS_2: Ionic or neutral species? encapsulation and ordering of hard electropositive cations. *Journal of the American Chemical Society*, 121:11720–11732, 1999.

[52] Michael Stührenberg, Battulga Munkhbat, Denis G. Baranov, Jorge Cuadra, Andrew B. Yankovich, Tomasz J. Antosiewicz, Eva Olsson, and Timur Shegai. Strong light-matter coupling between plasmons in individual gold bi-pyramids and excitons in mono- and multilayer WSe_2. *Nano Letters*, 18:5938–5945, 2018.

[53] Majid Shahriari, Abdolmohammad Ghalambor Dezfuli, and Mohammad Sabaeian. Band structure and orbital character of monolayer MoS_2 with eleven-band tight-binding model. *Superlattices and Microstructures*, 114:169–182, 2018.

[54] Xiao Li and Hongwei Zhu. Two-dimensional MoS_2: Properties, preparation, and applications. *Journal of Materiomics*, 1:33–44, 2015.

[55] Dhirendra Sahoo, Birendra Kumar, Jaivardhan Sinha, Subhasis Ghosh, Susanta Sinha Roy, and Bhaskar Kaviraj. Cost effective liquid phase exfoliation of MoS_2 nanosheets and photocatalytic activity for wastewater treatment enforced by visible light. *Scientific Reports*, 10:1–12, 2020.

[56] Martha I. Serna, Seong H. Yoo, Salvador Moreno, Yang Xi, Juan Pablo Oviedo, Hyunjoo Choi, Husam N. Alshareef, Moon J. Kim, Majid Minary-Jolandan, and Manuel A. Quevedo-Lopez. Large-area deposition of MoS_2 by pulsed laser deposition with in situ thickness control. *ACS Nano*, 10:6054–6061, 2016.

[57] Feng Ning, Dan Wang, Ye Xin Feng, Li Ming Tang, Yong Zhang, and Ke Qiu Chen. Strong interfacial interaction and enhanced optical absorption in graphene/InAs and MoS_2/InAs heterostructures. *Journal of Materials Chemistry C*, 5:9429–9438, 2017.

[58] Omid Salehzadeh, Mehrdad Djavid, Nhung Hong Tran, Ishiang Shih, and Zetian Mi. Optically pumped two-dimensional MoS_2 lasers operating at room-temperature. *Nano Letters*, 15:5302–5306, 2015.

[59] Andrea Splendiani, Liang Sun, Yuanbo Zhang, Tianshu Li, Jonghwan Kim, Chi Yung Chim, Giulia Galli, and Feng Wang. Emerging photoluminescence in monolayer MoS_2. *Nano Letters*, 10:1271–1275, 2010.

[60] Rudren Ganatra and Qing Zhang. Few-layer MoS_2: A promising layered semiconductor, 2014.

[61] Hannu Pekka Komsa and Arkady V. Krasheninnikov. Effects of confinement and environment on the electronic structure and exciton binding energy of MoS_2 from first principles. *Physical Review B - Condensed Matter and Materials Physics*, 86:241201, 2012.

[62] U. Krishnan, M. Kaur, K. Singh, M. Kumar, and A. Kumar. A synoptic review of MoS_2: Synthesis to applications, 2019.

[63] Imen Ben Amara, Emna Ben Salem, and Sihem Jaziri. Optoelectronic response and excitonic properties of monolayer MoS_2. *Journal of Applied Physics*, 120:051707, 2016.

[64] J. Frenkel. On the transformation of light into heat in solids. I. *Physical Review*, 37:17, 1931.

[65] Kin Fai Mak, Keliang He, Changgu Lee, Gwan Hyoung Lee, James Hone, Tony F. Heinz, and Jie Shan. Tightly bound trions in monolayer MoS_2. *Nature Materials*, 12:207–211, 2012.

[66] Battulga Munkhbat, Denis G. Baranov, Ankit Bisht, Md Anamul Hoque, Bogdan Karpiak, Saroj P. Dash, and Timur Shegai. Electrical control of hybrid monolayer tungsten disulfide–plasmonic nanoantenna light–matter states at cryogenic and room temperatures. *ACS Nano*, 14:1196–1206, 2020.

[67] Gwang Hun Jung, Seok Jae Yoo, and Q. Han Park. Measuring the optical permittivity of two-dimensional materials without a priori knowledge of electronic transitions. *Nanophotonics*, 8:263–270, 2018.

[68] Encai Hao and George C. Schatz. Electromagnetic fields around silver nanoparticles and dimers. *Journal of Chemical Physics*, 120:357–366, 2004.

[69] David D. Evanoff and George Chumanov. Size-controlled synthesis of nanoparticles. 2. Measurement of extinction, scattering, and absorption cross sections. *Journal of Physical Chemistry B*, 108:13957–13962, 2004.

[70] Vivian E. Ferry, Luke A. Sweatlock, Domenico Pacifici, and Harry A. Atwater. Plasmonic nanostructure design for efficient light coupling into solar cells. *Nano Letters*, 8:4391–4397, 2008.

[71] Vincenzo Giannini, Antonio I. Fernández-Domínguez, Susannah C. Heck, and Stefan A. Maier. Plasmonic nanoantennas: Fundamentals and their use in controlling the radiative properties of nanoemitters, 2011.

[72] Caterina Serafinelli, Alessandro Fantoni, Elisabete C. B. A. Alegria, and Manuela Vieira. Hybrid nanocomposites of plasmonic metal nanostructures and 2D nanomaterials for improved colorimetric detectino, 2019.

[73] J. R. Sambles, G. W. Bradbery, and Fuzi Yang. Optical excitation of surface plasmons: An introduction. *Contemporary Physics*, 32:173–183, 1991.

[74] M. D. Mcmahon, R. Lopez, H. M. Meyer, L. C. Feldman, and R. F. Haglund. Rapid tarnishing of silver nanoparticles in ambient laboratory air. *Applied Physics B: Lasers and Optics*, 80:915–921, 2005.

[75] Bowen Li, Shuai Zu, Jiadong Zhou, Qiao Jiang, Bowen Du, Hangyong Shan, Yang Luo, Zheng Liu, Xing Zhu, and Zheyu Fang. Single-nanoparticle plasmonic electro-optic modulator based on MoS_2 monolayers. *ACS Nano*, 11:9720–9727, 2017.

[76] Jinshui Miao, Weida Hu, Youliang Jing, Wenjin Luo, Lei Liao, Anlian Pan, Shiwei Wu, Jingxin Cheng, Xiaoshuang Chen, and Wei Lu. Surface plasmon-enhanced photodetection in few layer MoS_2 phototransistors with au nanostructure arrays. *Small*, 11:2392–2398, 2015.

[77] Bumsu Lee, Joohee Park, Gang Hee Han, Ho Seok Ee, Carl H. Naylor, Wenjing Liu, A. T.Charlie Johnson, and Ritesh Agarwal. Fano resonance and spectrally modified photoluminescence enhancement in monolayer MoS_2 integrated with plasmonic nanoantenna array. *Nano Letters*, 15:3646–3653, 2015.

[78] Johannes Kern, Andreas Trügler, Iris Niehues, Johannes Ewering, Robert Schmidt, Robert Schneider, Sina Najmaei, Antony George, Jing Zhang, Jun Lou, Ulrich Hohenester, Steffen

Michaelis De Vasconcellos, and Rudolf Bratschitsch. Nanoantenna-enhanced light-matter interaction in atomically thin WS_2. *ACS Photonics*, 2:1260–1265, 2015.

[79] Rebecca Heilmann, Aaro I. Väkeväinen, Jani Petri Martikainen, and Päivi Törmä. Strong coupling between organic dye molecules and lattice modes of a dielectric nanoparticle array. *Nanophotonics*, 9:267–276, 2020.

[80] Isabelle Staude and Jörg Schilling. Metamaterial-inspired silicon nanophotonics. *Nature Photonics*, 11:274–284, 2017.

[81] Roman S. Savelev, Alexey P. Slobozhanyuk, Andrey E. Miroshnichenko, Yuri S. Kivshar, and Pavel A. Belov. Subwavelength waveguides composed of dielectric nanoparticles. *Physical Review B - Condensed Matter and Materials Physics*, 89:035435, 2014.

[82] Lin Cheng, Rasoul Alaee, Akbar Safari, Mohammad Karimi, Lei Zhang, and Robert W. Boyd. Superscattering, superabsorption, and nonreciprocity in nonlinear antennas. *ACS Photonics*, 8:585–591, 2021.

[83] Manuel Decker, Isabelle Staude, Matthias Falkner, Jason Dominguez, Dragomir N. Neshev, Igal Brener, Thomas Pertsch, and Yuri S. Kivshar. High-efficiency dielectric Huygens' surfaces. *Advanced Optical Materials*, 3:813–820, 2015.

[84] Xia Zhang, Jing Li, John F. Donegan, and A. Louise Bradley. Constructive and destructive interference of Kerker-type scattering in an ultrathin silicon huygens metasurface. *Physical Review Materials*, 4:125202, 2020.

[85] Xia Zhang, Julia Lawless, Jing Li, John F. Donegan, Lisanne Peters, Niall McEvoy, and A. Louise Bradley. Absorbance enhancement of monolayer MoS_2 in a perfect absorbing system., 2022.

[86] Sheng Liu, Gordon A. Keeler, John L. Reno, Michael B. Sinclair, and Igal Brener. III–V Semiconductor nanoresonators—a new strategy for passive, active, and nonlinear all-dielectric metamaterials. *Advanced Optical Materials*, 4:1457–1462, 2016.

[87] Viktoriia E. Babicheva and Andrey B. Evlyukhin. Resonant lattice Kerker effect in metasurfaces with electric and magnetic optical responses. *Laser and Photonics Reviews*, 11:1700132, 2017.

[88] M. Kerker, D. S. Wang, and C. L. Giles. Electromagnetic scattering by magnetic spheres. *Journal of the Optical Society of America*, 73:765–767, 1983.

[89] Parikshit Moitra, Brian A. Slovick, Zhi Gang Yu, S. Krishnamurthy, and Jason Valentine. Experimental demonstration of a broadband all-dielectric metamaterial perfect reflector. *Applied Physics Letters*, 104:171102, 2014.

[90] E. M. Purcell. Spontaneous emission probabilities at radio frequencies, 1995.

[91] Illhwan Lee, Jae Yong Park, Kihyon Hong, Jun Ho Son, Sungjun Kim, and Jong Lam Lee. The effect of localized surface plasmon resonance on the emission color change in organic light emitting diodes. *Nanoscale*, 8:6463–6467, 2016.

[92] M. Fleischmann, P. J. Hendra, and A. J. McQuillan. Raman spectra of pyridine adsorbed at a silver electrode, 1974.

[93] Ken Ichi Yoshida, Tamitake Itoh, Hiroharu Tamaru, Vasudevanpillai Biju, Mitsuru Ishikawa, and Yukihiro Ozaki. Quantitative evaluation of electromagnetic enhancement in surface-enhanced resonance Raman scattering from plasmonic properties and morphologies of individual Ag nanostructures. *Physical Review B - Condensed Matter and Materials Physics*, 81:115406, 2010.

[94] Katrin Kneipp, Yang Wang, Harald Kneipp, Lev T. Perelman, Irving Itzkan, Ramachandra R. Dasari, and Michael S. Feld. Single molecule detection using surface-enhanced Raman scattering (SERS). *Physical Review Letters*, 78:1667, 1997.

[95] E. C. Le Ru, E. Blackie, M. Meyer, and P. G. Etchegoint. Surface enhanced Raman scattering enhancement factors: A comprehensive study. *Journal of Physical Chemistry C*, 111:13794–13803, 2007.

[96] G. Khitrova, H. M. Gibbs, M. Kira, S. W. Koch, and A. Scherer. Vacuum Rabi splitting in semiconductors. *Nature Physics*, 2:81–90, 2006.

[97] P. Törmä and W. L. Barnes. Strong coupling between surface plasmon polaritons and emitters. *Rep. Prog. Phys.*, 78:013901, 2015.

[98] Felix Stete, Wouter Koopman, and Matias Bargheer. Signatures of strong coupling on nanoparticles: Revealing absorption anticrossing by tuning the dielectric environment. *ACS Photonics*, 4:1669–1676, 2017.

[99] J. P. Reithmaier, G. Sk, A. Löffler, C. Hofmann, S. Kuhn, S. Reitzenstein, L. V. Keldysh, V. D. Kulakovskii, T. L. Reinecke, and A. Forchel. Strong coupling in a single quantum dot-semiconductor microcavity system. *Nature*, 432:197–200, 2004.

[100] T. Yoshle, A. Scherer, J. Hendrickson, G. Khitrova, H. M. Gibbs, G. Rupper, C. Ell, O. B. Shchekin, and D. G. Deppe. Vacuum Rabi splitting with a single quantum dot in a photonic crystal nanocavity. *Nature*, 432:200–203, 2004.

[101] E. Peter, P. Senellart, D. Martrou, A. Lemaître, J. Hours, J. M. Gérard, and J. Bloch. Exciton-photon strong-coupling regime for a single quantum dot embedded in a microcavity. *Physical Review Letters*, 95:067401, 2005.

[102] Tomasz J. Antosiewicz, S. Peter Apell, and Timur Shegai. Plasmon-exciton interactions in a

core-shell geometry: From enhanced absorption to strong coupling. *ACS Photonics*, 1:454–463, 2014.

[103] Sinan Balci. Ultrastrong plasmon–exciton coupling in metal nanoprisms with J-aggregates. *Optics Letters*, 38:4498, 11 2013.

[104] Andrea E. Schlather, Nicolas Large, Alexander S. Urban, Peter Nordlander, and Naomi J. Halas. Near-field mediated plexcitonic coupling and giant Rabi splitting in individual metallic dimers. *Nano Letters*, 13:3281–3286, 2013.

[105] Martin Wersall, Jorge Cuadra, Tomasz J. Antosiewicz, Sinan Balci, and Timur Shegai. Observation of mode splitting in photoluminescence of individual plasmonic nanoparticles strongly coupled to molecular excitons. *Nano Letters*, 17:551–558, 2017.

[106] Jorge Cuadra, Denis G. Baranov, Martin Wersäll, Ruggero Verre, Tomasz J. Antosiewicz, and Timur Shegai. Observation of tunable charged exciton polaritons in hybrid monolayer WS_2-plasmonic nanoantenna system. *Nano Letters*, 18:1777–1785, 2018.

[107] Di Zheng, Shunping Zhang, Qian Deng, Meng Kang, Peter Nordlander, and Hongxing Xu. Manipulating coherent plasmon-exciton interaction in a single silver nanorod on monolayer WSe_2. *Nano Letters*, 17:3809–3814, 2017. nanorods and TMDCs.

[108] Wei Wang, Parinda Vasa, Robert Pomraenke, Ralf Vogelgesang, Antonietta De Sio, Ephraim Sommer, Margherita Maiuri, Cristian Manzoni, Giulio Cerullo, and Christoph Lienau. Interplay between strong coupling and radiative damping of excitons and surface plasmon polaritons in hybrid nanostructures. *ACS Nano*, 8:1056–1064, 2014.

[109] Xiao Xiong, Nuttawut Kongsuwan, Yiming Lai, Ching Eng Png, Lin Wu, and Ortwin Hess. Room-temperature plexcitonic strong coupling: Ultrafast dynamics for quantum applications, 2021.

[110] Anoop Thomas, Jino George, Atef Shalabney, Marian Dryzhakov, Sreejith J. Varma, Joseph Moran, Thibault Chervy, Xiaolan Zhong, Eloïse Devaux, Cyriaque Genet, James A. Hutchison, and Thomas W. Ebbesen. Ground-state chemical reactivity under vibrational coupling to the vacuum electromagnetic field. *Angewandte Chemie*, 128:11634–11638, 2016.

[111] Yantao Pang, Anoop Thomas, Kalaivanan Nagarajan, Robrecht M.A. Vergauwe, Kripa Joseph, Bianca Patrahau, Kuidong Wang, Cyriaque Genet, and Thomas W. Ebbesen. On the role of symmetry in vibrational strong coupling: The case of charge-transfer complexation. *Angewandte Chemie - International Edition*, 59:10436–10440, 2020.

[112] Anoop Thomas, Anjali Jayachandran, Lucas Lethuillier-Karl, Robrecht M.A. Vergauwe, Kalaivanan Nagarajan, Eloise Devaux, Cyriaque Genet, Joseph Moran, and Thomas W. Ebbe-

sen. Ground state chemistry under vibrational strong coupling: Dependence of thermodynamic parameters on the Rabi splitting energy. *Nanophotonics*, 9:249–255, 2020.

[113] Susumu Noda, Masayuki Fujita, and Takashi Asano. Spontaneous-emission control by photonic crystals and nanocavities. *Nature Photonics*, 1:449, 2007.

[114] C. Lang, D. Bozyigit, C. Eichler, L. Steffen, J. M. Fink, A. A. Abdumalikov, M. Baur, S. Filipp, M. P. Da Silva, A. Blais, and A. Wallraff. Observation of resonant photon blockade at microwave frequencies using correlation function measurements. *Physical Review Letters*, 106:243601, 2011.

[115] Jia Bin You, Xiao Xiong, Ping Bai, Zhang Kai Zhou, Ren Min Ma, Wan Li Yang, Yu Kun Lu, Yun Feng Xiao, Ching Eng Png, Francisco J. Garcia-Vidal, Cheng Wei Qiu, and Lin Wu. Reconfigurable photon sources based on quantum plexcitonic systems. *Nano Letters*, 20:4645–4652, 2020.

[116] Allen Taflove, Susan C. Hagness, and Melinda Piket-May. Computational electromagnetics: The finite-difference time-domain method, 2005.

[117] Yiqun Zheng, Xiaolan Zhong, Zhiyuan Li, and Younan Xia. Successive, seed-mediated growth for the synthesis of single-crystal gold nanospheres with uniform diameters controlled in the range of 5-150 nm. *Particle and Particle Systems Characterization*, 31:266–273, 2014.

[118] Ralph G. Pearson. Hard and soft acids and bases. *Journal of the American Chemical Society*, 85:3533–3539, 1963.

[119] Mingzhao Liu and Philippe Guyot-Sionnest. Mechanism of silver(I)-assisted growth of gold nanorods and bipyramids. *Journal of Physical Chemistry B*, 109:22192–22200, 2005.

[120] N. R. Jana, L. Gearheart, and C. J. Murphy. Seed-mediated growth approach for shape-controlled synthesis of spheroidal and rod-like gold nanoparticles using a surfactant template. *Advanced Materials*, 13:1389–1393, 2001.

[121] Sukang Bae, Hyeongkeun Kim, Youngbin Lee, Xiangfan Xu, Jae Sung Park, Yi Zheng, Jayakumar Balakrishnan, Tian Lei, Hye Ri Kim, Young Il Song, Young Jin Kim, Kwang S. Kim, Barbaros Özyilmaz, Jong Hyun Ahn, Byung Hee Hong, and Sumio Iijima. Roll-to-roll production of 30-inch graphene films for transparent electrodes. *Nature Nanotechnology*, 5:574–578, 2010.

[122] Bilu Liu, Mohammad Fathi, Liang Chen, Ahmad Abbas, Yuqiang Ma, and Chongwu Zhou. Chemical vapor deposition growth of monolayer WSe_2 with tunable device characteristics and growth mechanism study. *ACS Nano*, 9:6119–6127, 6 2015.

[123] John Mann, Dezheng Sun, Quan Ma, Jen Ru Chen, Edwin Preciado, Taisuke Ohta, Bogdan Diaconescu, Koichi Yamaguchi, Tai Tran, Michelle Wurch, Katiemarie Magnone, Tony F.

Heinz, Gary L. Kellogg, Roland Kawakami, and Ludwig Bartels. Facile growth of monolayer MoS_2 film areas on SiO_2. *European Physical Journal B*, 86:226, 2013.

[124] Cheol Min Hyun, Jeong Hun Choi, Seung Won Lee, Jeong Hwa Park, Kang Taek Lee, and Ji Hoon Ahn. Synthesis mechanism of MoS_2 layered crystals by chemical vapor deposition using MoS3 and sulfur powders. *Journal of Alloys and Compounds*, 765:380–384, 2018.

[125] Maria O'Brien, Nils Scheuschner, Janina Maultzsch, Georg S. Duesberg, and Niall McEvoy. Raman spectroscopy of suspended MoS_2. *Physica Status Solidi (B) Basic Research*, 254:1700218, 2017.

[126] A. C. Ferrari, J. C. Meyer, V. Scardaci, C. Casiraghi, M. Lazzeri, F. Mauri, S. Piscanec, D. Jiang, K. S. Novoselov, S. Roth, and A. K. Geim. Raman spectrum of graphene and graphene layers. *Physical Review Letters*, 97:187401, 2006.

[127] C. Thomsen and S. Reich. Double resonant Raman scattering in graphite. *Physical Review Letters*, 85:5214, 2000.

[128] K. Gołasa, M. Grzeszczyk, K. P. Korona, R. Bozek, J. Binder, J. Szczytko, A. Wysmołek, and A. Babiński. Optical properties of molybdenum disulfide (MoS_2). *Acta Physica Polonica A*, 124:849–851, 2013.

[129] Joohoon Kang, Jung Woo T. Seo, Diego Alducin, Arturo Ponce, Miguel Jose Yacaman, and Mark C. Hersam. Thickness sorting of two-dimensional transition metal dichalcogenides via copolymer-assisted density gradient ultracentrifugation. *Nature Communications*, 5:1–7, 2014.

[130] Changgu Lee, Hugen Yan, Louis E. Brus, Tony F. Heinz, James Hone, and Sunmin Ryu. Anomalous lattice vibrations of single- and few-layer MoS_2. *ACS Nano*, 4:2695–2700, 2010.

[131] B. J. Mrstik, R. Kaplan, T. L. Reinecke, M. Van Hove, and S. Y. Tong. Surface-structure determination of the layered compounds MoS_2 and NbSe2 by low-energy electron diffraction. *Physical Review B*, 15:897, 1977.

[132] T. J. Wieting and J. L. Verble. Interlayer bonding and the lattice vibrations of β-GaSe. *Physical Review B*, 5:1473, 1972.

[133] A. Steinhoff, J. H. Kim, F. Jahnke, M. Rösner, D. S. Kim, C. Lee, G. H. Han, M. S. Jeong, T. O. Wehling, and C. Gies. Efficient excitonic photoluminescence in direct and indirect band gap monolayer MoS2. *Nano Letters*, 15:6841–6847, 2015.

[134] Hongyan Shi, Rusen Yan, Simone Bertolazzi, Jacopo Brivio, Bo Gao, Andras Kis, Debdeep Jena, Huili Grace Xing, and Libai Huang. Exciton dynamics in suspended monolayer and few-layer MoS_2 2D crystals. *ACS Nano*, 7:1072–1080, 2 2013.

[135] Jeremy J. Baumberg, Javier Aizpurua, Maiken H. Mikkelsen, and David R. Smith. Extreme nanophotonics from ultrathin metallic gaps, 2019.

[136] Seungwoo Lee. Nanoparticle-on-mirror cavity: a historical view across nanophotonics and nanochemistry, 2022.

[137] Sean Cormier, Tao Ding, Vladimir Turek, and Jeremy J. Baumberg. Actuating single nano-oscillators with light. *Advanced Optical Materials*, 6:1701281, 2018.

[138] Dean Kos, Giuliana Di Martino, Alexandra Boehmke, Bart de Nijs, Dénes Berta, Tamás Földes, Sara Sangtarash, Edina Rosta, Hatef Sadeghi, and Jeremy J. Baumberg. Optical probes of molecules as nano-mechanical switches. *Nature Communications*, 11:1–8, 2020.

[139] Hao Chen, Abdul M. Bhuiya, Runyu Liu, Daniel M. Wasserman, and Kimani C. Toussaint. Design, fabrication, and characterization of near-IR gold bowtie nanoantenna arrays. *Journal of Physical Chemistry C*, 118:20553–20558, 2014.

[140] Stephen Cunningham and A. Louise Bradley. Tunable plasmonics with au nanoparticles coupled to thin film vanadium dioxide, 2022.

[141] Gleb M. Akselrod, Tian Ming, Christos Argyropoulos, Thang B. Hoang, Yuxuan Lin, Xi Ling, David R. Smith, Jing Kong, and Maiken H. Mikkelsen. Leveraging nanocavity harmonics for control of optical processes in 2D semiconductors. *Nano Letters*, 15:3578–3584, 2015.

[142] Jiani Huang, Gleb M. Akselrod, Tian Ming, Jing Kong, and Maiken H. Mikkelsen. Tailored emission spectrum of 2D semiconductors using plasmonic nanocavities. *ACS Photonics*, 5:552–558, 2018.

[143] Daniel O. Sigle, Jan Mertens, Lars O. Herrmann, Richard W. Bowman, Sandrine Ithurria, Benoit Dubertret, Yumeng Shi, Hui Ying Yang, Christos Tserkezis, Javier Aizpurua, and Jeremy J. Baumberg. Monitoring morphological changes in 2D monolayer semiconductors using atom-thick plasmonic nanocavities. *ACS Nano*, 9:825–830, 2015.

[144] Tian Zhang, Lin Chen, and Xun Li. Graphene-based tunable broadband hyperlens for far-field subdiffraction imaging at mid-infrared frequencies. *Optics Express*, 21:20888–20899, 2013.

[145] Hua Zhu, Ming Deng, Shuqi Chen, and Lin Chen. Graphene-based meta-coupler for direction-controllable emission of surface plasmons. *Optics Letters*, 44:3382–3385, 2019.

[146] Yu Yao, Mikhail A. Kats, Patrice Genevet, Nanfang Yu, Yi Song, Jing Kong, and Federico Capasso. Broad electrical tuning of graphene-loaded plasmonic antennas. *Nano Letters*, 13:1257–1264, 2013.

[147] Yu Yao, Mikhail A. Kats, Raji Shankar, Yi Song, Jing Kong, Marko Loncar, and Federico Capasso. Wide wavelength tuning of optical antennas on graphene with nanosecond response time. *Nano Letters*, 14:214–219, 2014.

[148] Yu Yao, Raji Shankar, Patrick Rauter, Yi Song, Jing Kong, Marko Loncar, and Federico Capasso. High-responsivity mid-infrared graphene detectors with antenna-enhanced photocarrier generation and collection. *Nano Letters*, 14:3749–3754, 2014.

[149] Jonghwan Kim, Hyungmok Son, David J. Cho, Baisong Geng, Will Regan, Sufei Shi, Kwanpyo Kim, Alex Zettl, Yuen Ron Shen, and Feng Wang. Electrical control of optical plasmon resonance with graphene. *Nano Letters*, 12:5598–5602, 2012.

[150] Mohsin Habib, Alireza Rahimi Rashed, Ekmel Ozbay, and Humeyra Caglayan. Graphene-based tunable plasmon induced transparency in gold strips. *Optical Materials Express*, 8:1069–1074, 2018.

[151] Yuan Wan, Luogen Deng, Lei Wang, Mingchao Yang, and Yuli Wang. Modulation of visible and near-infrared surface plasmon resonance of au nanoparticles based on highly doped graphene. *Plasmonics*, 12:1317–1324, 2017.

[152] Yuan Wan, Yuanxin Tan, Yang Yang, Haining Chong, Zhaozhong Meng, and Jing Wang. Actively tunable fano resonance in H-like metal-graphene hybrid nanostructures. *Plasmonics*, 17:843–849, 2022.

[153] Shuhua Cao, Qi Wang, Xufeng Gao, Shijie Zhang, Ruijin Hong, and Dawei Zhang. Monolayer-graphene-based tunable absorber in the near-infrared. *Micromachines*, 12:1320, 2021.

[154] Danthure Arachchige Dayantha Lankanath Karunasena, Guangqing Du, Qing Yang, Gulshan Iqbal, Noor Uddin, Xun Hou, and Feng Chen. Stable plasmonic nano-trapping using a hybrid gold-graphene V-trench with an extremely deep potential well. *Optical Materials Express*, 11:4107–4117, 2021.

[155] A. Das, S. Pisana, B. Chakraborty, S. Piscanec, S. K. Saha, U. V. Waghmare, K. S. Novoselov, H. R. Krishnamurthy, A. K. Geim, A. C. Ferrari, and A. K. Sood. Monitoring dopants by Raman scattering in an electrochemically top-gated graphene transistor. *Nature Nanotechnology*, 3:210–215, 2008.

[156] P. B. Johnson and R. W. Christy. Optical constants of the noble metals. *Physical Review B*, 6:4370, 1972.

[157] Patrick Kékicheff and Olivier Spalla. Refractive index of thin aqueous films confined between two hydrophobic surfaces. *Langmuir*, 10:1584–1591, 1994.

[158] T. Stauber, N. M.R. Peres, and A. K. Geim. Optical conductivity of graphene in the visible region of the spectrum. *Physical Review B - Condensed Matter and Materials Physics*, 78:085432, 2008.

[159] Isabel Romero, Javier Aizpurua, Garnett W. Bryant, and F. Javier García De Abajo. Plasmons

in nearly touching metallic nanoparticles: singular response in the limit of touching dimers. *Optics Express*, 14:9988–9999, 2006.

[160] J. Mertens, A. Demetriadou, R. W. Bowman, F. Benz, M. E. Kleemann, C. Tserkezis, Y. Shi, H. Y. Yang, O. Hess, J. Aizpurua, and J. J. Baumberg. Tracking optical welding through groove modes in plasmonic nanocavities. *Nano Letters*, 16:5605–5611, 2016.

[161] S. Arcidiacono, N. R. Bieri, D. Poulikakos, and C. P. Grigoropoulos. On the coalescence of gold nanoparticles. *International Journal of Multiphase Flow*, 30:979–994, 2004.

[162] Felix Benz, Bart de Nijs, Christos Tserkezis, Rohit Chikkaraddy, Daniel O. Sigle, Laurynas Pukenas, Stephen D. Evans, Javier Aizpurua, and Jeremy J. Baumberg. Generalized circuit model for coupled plasmonic systems. *Optics Express*, 23:33255–33269, 2015.

[163] Navid Solati, Sonia Mobassem, Abdullah KahRaman, Hirohito Ogasawara, and Sarp Kaya. A comprehensive study on the characteristic spectroscopic features of nitrogen doped graphene. *Applied Surface Science*, 495:143518, 2019.

[164] N. Yamamoto, S. Ohtani, and F. Javier García De Abajo. Gap and Mie plasmons in individual silver nanospheres near a silver surface. *Nano Letters*, 11:91–95, 2011.

[165] Sharmin Haq, Tefera E. Tesema, Bisweswar Patra, Eric Gomez, and Terefe G. Habteyes. Tuning plasmonic coupling from capacitive to conductive regimes via atomic control of dielectric spacing. *ACS Photonics*, 7:622–629, 2020.

[166] Maria O'Brien, Niall McEvoy, Toby Hallam, Hye Young Kim, Nina C. Berner, Damien Hanlon, Kangho Lee, Jonathan N. Coleman, and Georg S. Duesberg. Transition metal dichalcogenide growth via close proximity precursor supply. *Scientific Reports*, 4:1–7, 2014.

[167] V. Savona, L. C. Andreani, P. Schwendimann, and A. Quattropani. Quantum well excitons in semiconductor microcavities: Unified treatment of weak and strong coupling regimes. *Solid State Communications*, 93:733–739, 1995.

[168] Yu Ye, Zi Jing Wong, Xiufang Lu, Xingjie Ni, Hanyu Zhu, Xianhui Chen, Yuan Wang, and Xiang Zhang. Monolayer excitonic laser. *Nature Photonics*, 9:733–737, 2015.

[169] Dominik Kufer and Gerasimos Konstantatos. Highly sensitive, encapsulated MoS_2 photodetector with gate controllable gain and speed. *Nano Letters*, 15:7307–7313, 2015.

[170] Tao Jiang, Di Huang, Jinluo Cheng, Xiaodong Fan, Zhihong Zhang, Yuwei Shan, Yangfan Yi, Yunyun Dai, Lei Shi, Kaihui Liu, Changgan Zeng, Jian Zi, J. E. Sipe, Yuen Ron Shen, Wei Tao Liu, and Shiwei Wu. Gate-tunable third-order nonlinear optical response of massless Dirac fermions in graphene, 2018.

[171] Wei Li, A. Glen Birdwell, Matin Amani, Robert A. Burke, Xi Ling, Yi Hsien Lee, Xuelei Liang, Lianmao Peng, Curt A. Richter, Jing Kong, David J. Gundlach, and N. V. Nguyen.

Broadband optical properties of large-area monolayer CVD molybdenum disulfide. *Physical Review B - Condensed Matter and Materials Physics*, 90:195434, 2014.

[172] Mingxiao Ye, Dustin Winslow, Dongyan Zhang, Ravindra Pandey, and Yoke Khin Yap. Recent advancement on the optical properties of two-dimensional molybdenum disulfide (MoS_2) thin films, 2015.

[173] Michele Buscema, Gary A. Steele, Herre S.J. van der Zant, and Andres Castellanos-Gomez. The effect of the substrate on the Raman and photoluminescence emission of single-layer MoS_2. *Nano Research*, 7:561–571, 2014.

[174] D. Kaplan, Y. Gong, K. Mills, V. Swaminathan, P. M. Ajayan, S. Shirodkar, and E. Kaxiras. Excitation intensity dependence of photoluminescence from monolayers of MoS_2 and WS_2/MoS_2 heterostructures. *2D Materials*, 3:015005, 2016.

[175] Stephen Cunningham, Calin Hrelescu, and A. Louise Bradley. Plasmonic nanodiscs on vanadium dioxide thin films for tunable luminescence enhancement. *Optics Express*, 29:22288–22298, 2021.

[176] G. Baffou, R. Quidant, and C. Girard. Heat generation in plasmonic nanostructures: Influence of morphology. *Applied Physics Letters*, 94:153109, 2009.

[177] B. Zhao, J. M. Zhao, and Z. M. Zhang. Enhancement of near-infrared absorption in graphene with metal gratings. *Applied Physics Letters*, 105:031905, 2014.

[178] Hua Lu, Xuetao Gan, Dong Mao, Yicun Fan, Dexing Yang, and Jianlin Zhao. Nearly perfect absorption of light in monolayer molybdenum disulfide supported by multilayer structures. *Optics Express*, 25:21630–21636, 2017.

[179] L. Sortino, P. G. Zotev, S. Mignuzzi, J. Cambiasso, D. Schmidt, A. Genco, M. Aßmann, M. Bayer, S. A. Maier, R. Sapienza, and A. I. Tartakovskii. Enhanced light-matter interaction in an atomically thin semiconductor coupled with dielectric nano-antennas. *Nature Communications*, 10:1–8, 2019.

[180] Maurizia Palummo, Marco Bernardi, and Jeffrey C. Grossman. Exciton radiative lifetimes in two-dimensional transition metal dichalcogenides. *Nano Letters*, 15:2794–2800, 2015.

[181] Haining Wang, Changjian Zhang, Weimin Chan, Christina Manolatou, Sandip Tiwari, and Farhan Rana. Radiative lifetimes of excitons and trions in monolayers of the metal dichalcogenide MoS^2. *Physical Review B*, 93:045407, 2016.

[182] Dhiraj Prasai, Andrey R. Klots, A. K.M. Newaz, J. Scott Niezgoda, Noah J. Orfield, Carlos A. Escobar, Alex Wynn, Anatoly Efimov, G. Kane Jennings, Sandra J. Rosenthal, and Kirill I. Bolotin. Electrical control of near-field energy transfer between quantum dots and two-dimensional semiconductors. *Nano Letters*, 15:4374–4380, 2015.